Università degli Studi di Cagliari

Ph.D. DEGREE

Industrial Engineering

Cycle XXXIV

TITLE OF THE Ph.D. THESIS

Uncertainty Quantification and Optimization of Aeronautical Components

Scientific Disciplinary Sector(s)

ING-IND/08

Ph.D. Student:	Irene Virdis
Supervisor	Tiziano Ghisu

Final exam. Academic Year 2020/2021
Thesis defence: April 2022 Session

Abstract

This project was part of a wider investigation performed on a set of 200 High Pressure Turbine (HPT) blades, dismounted after several hours of flight and characterized by in-service and manufacturing variations.

The main objective of this project was to determine the impact of these variations on the aerodynamic performance of the rotor and to devise a strategy to design more robust geometries, i.e, less sensitive to the given uncertainties.

The initial set of data consisted of the digitized versions of the blades (GOM scans). The geometrical deviations characterizing the blades from their hub until the 70% of the span were parametrized via a set of aerodynamic Engineering Parameters belonging to PADRAM design space (EP) and quantified via an inverse mapping procedure (P2S-PADRAM-SOFT); the visual inspection of the digital twins highlighted a considerable volume loss along the blade rim (tip region) due to localized erosion: the quantification of this metal degradation was performed via in-house Python scripts and expressed as indices of volume removal rate (PADRAM Squealer Tip option).

The adjoint solver and the Polynomial Chaos Expansion (PCE) were used for the Uncertainty Propagation (UP) of the first set of uncertain variables, while for the erosion parameters only PCE was selected. The sensitivity of the nominal blade with respect to the typical erosion level was found to be higher than that of the geometrical deviations occurring beneath the tip.

UP was followed by a series of gradient-based robust optimizations (RO) approaches. The rotor efficiency was selected as the figure of merit to be maximized by optimizing the EP values; in the first approach, the performance of a simplified geometry (without winglet and gutter) was slightly improved driving SLSQP Python optimizer via adjoint gradients. Following this, the nominal configuration, complete with winglet and gutter, was optimized providing SLSQP with the first order derivatives calculated via PCE. The same strategy for the calculation of the derivatives was used in the third approach, only this time the erosion level, characterizing the worst damaged rim, was included. A local, gradient-based, optimization was then performed in a larger design space: the final optimized configuration is then recovered a good percentage of rotor efficiency otherwise lost when the erosion occurs, thanks to an offloading of the tip region, while also improving the nominal rotor performance.

Acknowledgments

The author would like to thank Rolls-Royce for their support and permission to publish this work. This project has received funding from the European Union's Horizon 2020 research and innovation program under Grant Agreement No. 769025.

Thanks to Shahrokh Shahpar from Rolls-Royce Derby and Haidong Li from Rolls-Royce Bristol for the technical support and for sharing their knowledge. Thanks to Indi, Karl Huckerby and Daniele Gorla in Rolls-Royce Derby for the time dedicated and the precious support.

Thanks to Pranay and Ashley for giving me the opportunity to collaborate with Effective Quadratures, for all the knowledge and the inspiration they shared.

Many thanks to Diego and Inaki for all the explanations received but overall for being an amazing source of new ideas. To Mario, for being the best ever teammate inside and outside of the office. To Giorgia, irreplaceable friend and adventure mate. To my parents, Erika and Lorenzo, whose love supports me every day. To David, an infinite source of energy and love. To Tiziano, for the patience, the technical and the moral support, thanks for always being on my side.

Contents

List of Figures

Acronyms	**Definitions**
CAD	Computer-aided design
CFD	Computational Fluid Dynamics
CFL	Courant-Friedrichs-Lewy
DoE	Design of Experiment(s)
EFH	Engine flying hours
GD	Geometrical Deviations due to manufact. and in-service deformations
HPT	High Pressure Turbine
SLSQP	Sequential Least SQuares Programming
MAM	Multi point Approximation Method
NIPCE	Non-Intrusive Polynomial Chaos Expansion
OTL	Over Tip Leakage
PADRAM	PARametric Design and Rapid Meshing
PCE	Polynomial Chaos Expansion
PDF	Probability Density Function
PS	Pressure Side of the blade
RAF	Royal Air Force
RANS	Reynolds-averaged Navier-Stokes
RDO	Robust Design Optimization
RMS	Root Mean Square
RO	Robust Optimization
R&D	Research And Development
SITC	Standard International Trade Classification
SQP	Sequential Quadratic Programming
SST	Shear Stress Transport
SMH	Scheduled Maintenance Hours
SOFT	Smart Optimization For Turbomachinery
SS	Suction Side of the blade
STL	Stereolitography file
TBC	Thermal Barrier Coating
UP	Uncertainty Propagation
UQ	Uncertainty Quantification
Greeks	**Definition**
η	rotor efficiency
σ_η	Standad Deviation of rotor efficiency
Latin	
c	blade chord
P	polynominal expansion order
o_e	order of orthogonal polynomial
Subscripts	
e	eroded
IN	inlet
m	mean value
n	nominal
n,d	nominal not eroded
OUT	outlet

Chapter 1

Introduction

1.1 Research and Development in Aeronautics

High technology sectors have a decisive role in the global market: the intensive nature of their research and development (R&D) outputs competitive products which promote quality improvements to other sectors, as well as a healthy competition environment for all the involved stakeholders.

The work of Hatzichronoglou [44] collects several considerations regarding the identification and classification of industrial sectors and their related products. In this study, the aerospace industry's *R&D* is systematically ranked as the number one sector among other advanced industrial and manufacturing types of companies, according to different classification methodologies. The SITC (Standard International Trade Classification), revision 3, elects turbo-jets and aero-engines (along with their components) among the systems with the highest degree of technology.

The role of aeronautical's R&D is wide. Beyond the development of advanced aircraft like the Concorde, U2 or the WB-57F, it has also contributed to the development of other industrial sectors thanks to its deep understanding, comprehension, and interpretation of fluid dynamics interactions around simple and complex geometries [69].

Multiple reasons can be listed to explain why research on jet engines still boosts the *spillover* role in both economical and financial fields: the forecast (towards 2050) of the transportation market estimates a sharp increase in international mobility. This increase is pushed by the development of long-range transport solutions involving global commerce and the increasing trend in people's mobility [10]. The design of a jet engine is subject not only to the high competitiveness of the global market or high levels of operational safety but also to the requirement of low fuel consumptions given by environmental regulations [10]. The robustness of the engine design becomes crucial to meet these numerous requirements and ensure reliability in performance.

1.2 Jet Engine Design

It was only 1940 when the Royal Air Force officer Arthur Tedder, searching for new engines to be used in British warplanes during World War II, entered Frank Whittle's laboratory and saw a jet engine for the first time [77]. At the time, the gas turbine was known by a restricted niche of constructors, and research was strongly needed to push the first prototypes to become an effective propulsion system.

The operating principles of jet propulsion were historically understood way before Whittle's patent (1930) [5] but the materials' technology was not ready to support the extreme working conditions that characterize these engines. The structure of the turbo-jet designed by Whittle contained all the basic elements still present in today's gas turbines. Figure 1.1 illustrates the basic elements of a turbo-jet engine.

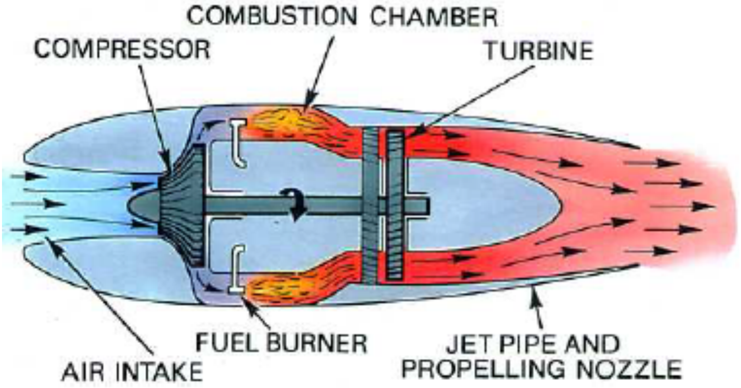

Figure 1.1: Turbo-jet engine basic elements (from [90])

The main body consists of two rotating elements (compressor and turbine) coupled with a frontal air intake, a combustion chamber, and a nozzle. Among the available aeronautical propulsion systems, the jet engine is suitable for civil and military applications in atmospheric air; the fluid is driven through the intake and compressed. The combustion chamber provides heat energy to the main flow at constant pressure; the gases then expand in the turbine's sections: the force exerted over the surface of the rotating blades makes the shaft rotate around the machine axis, converting into mechanical power the high enthalpic content of the flow (Figure 1.2). The exhaust gases are accelerated in the nozzle and released into the atmosphere, providing the required thrust.

The jet engine operates according to Joule's thermodynamic cycle (Figure 1.3): the work w produced in the expansion sections is proportional to the maximum temperature of the cycle T_3. In equation 1.1, the mechanical losses of compressor and turbine are represented by the mechanical efficiency η_{mc} and η_{mt} respectively; the thermodynamic efficiency of these turbomachines are the terms η_c and η_t. By increasing the maximum temperature T_3, the heat introduced in the cycle increases

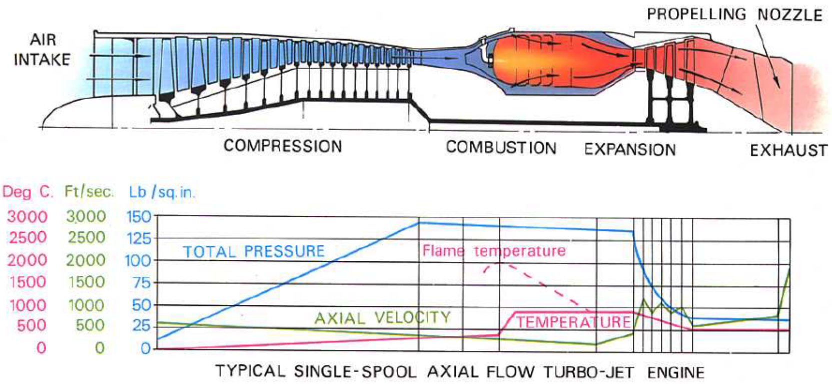

Figure 1.2: Turbo-jet engine sections and variation of fluid properties (from [90])

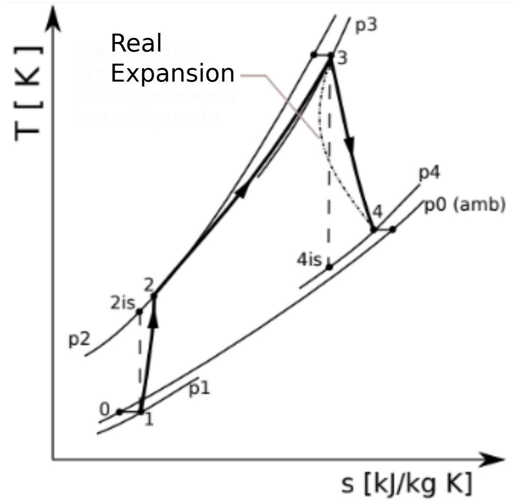

Figure 1.3: Joule working cycle for a jet engine

thus leading to a higher value of work produced, being the other parameters, such as pressure ratios and efficiencies, equal.

$$w = \eta_{mt}\eta_t w_t - \frac{w_c}{\eta_{mc}\eta_c} \text{ where } \eta_t = \frac{T_3 - T_4}{T_3 - T_{4is}} \text{ and } l_t = c_p \cdot (T_3 - T_4) \tag{1.1}$$

The theory faces technology limitations in real life: the blading system inside the jet engine is made out of superalloys (typically Nickel-based and Titanium-based for turbines and compressors respectively) whose melting point is close or lower than the typical temperature values at the outlet section of the combustion chamber. This is one of the most important limitations and challenges for the turbo-jet design: the expansion stages are subject not only to mechanical but also to extreme thermal stresses. Two strategies commonly used to protect the high-pressure turbine (HPT) blades against the high-temperature distributions are Thermal Barrier Coating (TBC) and film cooling systems (internal and external to the blade's surface). Extensive experimental studies were carried out [72, 91, 115, 15] to improve the initial design of the cooling system, but the complexity of the real system [126] along with manufacturing tolerances and uncertain operating conditions do not allow to fully prevent the damage of these components. More details about the common reasons behind the blade's failure are reported in the following Section.

1.3 Components Failure and Performance Prediction

Component failure analysis is a subject that aims at understanding the causes behind damage and unforeseen in-service performance deteriorations. This topic is particularly important for aero-engine components. Once removed from the machine, for example during a full-engine overhaul, the component is thoroughly inspected. If the component is prematurely showing signs of plastic deformation, shape deviations, erosion, and oxidation, this is the first tangible hint for the blade designer to understand the shortcomings of the original design intent (DI). The design of aeronautical components always includes a prediction of the time intervals in which the different kinds of damage and deteriorations are expected to occur.

In addition, a periodic sanity check is performed during the component's life to assess their status inside the engine. This detailed scheduled maintenance minimizes the occurrence of unexpected failures during service, but the chance of damage occurring due to unexpected operating conditions or other unforeseen causes still exists [21]. Automated non-destructive inspection tools such as the one provided by borescope analysis [123, 120] can be used in industry to quickly assess the external damage once it is already visible. Each component is characterized by typical failure modes [70, 13, 32]: in the case of HPT rotors, the modes are visible in the form of creep, volume loss along the upper surface of the blades, or distortion of the rotor shroud. An example of a damaged *squealer tip* is illustrated in Figure 1.4. Visual analysis can also be used to inspect for a chemical attack, which is usually due to corrosion and sulfidation. In addition to the cyclic centrifugal stress, strong vibrations are always present during the engine's operation. In regards to the thermal aspect, an inadequacy in film cooling effectiveness can be critical and lead to blade failure [70]. This is true for all jet engines, both for the civil and military markets. In fact, military applications are often characterized by even harsher in-service conditions, and do not follow well-established scheduled flying hours, so the expected time window of sanity-check and component removal for military engines happens earlier compared to civil engines [61].

Extensive studies have been conducted to identify the principal aerothermal loss mechanisms of modern aero-engine components, and in particular one of the most critical ones, which is the HPT rotor blade. In this regard, the flow behavior around

Figure 1.4: Damaged high pressure turbine blade

the tip region of the blade is widely known to be of great impact on the overall blade aerothermal performance [41]. Geometric deviations from the nominal design, in this region of the HPT rotor blade's geometry, can have a remarkably detrimental effect on the whole engine's performance. For this reason, it is of great interest in the industry to produce increasingly accurate damage classifications for real, after-service components and related causes [53]. It is also vital to understand ad quantify the amount of performance loss that happens as an effect of these shape deviations. Experimental analyses are often carried out in rigs that replicate a simplified version of the real system, and nonetheless can be very expensive. In recent years, predicting the component's performance in the presence of geometric deviations from nominal, high-fidelity numerical simulations has gained more and more attention and nowadays represents a well-established part of the jet engine design process. These numerical investigations are performed via Computational Fluid Dynamics (CFD) to assess performance variations of components [87, 12, 57, 58] and provide insight on the reasons behind their failure. CFD analyses have been used to model the effects of erosion on the performance of HPT blades [128, 129] and compressors [8], as well as the effects of hot corrosion on the blade's tip [94, 30]. Erosion modeling in the blade tip region represents a challenge [27] because of the complexity that usually characterizes the geometries, and a large number of uncertain variables involved [86].

Shortcomings in the film cooling effectiveness can cause unexpectedly high temperature on the blade surface, particularly near the tip, with a consequent dramatic acceleration of the erosion dynamics. Experimental [73] and numerical studies [49, 14, 64, 112, 29] have been carried out with the intent of modeling the often intricate internal cooling ducts and finding an optimal setup, able to ensure the achievement of the desired level of effectiveness for the external cooling. It is the duty of the blade designer not only to avoid failure of the components, but also to learn from them in case they take place, and use the (gained) knowledge to improve the design.

Many methodologies can be followed to optimize a design intent shape, but in general, they belong to one of the following two categories: deterministic or stochastic. The difference between these two is that the first one is only aimed at maximizing the component's nominal performance, that is the performance of a component whose design variables and parameters (such as geometrical dimensions, operating conditions, etc.) are assumed to be fixed at their nominal values. The stochastic approach, on the other hand, tackles the optimization problem in a much more realistic hypothesis that the component will operate with variable (uncertain) conditions and geometrical dimensions, caused either by manufacturing variations or by changes occurring during the life of the component. This means that the uncertainty characterizing the shape of the component and its operating conditions needs to be considered during the design process. To achieve meaningful results, the uncertainty affecting the component's performance needs to be accurately quantified **(uncertainty quantification)**. Then, the performance variability that is associated with the observed geometrical or operational (input) variability needs to be evaluated **(uncertainty propagation)**. Finally, a design solution that minimizes the variability in performance in the presence of the given input uncertainties needs to be selected **(robust optimization)**. In essence, a deterministic design aims at improving the nominal performance of a component or system, while a stochastic optimization has the objective of improving not only their nominal performance, but also their variability, which is often expressed as a combination of the different moments of a probability density function. This often means that a robust design solution will not have the "peak" performance of its deterministic equivalent in nominal conditions; however its performance will be more resilient to the inevitable variations experienced during the life of the component.

1.3.1 Motivation and Outline of the Thesis

This project is part of a wider investigation performed on a set of 200 HPT rotor blades, dismounted from four engines after a certain number of working hours, all characterized by in-service and manufacturing variations. The initial set of data consists of the laser scans (renamed GOM scans by the company providing the technology [2]) of the blades. A first visual inspection highlighted a relevant volume loss along the rim, in addition to the likely plastic deformations experienced during operation. The aim of this work is to quantify the shape variability due to manufacturing and in-service deterioration, estimate its effect on the performance of the rotor, and suggest an alternative design solution, less sensitive to the given uncertainties, by means of robust optimization. A schematic of the different steps of this work is presented in Figure 1.5.

The Thesis is organized as follows. Chapter 2 is dedicated to a presentation of the relevant literature, as well as the methods used for uncertainty quantification, propagation and robust optimization. The results of the uncertainty quantification

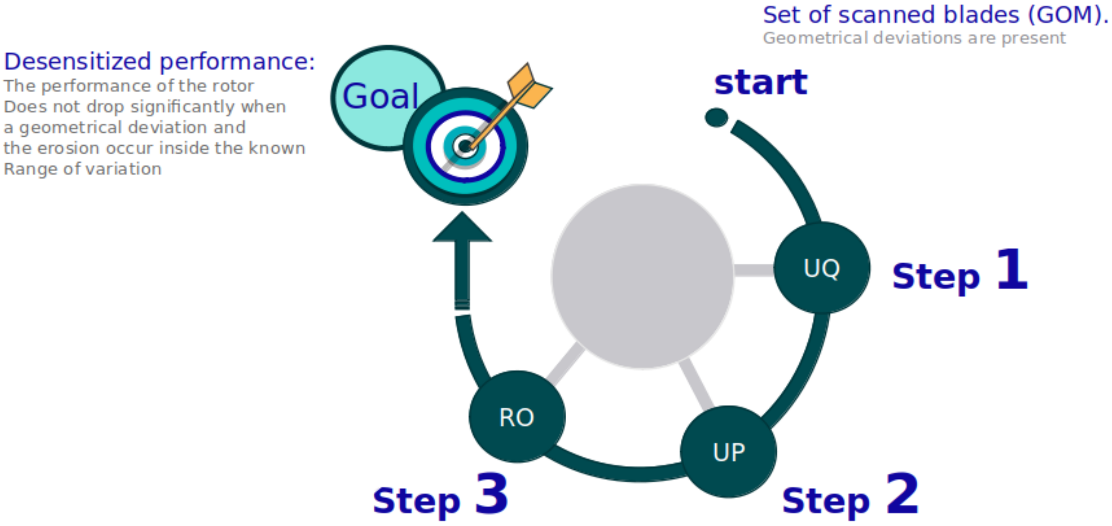

Figure 1.5: Overview of the project heuristics

on the set of real blades are detailed in the third chapter, while the fourth chapter contains the results of the uncertainty propagation, which is the analysis of the variability in performance due to the geometric uncertainties presented in the previous chapter, as well as an identification of the most influential ones. Chapter 5 focuses on a series of optimization runs performed with the aim of improving both the nominal performance of the rotor, and their variability. Chapter 6 provides the final conclusions and recommendations for future work.

Chapter 2

Background

2.1 Robust Design

The design of jet-engine components is characterized by a strong demand for high performance, reliability, long-term life requirements, low fuel consumption, and high safety levels. The final products are the result of a complex and long design process where the number of the variables involved is large. A classical approach to the design of the components takes into account only nominal values of quantities of interest; this point of view does not include the statistical deviations of the design variables with respect to the expected, nominal values. During the real life of the jet engine, the uncertain variables are numerous: unit-by-unit uncertainty is measured [84], due to manufacturing deviations, [17] in the final shape of each component; external factors are also present, such as variations in operating conditions during experimental measurement in laboratories [114, 7] or during the in-service period, leading to unexpected performance.

In general, all the causes of discrepancies directly related to the component, such as its shape and the operating conditions are classified as *aleatory* uncertainties [79]. This type of uncertainty is not the only one affecting the performance. Thanks to the availability of computational resources, it is common nowadays to use numerical and analytical tools to predict the components' behavior; this is pursued via machine learning techniques [85], numerical and analytical models: normally they need to be fed with information or constants and their values should be chosen properly to accurately describe the component behavior. When this knowledge is limited, because of the lack of experimental data, for example, it is difficult to predict the components' performance with accuracy [95]. The uncertainties related to the lack of knowledge are classified as *epistemic* [79].

The identification and the inclusion of the uncertainties in the early stages of component design can make a difference: the global performance can be desensitized with respect to the uncertain factors; when the uncertainties are taken into account before and during the optimization process, this becomes a robust design

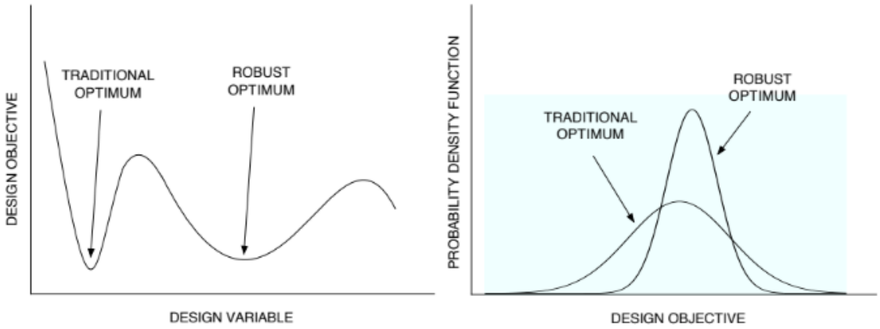

Figure 2.1: Probability density function comparison: robust and classical design [34]

optimization (RO) heuristics. The final aim of the process is to desensitize the performance of the components with respect to the typical noise factors. The statistical variation of the uncertain variables can be quantified and their trend described by a probability density function (PDF); the same logic can be repeated for the component response: given a metric of interest, for example, the efficiency of a blade, a statistical variation and its corresponding probability density function can be estimated. The difference between a desensitized component and another designed via classical approach (i.e. more sensitive to the noise factors) is represented graphically in the probability density functions of the metric of interest shown in Figure 2.1 [34]. Desensitizing the performance leads to a smaller value in variance and the choice of an optimum located in a "flatter" region of the design space, with respect to a traditional optimum; when the variation in the uncertain variables occurs, a mitigation in the drop of the objective function is experienced.

A unique list of mathematical steps that define the RDO methodology does not exist, but in general, it can be divided into three main processes [84]:

- Uncertainty Quantification (**UQ**): the key uncertain parameters are identified and their statistical variation is quantified;
- Uncertainty Propagation (**UP**): this step aims to determine the effect of all the noise factors on the performance, by propagating the uncertainty of the key parameters with the help of a model;
- Robust Optimization (**RO**): the solution that minimizes the variability in the performance due to the presence of the above uncertain parameters is found.

2.1.1 Uncertainty Quantification and Propagation

Small shape variations are normally present in modern jet-engine components, caused by manufacturing variations [55] or in-service deformation due to mechanical stress [22] and thermal loads [89, 74]. Rotating parts such as the blading system in fan, compressor and expansion stages are all characterized by a small gap between the tip of the blade and the upper casing. This geometrical parameter is a perfect example of uncertain variable which can significantly influence the performance. An important contribution that shows how small variations can lead to a substantial degradation in performance can be found in the work of Freeman [31]: the author carried out experimental and numerical investigations on the influence of the tip gap on the global efficiency of a compressor; this small passage, around 1% of the total blade span value, can lead to an increase of suction side loading (visible in the pressure coefficient diagram) and a degradation on the nominal efficiency of about 1.4%. The tip configuration [131, 19] and the variability of the gap is a crucial feature feature for HPT blades as well: the expensive numerical study carried out by Zou *et al.* [132] focused on the comparison between flat and squealer tip; for both configurations, it was shown a drop in stage efficiency of about 0.5% when the rim height, expressed as a percentage of the blade span, goes from 0.6% to 2.2%. The variability of the winglet geometry of a HPT blade has been demonstrated to influence not only the aerodynamics but also the heat transfers [47]: Yan *et al.* [127] decreased by the 15% the heat transfer coefficient by varying only the suction side of winglet; analogue considerations are found in the work of Saha [93] where a minimization of heat transfer coefficient was pursued via pressure side winglet geometrical variations. An additional source of uncertainty is given by the positioning of a component inside the engine; Tao *et al.* [113] focused their attention on the misalignment effects of a HTP blade endwall: along the lower platform of the blade it is normal to have slots for secondary inlet flows and a variation of 2 degrees in this flow direction leads to a drop of film cooling effectiveness of around 12%.

The Uncertainty Propagation can be studied by following two main classes of approaches: **deterministic** and **probabilistic**.

The former group collects heuristics whose common aspect is the evaluation of the system response in given points of the design space. The *interval analysis* [88] aims to determine the limits of the design space identifying the conditions that lead to the worst drop in performance; the expansion of Taylor series around a nominal point is among the deterministic approaches: Abernathy *et al.* [7] identified in the experimental measurements the main cause of error in the performance predictions and propagated the uncertainties via Taylor series. Sensitivity derivatives [20, 107, 42] have as main purpose the calculation of the derivatives of the objective function with respect to the uncertain variables, in the same fashion as in a first order Taylor series.

A statistical approach to the uncertainty propagation can be done via probabilistic methods where the the calculation of the PDF of the metric of interest is the main focus. A random sampling strategy inside the design space, such as Monte Carlo, can estimate with an excellent approximation the statistical moments characterizing the data set. An interesting application of Monte Carlo is present in the work of Wang *et al.* [119], where this statistical approach is used for a case of a stator vane subject to film cooling effectiveness variations due to uncertainty in the inlet boundary conditions. The authors propagated the uncertainties via a neural network surrogate model whilst Monte Carlo was used to calculate the response statistics. Monte Carlo strategy is used also in the recent work of Iglesias *et al. Iglesias*: the authors aimed to find the relationship between the mean time to failure (MTTF) characterizing the engine with the time to failure (TTF) associated to each single component; the propagation was performed via a score function method whilst the calculation of local probabilistic derivatives was performed via Monte Carlo. In general, the drowback of Monte Carlo is that a high number of samples is needed leading to a high computational cost in practical applications. The moment methods [82], are based on the expansion performed via Taylor series around a point and provide the mean and variance of the objective functions for first or second order truncated Taylor expansion.

When the complexity of the system does not allow to have a unique simple expression to describe its performance, a surrogate model can be constructed: the Polynomial Chaos Expansion (PCE) [100] can be used as a propagation technique and can provide a good approximation of the target function; it is generally used when statistical (PDFs) or experimental data is available. Polynomials are not only handy and quite intuitive, they are also easily differentiable; in the aeronautical sector, this strategy is widely used for the design and the performance improvement of simple geometries [38, 125] or more complex test cases such as a real fan blade [39]; the distribution of quantities of interest such as temperatures in a jet engine can be modeled starting from sparse experimental data [102, 99], as well as the heat transfer in a turbine disc [121]; the design of engine complementary instrumentation, such as stagnation temperature probes, can be desensitized with respect to typical manufacturing variations [97].

PCE enables to calculate the statistical moments from the coefficients of the expansion and to perform a sensitivity analysis via Sobol Indices; the recent work of Shi *et al.* [108] focused on three main features of the squealer tip of an HPT blade, namely tip gap, gutter depth and rim corner radius. These uncertain variables were propagated associating Gaussian distributions to the first two and a uniform distribution to the third; the calculated Sobol indices indicated the tip gap as the most influential parameter for the aerodynamic performance. The computational cost of the PCE depends on the number of input variables involved (*curse of dimensionality*); when dealing with problems with a high number of uncertain variables this represents a problem.

In recent years the use of adjoint solvers gained particular attention because they provide the gradients (first order derivatives) of the target function with respect to the uncertain input variables at a computational cost comparable with that of a normal CFD run. In general, two main approaches have been developed: continuous [81] and discrete adjoint [40, 16, 124, 28], this latter widely available thanks to the availability of automatic algorithmic differentiation tools [9]. This mathematical operator is widely used to perform sensitivity analyses: the work of John *et al.* [48] uses the mesh sensitivity in a optimization loop in order to adapt the mesh clustering the cells and changing their size thus improving the local flow resolution. A similar analysis was carried out by Vivarelli *et al.* [118], where the nodes of the mesh were adapted based on the adjoint sensitivity. A hybrid heuristic was used by Schmidt [96] for the sensitivity of a high pressure compressor: the adjoint run provided with the first order derivatives and after that the non-linear effects of the target functions were calculated via Monte Carlo approach.

The designer, thanks to the availability of the gradients, is able not only to perform a sensitivity campaign but also to drive the optimizer towards the direction of the optimum [66, 33]. Caloni *et al.* [105, 18] carried out an extensive research for optimization of HPT blades by means of adjoint gradients and mitigating, thanks to the optimized shape, the effect of the swirl flows in the stage. An improvement in HPT stage efficiency, even if small, was achieved in the work of Lei *et al.* [23] driving the optimizer using a a continuous adjoint solver. Sabater *et al.* [92] coupled a non-intrusive surrogate with the adjoint in order to improve the aerodynamic performance of a 2D airfoil, using as the target function the drag.

2.1.2 Robust Optimization

The deterministic approaches calculate a unique value of an objective function $f(x)$ from the nominal values of the design variables; the final outcome of this kind of analysis lacks in statistical meaning, and when uncertainties are present a substantial difference with respect to the expected system response can occur. In order to pursue a robust design, an appropriate non-deterministic strategy [45] should be used to determine the expected value $E(f(x))$ and the variance $var(f(x))$ of the objective function $f(x)$; after that, different mathematical approaches can be pursued to minimize $E(f(x))$ and $var(f(x))$ but two main groups can be identified: multi-objective optimization in which the statistical moments are minimized simultaneously and the alternative, represented by the use of weighting coefficients (adopted to re-formulate the problem into a series of single-objective problems); the computational costs is lower in the second case, but in the same time attention needs to be payed to the choice of the weights. The challenging aspect in using this strategy is that, most of times, it is difficult to decide which objectives are more important than others a priori.

Das *et al.* [26] and Indraneel [25] analyzed and proposed the *Normal-Boundary intersection* method to solve a generic multi-objective optimization problem. This strategy aims to generate a well-distributed Pareto optimal set of points from a a set of uniformly distributed parameters: this first aspect represents an advantage compared to weighting methods which are not able to achieve this purpose; a significant advantage is also the independence with respect to the magnitude of the particular function value. However, considering that this peculiarity is generated by a derivative-based approximation method, there is a consequent limit for the application of this procedure only to cases in which the designer has knowledge of the function's derivatives.

In recent years, a new class of numerical strategies has been developed to overcome the limitation represented by a-priori choice of weights in multi-objective optimizations. The *generate-first-choose-later* approaches allow the designer to carry out a-posteriori selection of optimal designs; among this group of strategies the Normal Constraint (NC) and its updated version Smart Normal Constraint (SNC) has the interesting advantage to translate a multi-objective optimization problem to single-objective problem with a set of additional constraints; this is translated to a reduction in the size of the search region and more evenly spaced points in the Pareto set. The work of Cresenti *et al.* [24] focused on this numerical strategy and carried out a multi-objective Solid Isotropic Material with Penalization (SIMP) optimization of a full-scale wing. The authors coupled this strategy with a Method of Moving Asymptotes (MMA) optimizer, due to its superior convergence quality. The objective functions for the case under study were compliance and eigenfrequency of the wing. Minimization of compliance and maximization of fundamental frequency were achieved by controlling the pseudo-density parameters of the wing ribs, while the performance assessment of the full-scale wing was performed via Altair OptiStruct code. The results along the Pareto front showed an interesting smooth passage from the optimal shape associated to minimum compliance and the one associated to maximum eigenfrequency.

Among the widespread industrial solutions, the 6σ method [83], being σ the standard deviation, circumscribes the system performance around the mean value and considers a variation six times the standard deviation; this method is intuitive because the chosen range is linked to a high probability to find the random event below the PDF's curve. The downside of this application is that the cited range is associated to a failure probability of 0.0000001% and for the majority of the cases, it means a measure of uncertainty outside the industrial tolerances [103].

A multi-objective optimization, which minimizes the mean and the variance of the pressure losses in a real Rolls-Royce compressor blade was done in the work of Kumar *et al.* [106]. A Design of Experiments (DoE), defined as the set of normally distributed noise factors, was used to model several blades deformed with Hicks-Henne functions. The computational cost was reduced by using a surrogate model with a Gaussian stochastic process: the system was approximated as the sum of two main contributions, a global model and a Gaussian random function characterized by zero mean and non-zero covariance. The final Pareto front was chosen using the NSGA method. The comparison of one of the desensitized blade (with respect to geometrical parameters) with a blade which had been optimized using a deterministic method showed a performance improvement away from the nominal conditionswhere the deterministic blade presented better performance.

In turbomachinery industrial applications, a large number of works sets the adiabatic efficiency as the objective function both for expansion and compression stages. Kato *et al.* [52] proposed the maximization of the mean efficiency for the supersonic M1 impulse turbine, mixing a probabilistic method such as polynomial chaos with a deterministic approach. The mean efficiency value was bounded inside a 3σ range. The optimization problem led to a small increase of the nominal efficiency as well as its robustness.

It is a good practice to use non-dimensional curves which describe the behavior of compression and expansion stages as function of pressure ratios and non-dimensional mass flow. In the work carried out by Ghisu *et al.*[37] the ratio between inlet and outlet total temperatures of the compression system in a three-spool aero-engine has been selected as the control variable with a known PDF, whilst the efficiency and the surge margin were the objective functions to be maximized; the procedure mantains a low computational cost by using weights in the optimization model. Two objective functions were selected: a simultaneous control of the performance associated to nominal and off-design conditions was performed; the bounds of the expected efficiency is fixed using weights which promote the performance and surge limit increase; the authors underline that this kind of study gives better information about robustness, because a traditional mono-objective procedure, without the inclusion of a figure of merit for the off-design condition, does not allow to compare the performance gap between optimized and baseline off-design conditions, so the designer has a partial information regarding an effective improvement of the system behavior.

The choice of the parametrization, thus the set of optimized variables, can have a significant impact on the result of the design process. It is possible to reach optimal solutions, meeting the requirements, however the output can show different optimized shapes and performances. This case is widely argued by Seshadri *et al.* [101] using two different design spaces: one defined by a set of aerodynamic parameters such as lean, recambering and solid rotation of the blade; the second set is represented by local perturbation of the blade, performed via Hicks-Henne bump functions. The multi-objective optimization results showed an improvement in mean the efficiency and its variance for both design spaces, but the one associated with Hicks-Henne bump space provided a smaller improvement.

Langmaak *et al.* [62] proposed an interesting RO where the aim is to determine the best engine topology (turbofan, turboprop or prop-fan) and the optimal cruise speed to minimize the *direct operational costs* of the aircraft. In this study, the related fuel cost and CO_2 uncertainties were quantified. A probabilistic approach was chosen instead of a deterministic one. The objective function is the direct operating cost and the DoE is stated by a heterogeneous list of parameters: cruise Mach or maximum pressure ratio, flight conditions such as the maximum altitude or mission fuel and geometrical variables such as fan diameter or tip blade maximum velocity.

Zhiying *et al.* [130]'s work aimed to reduce the sensitivity to tip clearance of a turbine blade. The complexity of the system (casing shroud, blade and turbine disk) was reduced by approximating the behavior of each sub-system and calculating a set of response surfaces from the run of finite-element based simulations. Surrogates were used to generate a global model from which the moments were extrapolated. The optimization cost was reduced by using weights functions and minimizing a linear combination of mean and variance. The predictions of this model were validated against a global Kriging surrogate model and a maximum relative error below 0.97% was found.

In engineering, it is common to distinguish between RDO and Reliability-based Design Optimization (RBDO) [43]: while the former is meant to minimize the variability of a target function, the latter selects the optimum with lower probability of failure. A trade-off between the robust optimization and the RBDO is possible as demonstrated by Korelev *et al.* [56]. This work focuses on the usage of Mid-range Approximation Method. The majority of the works which performed a RDO limited the values of the design control variables. The risk associated to this strategy is to locate the optimum solutions near the extreme regions of the DOE. In order to reduce this risk, in the recent work of Kamenik *et al.*[50] an enforcement of mean constraint values is present. The authors optimized a HPT rotor by selecting the mean of turbine efficiency and its standard deviation as objective functions. The mean and the variance were determined with a quasi-Monte Carlo method. The optimized blade matched the required constraints, in spite of the smaller accuracy of standard deviations prediction.

The recent work of Martin *et al.*[67] focused on the multi-disciplinary optimization of an axial compressor. The complexity of the problem did not allow to separately treat the mean and the variance of the objective functions (pressure losses measured during off-design operational conditions and nominal ones). Therefore a combination of the statistical moments was used. The optimization was performed using a Genetic Algorithm. Two response surfaces were built by separately running CFD simulations and FEM simulations followed by the construction of a global model. The results show a small increase in aerodynamic efficiency and higher structural robustness.

A large number of studies carried out on engine components aimed to desensitize with respect to typical manufacturing variations: Antinori *et al.* [11] focused the attention of low pressure turbine disc and the secondary flow system passing through it; Martins *et al.* [68] included not only the typical values of manufacturing deviations, but enforced the choice of an optimum shape inside a “safer” range of values, away from the failure condition range. A robust optimization of a compressor blade was carried out by Kumar *et al.* [59], in light of the typical manufacturing variations occurring in the component. A trade-off between the mean and a variance of the aerodynamic performance was possible by combining a Gaussian stochastic process model and Bayesian Monte Carlo simulations to calculate the statistics.

In the work of Karimi *et al.* [51] two optimized shapes for the NASA C3X turbine vane were compared: the former was obtained via deterministic approach, the second via robust optimization where the probability distributions associated to the uncertain operational conditions were propagated via PCE; the maximum temperature as well as its gradient were minimized, leading to a less sensitive geometry.

The work conducted by Vishwanathan *et al.* [117] is one of the few where the structural boundary conditions uncertainties are propagated within a robust topology optimization; the uncertainty is represented by the degree of freedom of some points along the fixed edge of a cantilever wing. The the authors run two optimizations of this component: in order to choose a design away from the aeroelastic instability, the closest natural frequencies of the system (namely the first two) were identified and the gap between them selected as the first objective function to be maximized; the analytical expression of the aforementioned target function was a weighted sum of its mean and standard deviation. Same approach was followed for the second objective function to be minimized, the wing compliance; for both objectives a non-intrusive PCE surrogate was built. The eigenvalues of the wing dynamic response are optimized in the first phase, adopting a modified interpolation scheme for the Bi-Directional Evolutionary Structural Optimization (BESO); for the second optimization was run via Solid Isotropic Material with Penalization strategy, controlling the pseudo-density of each rib inside the cantilever. The results of both optimizations showed an improved performance for the worst case, furthermore a more robust design was obtained.

2.2 Theoretical Background

2.2.1 Polynomial Expansion

In engineering, it is quite common to express the behavior of a system via analytical expressions. Oftentimes, the complexity of the problem does not allow to have a handy or unique expression. In this thesis, the expression linking the aerodynamics of the blades with its shape is not trivial and it has a high added computational cost. However, the relationship between the selected parameters and the metric of interest is still possible via a polynomial expansion.

The general structure of a PCE recalls some aspects of a Fourier series: in the latter, a generic function is reconstructed via sines and cosines; the aim of PCE is to approximate a function of interest using polynomials.

Let's consider X as the set n uncertain variables characterizing a component such as an HPT blade; the uncertainties are represented by all the deviations occurring in geometrical parameters, operating conditions, etc. Each variable in X is subject to a deviation with respect to the nominal value because of the occurrence of a generic random event θ; $X = X(\theta)$ is associated to a statistical variation thus can be described by a probability distribution or in another word a Probability Density Function (PDF) $f(X)$. As mentioned above, it is a common practice in engineering to deal with analytical models which describe the relationship between some input variables (here the uncertain variables in X) and a metric of interest: it can be the rotor efficiency, the inlet capacity, or any other objective function for the designer. Let's call the metric of interest as Y and let's assume we know the functional relationship between a number of uncertain variables X and $Y = Y(X)$. A statistical deviation with respect to an expected value is present also for $Y(X)$ and this can be described by another PDF, $f(Y)$. To expand the uncertain $Y = Y(X(\theta))$, this is assumed to have a finite variance thus Y is a quadratically integrable function (L^2 function). Let's define the vector $\xi(\theta)$ as a random variables support with a well-established probability distribution $W(\xi)$; the easier choice is to select $\xi = X$ but it is not necessary. The polynomial expansion of $Y(\theta) = Y(\xi(\theta))$ can be expressed by the series in Equation 2.1, being a_i the coefficients and the terms $\Phi_i(\xi(\theta))$ orthogonal polynomials.

$$Y(\theta) = Y(\xi(\theta)) = \sum_{i=0}^{\infty} a_i \Phi_i(\xi(\theta)) \tag{2.1}$$

Being Φ_i orthogonal polynomials, the space where they belong is equipped with an inner product defined as in the following equation :

$$\langle \Phi_i(\xi)\Phi_j(\xi) \rangle = \langle \Phi_i(\xi)^2 \rangle \delta_{ij} = \int \Phi_i(\xi)\Phi_j(\xi) W(\xi) d\xi \tag{2.2}$$

The term δ_{ij} is the Kronecker delta, equal to zero when $i \neq j$; the expression in Equation 2.2, in order to be true, puts a constraint on the choice of the orthogonal polynomials Φ_i, depending on the particular PDF $W(\xi)$ [54]. In one-dimensional problems, the choice of the basis of orthogonal polynomials is straightforward. A Gaussian distribution, for example, needs to be associated with the Hermite family of orthogonal polynomials [122]; the Askey scheme for the choice of the best family of orthogonal polynomials is used for other well-established PDF. When dealing with non-standard distributions, it is possible to use their statistical moments and construct an expression for the orthogonal polynomial [80]. Numerical strategies can be used to determine ad-hoc orthogonal polynomials, when dealing with challenging distribution of probability, using a three-recurrence coefficient method [36, 75]. It is more likely, in engineering problems, to have multi-dimensional problems where the uncertain variables ξ_i, influencing the response Y of the system, are multiple and each of them characterized by their own probability distribution $w_i(\xi_i)$. When independence occurs among input variables, the term $W(\xi)$ can be replaced by the product of the aforementioned marginals $w_i(\xi_i)$:

$$W(\xi) = \prod_{i=1}^{n} w_i(\xi_i) \tag{2.3}$$

The basis construction in the case of a multi-dimensional problem is performed via a tensor product among the bases Φ_{ξ_j}:

$$\Phi = \Phi_{\xi_1} \otimes \Phi_{\xi_2} \otimes ... \otimes \Phi_{\xi_n} \tag{2.4}$$

Index Set

As the number of the variables involved increases, the number of the terms in the tensor product in Equation 2.4 grows exponentially: the computational cost becomes too high to justify the application of the PCE. This issue is named as *curse of dimensionality.* A first solution is represented by the observation of the contribution given by each term inside the expansion: in most of the practical applications the most relevant contribution, in order to surrogate the system response, is contained in the low-order terms of the expansion [78], i.e. all the terms in the series of tensor products whose polynomial order is low. The remaining terms do not add relevant information and the approximation provided by the lower order terms can already be considered satisfactory. The *index set* of a PCE contains the selected combination of polynomials according to a curtain rule. The rule defining the basis constructed by a tensor product includes all the possible combinations: this means that, given j uncertain variables, for $j = 1, ..., n$, and their related orthogonal polynomial with order o, all the polynomials whose order respects the condition $|o_j| < o_e$ will be included in the expansion; the number of combinations contained in the expansion is the *cardinality* and in the case of a tensor product it will be equal to $(o_e + 1)^n$. A smaller number of elements can be considered, thus reducing the computational cost, by choosing a different rule such as a total order and hyperbolic cross: the former selects the combinations such that $\sum_j o_j \leq o_e$; the latter is slightly different but can be equivalent to a total order set (with the same order) when the term p in Equation 2.5 is equal to 1.

$$||o_j||_p = \left(\sum_j {o_j}^p \right)^{\frac{1}{p}} \leq o_e \tag{2.5}$$

The cardinality associated to the total order is fixed to $\binom{n+o}{n}$, whilst for the hyperbolic cross it is dependent on the value assumed by p; a graphical comparison among the cardinalities of total order and hyperbolic cross for different values of p is reported in Figure 2.2 [38]. The example reported is for a 2-dimensional problem; the horizontal and the vertical axes show the values of the orders of the orthogonal polynomials associated to each input variable.

The number of elements included in the expansion when choosing an hyperbolic set is smaller for decreasing values of p; when decreasing also the order of the hyperbolic set (equal to 4 in the example of Figure 2.2) with respect to the higher order of the orthogonal polynomials (6 in the example of Figure 2.2), the cardinality and the computational cost decrease even more. In practical cases, the identification of the polynomial expansion order is dictated by the required level of approximation in the uncertainty propagation modeling; the knowledge of the system and the designer's experience help the choice in the truncation of the PCE.

Calculation of Coefficient

One the most challenging parts of a PCE is the calculation of the coefficients a_i in Equation 2.1. As reported in the paragraph above, in order to model the uncertainty propagation via a truncated series, a finite subspace of polynomials is constructed.

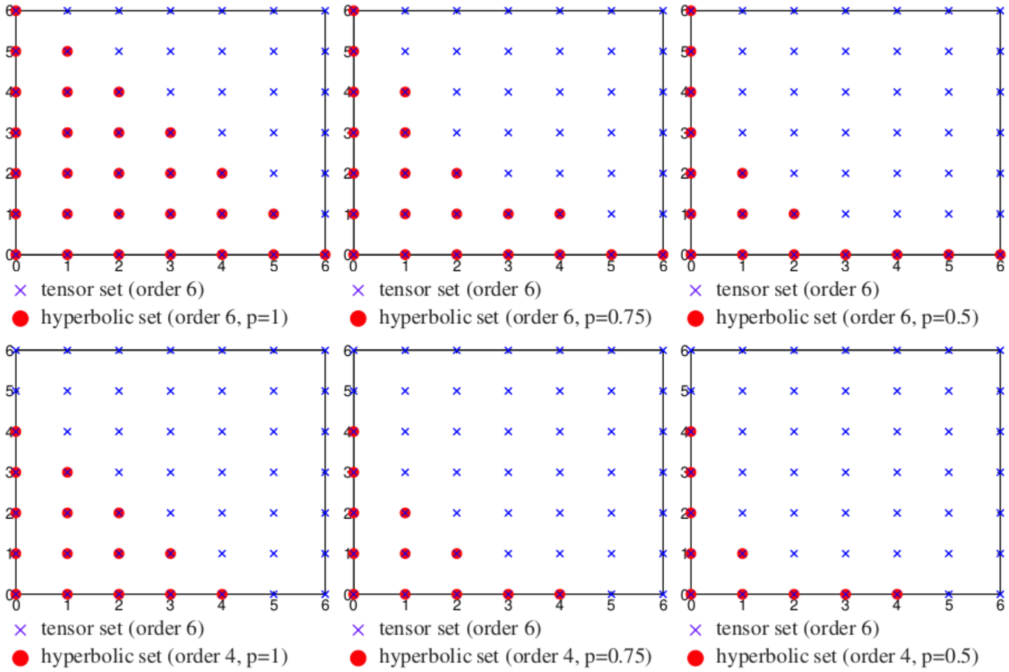

Figure 2.2: Cardinality of a hyperbolic cross set for different values of p, compared with a tensor grid approach in the case of 2-dimensional case and order 6 orthogonal polynomials [38]

From here, two main groups of strategies can be mentioned: Galerkin projections onto the polynomial subspace and non-intrusive approaches where deterministic computations are used to approximate the coefficients. The first group of methods is particularly demanding because it requires a modification of the solvers used to simulate the system. The second group is meant to treat the system as a black box, without any modification to the governing equations. This second class of methods is called Non-Intrusive Polynomial Chaos Expansion (NIPCE) and recently gained attention because of the simpler application with respect to the first class of approaches [38, 75, 35]. The calculation of the coefficient can be performed via a pseudo spectral approach: the system response $Y(\xi)$ is projected on each element belonging to the basis and, given the condition of orthogonality in Equation 2.2, the terms a_i in Equation 2.6 can be calculated via the expression in 2.7, being $\mathbb{E}$ the expectation defined by the properties of the inner product space L^2.

$$Y(\theta) = \sum_{i=0}^{\infty} a_i \Phi_i(\xi) \approx \sum_{i=0}^{o_e} a_i \Phi_i(\xi) \tag{2.6}$$

$$a_i = \frac{\langle Y(\xi), \Phi_i(\xi) \rangle}{\langle {\Phi_i}^2(\xi) \rangle} = \frac{\mathbb{E}\left[Y(\xi)\Phi_i(\xi)\right]}{\mathbb{E}\left[\Phi_i^2(\xi)\right]} = \frac{1}{\langle \Phi_i^2(\xi) \rangle} \int_{\xi} Y(\xi)\Phi_i(\xi)W(\xi)d\xi \tag{2.7}$$

The term defining the variance (denominator in the fraction of 2.7) can be calculated analytically, the same is not true for the numerator. Sampling methods are generally employed to evaluate the unknown term by sampling, for each element inside the expansion, some points inside the distribution $W(\xi)$ and then calculating the expectation $\mathbb{E}\left[Y(\xi)\Phi_i(\xi)\right]$. The sampling strategy can be based on Monte Carlo (classical approach as well as Quasi-Monte Carlo): the advantage is the independence with respect to the problem dimensionality but the downside is represented by the large number of required samples in order to reach a good estimation; even if considered more efficient, also the sampling strategy Latin Hypercube is affected by high computational cost in most of the practical applications. An interesting alternative is represented by the possibility to approximate the integral by means of quadrature rules: Gaussian quadratures solve an integral by approximating it as a finite summation, as reported in Equation 2.8 in the case of a one-dimensional problem.

$$U = \int Y(\xi)W(\xi)d\xi = \sum_{i=1}^{m} w_i Y(\xi) \tag{2.8}$$

The term w_i acts as a weight in the summation. Each well known PDF has a defined set of quadrature points and their associated weights; this logic, used in quadrature rule, is framed as a collocation method. For a more general application, provided that all the involved variables are independent, a n-dimensional quadrature rule can be written via tensor product such as:

$$\sum_{i_1=1}^{m_1} \dots \sum_{i_n=1}^{m_n} Y\left(\xi_{i_1}, \dots, \xi_{i_n}\right) \prod_{k=1}^{n} w_{n_k} = \otimes_{j=1}^{n} U^{i_j} \tag{2.9}$$

The curse of dimensionality affects the quadrature rule as well: as the number of the input uncertainties ξ_i increases, an exponential increase in the number of points in the tensor product of Equation 2.9 is experienced. Several numerical solutions were implemented to deal with this issue. In order to reduce the collocation points [109] it is possible to use a sparse tensor product grid: the full tensor is replaced by a linear combination of lower order quadrature rules, where the growth of points in each one-dimensional rule is controlled by the level of sparsity l. The general formulation of an isotropic sparse quadrature can be written as follows.

$$S(n,l) = \sum_{l+1 \leq i \leq l+n} (-1)^{l+n-|i|} \binom{n-1}{l+n-|i|} \otimes^{n}{}_{k=1} U^{i_k} \tag{2.10}$$

A different point of view in the calculation of the coefficients and in the construction of the PCE is represented by the Least Squares approximation (LSA): the PCE itself is thought to be a system of equations:

$$\begin{pmatrix} \Phi_0(\xi^{(0)}) & \Phi_1(\xi^{(0)}) & ... & \Phi_P(\xi^{(0)}) \\ \Phi_0(\xi^{(1)}) & \Phi_1(\xi^{(1)}) & ... & \Phi_P(\xi^{(1)}) \\ \vdots & \vdots & \ddots & \vdots \\ \Phi_0(\xi^{(N_s)}) & \Phi_1(\xi^{(N_s)}) & ... & \Phi_P(\xi^{(N_s)}) \end{pmatrix} \begin{pmatrix} a_0 \\ a_1 \\ \vdots \\ a_p \end{pmatrix} = \begin{pmatrix} Y(\xi^{(0)}) \\ Y(\xi^{(1)}) \\ \vdots \\ Y(\xi^{(N_s)}) \end{pmatrix} \tag{2.11}$$

N_s is the number of training points sampled from the probability distribution $W(\xi)$. The coefficients of the PCE, given the system in 2.11, are calculated as a minimization problem as follows, being $||.||_2$ the $l^2 - norm$.

$$\tilde{a} = \underset{\mathrm{k}}{\operatorname{argmin}} ||\Phi(\xi)a - Y(\xi)||_2 \tag{2.12}$$

The solution of the linear system requires a number of equations N_s equal or greater than the number of elements contained in the expansion; the oversampling ratio, defined as the ratio between the number of equations N_s and the minimum required to ensure a full rank, cannot be too high because otherwise the increased computational cost does not justify anymore the application of this method.

Among the regression strategies [65, 35, 75], the gradient-enhanced PCE incorporates in the system in Equation 2.11 the information about the derivatives of the objective function $Y(\xi)$: an additional equation can included by considering the variations of the system response with respect to the variation of the uncertain variable (equation 2.13).

$$\frac{\partial Y}{\partial \xi_j}(\xi^{(k)}) = \sum_{i=0}^{N_s} a_i \frac{\partial \Phi_i}{\partial \xi_j}(\xi^{(k)}) \tag{2.13}$$

Recalling the system of equations seen in 2.11, the new system for a gradient-enhanced strategy has the general form reported in Equation 2.14.

$$\begin{pmatrix}
\Phi_0(\xi^{(0)}) & \Phi_1(\xi^{(0)}) & ... & \Phi_P(\xi^{(0)}) \\
\Phi_0(\xi^{(1)}) & \Phi_1(\xi^{(1)}) & ... & \Phi_P(\xi^{(1)}) \\
\vdots & \vdots & \ddots & \vdots \\
\Phi_0(\xi^{(N_s)}) & \Phi_1(\xi^{(N_s)}) & ... & \Phi_P(\xi^{(N_s)}) \\
\partial_0\Phi_0(\xi^{(0)}) & \partial_0\Phi_1(\xi^{(0)}) & ... & \partial_0\Phi_P(\xi^{(0)}) \\
\partial_1\Phi_0(\xi^{(0)}) & \partial_1\Phi_1(\xi^{(0)}) & ... & \partial_1\Phi_P(\xi^{(0)}) \\
\vdots & \vdots & \ddots & \vdots \\
\partial_n\Phi_0(\xi^{(0)}) & \partial_n\Phi_1(\xi^{(0)}) & ... & \partial_n\Phi_P(\xi^{(0)}) \\
\partial_0\Phi_0(\xi^{(1)}) & \partial_0\Phi_1(\xi^{(1)}) & ... & \partial_0\Phi_P(\xi^{(1)}) \\
\partial_1\Phi_0(\xi^{(1)}) & \partial_1\Phi_1(\xi^{(1)}) & ... & \partial_1\Phi_P(\xi^{(1)}) \\
\vdots & \vdots & \ddots & \vdots \\
\partial_n\Phi_0(\xi^{(1)}) & \partial_n\Phi_1(\xi^{(1)}) & ... & \partial_n\Phi_P(\xi^{(1)}) \\
\vdots & \vdots & \ddots & \vdots \\
\partial_0\Phi_0(\xi^{(N_s)}) & \partial_0\Phi_1(\xi^{(N_s)}) & ... & \partial_0\Phi_P(\xi^{(N_s)}) \\
\partial_1\Phi_0(\xi^{(N_s)}) & \partial_1\Phi_1(\xi^{(N_s)}) & ... & \partial_1\Phi_P(\xi^{(N_s)}) \\
\vdots & \vdots & \ddots & \vdots \\
\partial_n\Phi_0(\xi^{(N_s)}) & \partial_n\Phi_1(\xi^{(N_s)}) & ... & \partial_n\Phi_P(\xi^{(N_s)})
\end{pmatrix}
\begin{pmatrix} a_0 \\ a_1 \\ \vdots \\ a_p \end{pmatrix}
=
\begin{pmatrix}
Y(\xi^{(0)}) \\
Y(\xi^{(1)}) \\
\vdots \\
Y(\xi^{(N_s)}) \\
\partial_0 Y(\xi^{(0)}) \\
\partial_1 Y(\xi^{(0)}) \\
\vdots \\
\partial_{N_s} Y(\xi^{(0)}) \\
\partial_0 Y(\xi^{(1)}) \\
\partial_1 Y(\xi^{(1)}) \\
\vdots \\
\partial_{N_s} Y(\xi^{(1)}) \\
\vdots \\
\partial_0 Y(\xi^{(N_s)}) \\
\partial_1 Y(\xi^{(N_s)}) \\
\vdots \\
\partial_n Y(\xi^{(N_s)})
\end{pmatrix}
\tag{2.14}$$

For each point, an additional number of equations, equal to n, is included. In order to find a solution an over-determined system is built (given a on oversampling ratio ζ). In the recent work of Ghisu *et al.* [35], a novel approach for the calculation of the coefficient in gradient-enhanced heuristics was developed: the system of equations in 2.14 can be written by separating four main contributions:

- The matrix A, collecting all the terms $\Phi_i(\xi^{(j)})$ of the polynomial expansion
- The matrix C, collecting the derivatives of the terms in A
- The array b, collecting the model evaluations
- The array d, collecting the derivatives of the elements in b

The resulting problem can be summarized with the following expression:

$$\tilde{a} = \underset{\text{k}}{\text{argmin}} || \begin{pmatrix} A \\ C \end{pmatrix} a - \begin{pmatrix} b \\ d \end{pmatrix} ||_2 \tag{2.15}$$

The number of sub-sampled points, in order to get a full rank for $\binom{A}{C}$ is found iteratively: in each iteration the rows of A and C are selected only if the rank increases; the loop continues until a full rank is obtained.

Statistics and Sensitivity Analysis

Once the PCE surrogate is built, the calculation of the statistical moments is trivial:

$$\mathbb{E}\left[Y(\xi)\right] = a_0 \tag{2.16}$$

$$\sigma^2\left[Y(\xi)\right] = \sum_{i=1}^{P} a_i^2 \tag{2.17}$$

The moments of higher order can calculated in the same fashion; a sensitivity analysis can be also performed via Sobol indices [110]: this variance-based approach calculates the variability of the system response $Y(\xi)$ with respect to one uncertain variable ξ_i (taken from the n-dimensional array $\xi = \xi_1, \xi_2, ..., \xi_n$) as in 2.18, where the numerator is the variance of the objective function with respect to ξ_i, different from the denominator which is instead the variance with respect to the entire set of uncertain variables. Second order Sobol indices can be calculated as well (Equation 2.19) and they take into account the interaction between a couple of uncertain variables ξ_i and ξ_j.

$$S_i = \frac{\sigma^2(Y(\xi_i))}{\sigma^2(\xi)} \tag{2.18}$$

$$S_{i,j} = \frac{\sigma^2(Y(\xi_i, \xi_j))}{\sigma^2(Y(\xi))} \tag{2.19}$$

Correlation between Input Variables

The expression in Equation 2.3 is not true when the uncertain variables are correlated: the joint PDF $W(\xi)$ cannot be calculated a priori and this topic still represents a research challenge nowadays. A correlation may be present in the initial set of data [116]. Some examples are experimental data taken with calibrated instruments with the same batch wires; correlation between uncertainties can also be introduced when converting an electrical potential measurement to a pressure or a temperature value: this is because these two values are obtained by setting initial reference values of pressure and temperature respectively. Correlation is a measure of the relationship between two or more variables, different from dependence. The latter implies the manifestation of an event, given the occurrence of another independent one; correlation, instead, is indicative of a tendency of two sets of data that follow a preferential trend.

Neglecting the correlation among uncertain data may cause misleading statistics, such as variance overestimation. When dealing with correlated data, it is still possible to construct a polynomial expansion [46]: this can be achieved by mapping the initial set of data from the space where they are correlated (blue points in Figure 2.3) to a new space where they are independent (Nataf and Rosenblatt transforms are

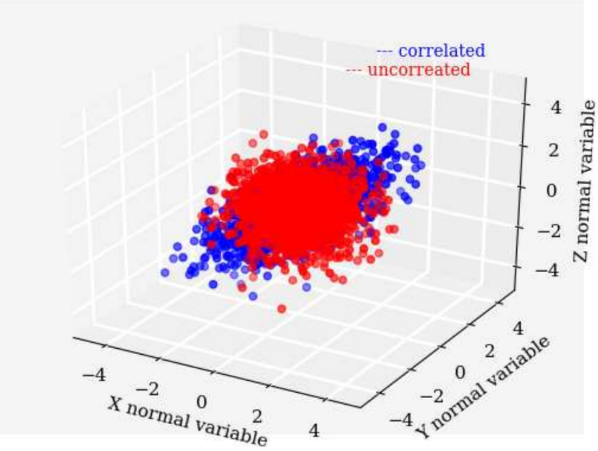

Figure 2.3: Example of independent normal distribution (red) and correlated guassian distributions (blue)

used to this aim) or via orthogonalization methods such as Graham-Schmidt. The Nataf transform can operates with different type of well known statistical distribution, under the assumption that the cumulative density function for the initial set of input variables is available. Given a set of random variables $X = x_1, x_2, ..., x_n$ characterized by a marginal probability density functions $w_i(x_i)$ and the corresponding cumulative density functions $CDF_i(x_i)$ for an index $i = 1, ..., n$. The tail transformation [6] enables to obtain a set of normally distributed Gaussian samples $Y = y_1, y_2, ..., y_n$ according to Equation 2.20; the Gaussian distribution described by Y is characterized by a cumulative distribution function CDF_{NG} and the inverse of this latter CDF_{NG}^{-1}.

$$\begin{cases} CDF_{NG}(y_i) = CDF_i(x_i) \\ y_i = CDF_{NG}^{-1}(CDF_i(x_i)) \end{cases} \tag{2.20}$$

Let's assume a correlation among the initial set of data X, quantified for each couple of arrays X_i, X_j as in formula 2.21; in the same fashion the correlation among the normal Gaussian distribution is described by the correlation coefficients ρ'_{ij}. The relationship between the correlated set of data [6] can be expressed as reported in Equation 2.22.

$$\rho_{ij} = \frac{cov[X_i, X_j]}{\sigma_{X_i,X_j}} \tag{2.21}$$

$$\frac{1}{\sigma_{x_i,x_j}} \int_{-\infty}^{\infty} \int_{-\infty}^{\infty} \left(CDF^{-1}(CDF_{NG}^{-1}(y_i)) - \mu_{x_i}\right) \left(CDF^{-1}(CDF_{NG}^{-1}(y_j)) - \mu_{x_j}\right) \mathcal{P} dy_i dy_j \tag{2.22}$$

The correlation matrices which collect the correlation coefficients for X is renamed ρ whilst the one associated to the correlation in Y is renamed ρ'. In Equation

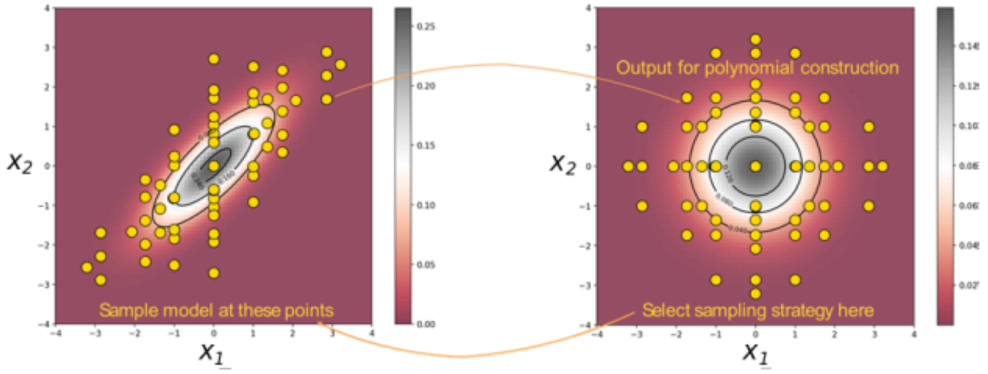

Figure 2.4: Nataf transform for correlated data in PCE [98]

2.22 the joint PDF for the Gaussians Y_i, Y_j is given by $\mathcal{P} = PDF_{joint}(y_i, y_j; \rho'_{ij})$. In the expression above the unknown terms are represented by the correlation coefficients ρ'_{ij}; when the marginals associated to X are Gaussian, then the calculation of the unknown terms is trivial, being the correlation matrices $\rho = \rho'$. When dealing with other well known probability density functions, it is necessary to go through an iterative process in order to calculate each correlation coefficient ρ'_{ij}. For the calculation of the polynomial expansion in the case of correlated samples, the iterative process has been implemented as an optimization loop in the open-source code *Effective Quadratures*. When the set of correlation coefficients for Y are calculated, it is possible to decompose ρ' via Cholesky decomposition:

$$\rho' = L_0 L_0^T \tag{2.23}$$

The matrix L_0 performs the mapping of the correlated samples Y to a new space where the transformed samples U are independent and vice-versa according to the following equations:

$$U = L_0^{-1} Y \tag{2.24}$$

$$Y = L_0 U \tag{2.25}$$

Once the set of independent samples are available it is possible to build in their space the polynomial chaos expansion and sample the points inside the correlated, original set of data (Figure 2.4).

2.2.2 Adjoint

The design of complex system such as HPT blades is challenging and involves numerous variables, from geometrical parameters to working conditions. The computational cost (along with its time) can represent a limit for an extensive performance analysis: a Monte Carlo approach is, most of the times, not feasible when the number of the variables involved is too large; in industry an additional limitation is represented by the project deadlines. Surrogate models such as PCE can represent a first important tool for the designer, but it is still affected by the course of dimensionality. Among the solution adopted to overcome this problem, the adjoint method has recently gained particular attention [3].

The adjoint solver can be continuous or discrete. In the former, the variations of the target function are combined with the variations of field equations, both with respect to the uncertain input variables (they are geometrical parameters and flow field variables); this can be achieved by using Lagrangian multipliers. The adjoint equations are derived from the model equation and then discretized in order to obtain the solution; in the discrete approach the adjoint equations are obtained after the discretization of the model equation. The computational cost of this mathematical operator is independent by the number of input parameters. The adjoint can therefore provide the gradients of one objective function with only one run. There exists, although, a computational cost related to the choice of a continuous or a discrete solver: the two methods can provide the same results in terms of gradients [76] but the computational cost of deriving the discrete adjoint is larger. Despite this aspect, the discrete adjoint is widely implemented [16, 40] thanks to the availability of automatic differentiation algorithms [124, 107, 28].

In the present work, the discrete approach implemented in HYDRA [63] solver was used. The aerodynamic performance I of a generic body immersed in a fluid is dependent on the design variables α_j describing the body shape and the flow properties U inside the fluid domain (Equation 2.26).

$$I = f(\alpha, U) \tag{2.26}$$

The variation of the objective function with respect to the shape variations, expressed trough the design variables α_i can be written via first order derivatives as in the following Equation:

$$\frac{dI}{d\alpha_j} = \frac{\partial I}{\partial U_k}\frac{\partial U_k}{\partial \alpha_j} + \frac{\partial I}{\partial \alpha_j} \tag{2.27}$$

The adjoint solver is related to the solution of a normal CFD (primal) in the way that it uses the converged solution of this latter. This aspect leads to the assumption that the numerical errors contained inside the primal flow solution are minimized thus the convergence of the CFD simulation is good enough to minimize the presence of noise in the adjoint solution. Mathematically this can be written as in equation 2.28:

$$R(U,\alpha) \approx 0 \rightarrow \frac{dR}{d\alpha_j} = \frac{\partial R}{\partial U_k}\frac{dU_k}{d\alpha} + \frac{\partial R}{\partial \alpha_j} \approx 0 \tag{2.28}$$

Assuming a negligible value of residual for the primal convergence, the term R can be assimilated to a null value, leading to the definition of the adjoint variables v_i, as in Equations 2.29.

$$-\left(\frac{\partial R}{\partial U}\right)^{-1}\frac{\partial R}{\partial \alpha} = \frac{dU}{d\alpha} = v_i^T \tag{2.29}$$

By including the adjoint variables in Equation 2.27, the total derivative, so the sensitivity, of the objective I with respect to the design parameter α_i can be written as:

$$\frac{dI}{d\alpha_i} = v^T\frac{\partial R}{\partial \alpha_i} + \frac{\partial I}{\partial \alpha_i} \tag{2.30}$$

Thus, the adjoint equation can be written as reported in 2.31: as already anticipated, the adjoint solver computational cost does not depend on the number of the variables α but on the objective functions of the study.

$$\left(\frac{\partial R}{\partial U}\right)^T v = \left(\frac{\partial I}{\partial U}\right)^T \tag{2.31}$$

Chapter 3

Uncertainty Quantification

3.1 Real Test Case

3.1.1 GOM Scans

In industrial practice, it is important to record information about the manufactured components. In the case of turbine blades, after each phase of the production chain, an optical measurement is performed using the *GOM* optical 3D metrology methodology [2]. Each piece is illuminated with white light; the surface surrounding the blade is divided into small sub-spaces and each of these is compared in terms of distance with a reference point; it follows a translation to 3D Cartesian coordinates and a further *triangularization* of the cloud of points. The final digital file is in *STL* (stereolithography) format and it represents the digital version of the real mechanical component. The computational power available permits the designers to analyze the digital twins and perform wide investigations: in a manufacturing context, it is important to ensure the manufacturing deviations do not interfere with the normal phases of the production process.

The blades are subject to continuous monitoring phases during their lifespan: it is common practice to perform periodic sanity and integrity checks [60].

Used components, once dismounted from the engine, can still be useful to unveil defects in the original design as well as critical conditions which can lead to a deterioration of this component's lifespan - being this, the main context which triggered this project's investigation.

Thanks to Rolls-Royce Bristol team, a set of 200 scanned rotor blades were analyzed. The set of real blades belongs to a high-pressure stage of the same engine design; the name of the real engine will be omitted in the present work. For the sake of clarity, it will be renamed *RReng* from this point on.

All the GOM scans report (Figure 3.1):

- The external surface of each blade
- The lower end wall of the blade

- The firtree: the mechanical connection between the blade and the disk.

Each blade belonging to the set is characterized by (Figure 3.1):

- Shroudless tip
- Winglet with a cooling system
- Gutter with cooling holes and weldings
- Squared Trailing Edge (TE) in the tip region.
- Cooling holes on both pressure side (PS) and suction side (PS)

The working conditions of the engine design intent can be compared with old military engines [61]: it is assumed an average probability of removal rate equal to 1/1000 Engine Flying Hours (EFH): for every 1000 hours, one engine will be dismounted to replace a damaged component. The first scheduled maintenance of an engine can be thought to be in the middle of this time window: the amount of EFH before the first Scheduled Maintenance Hours will be renamed in this work with the acronym SMH and represents the first reference to classify the damage level of each blade.

Three out of four engines are inside the expected time window for part removal, i.e, between 2 and 3 SMH. One of them - engine 1 - worked with components whose lifespan has been shortened by half of the expected value. The remaining 3 engines were dismounted and are inside the normal time window for component removal. A classification of the geometrical deviation and damage is necessary to understand how the performance has been affected by this lifespan issue.

The GOM scans (*STL* files) are a digital representation of the external surface: the information about the chemical composition, oxidation, chemical corrosion, and other internal features of the blade cannot be captured in these STL files.

3.1.2 Damage Classification

A total number of 200 real (HPT) rotors were analyzed in this work; they belong to the same engine design and can be gathered in four main groups: Engine 1 worked for 1.5 SMH while Engines 2, 3 and 4 between 2.5 SMH and 3 SMH. All blades have been dismounted and scanned. Each component is digitalized: we refer to each digital twin with the term *GOM scan.* Each blade, so its digital reproduction is characterized by geometrical deviations in two main zones of interest, namely the blade pressure side (PS) and suction side (SS) between the 0% and 70% of the span (zone 1 in Figure 3.1) and the tip region (zone 2). In Figure 3.1 a typical example of damage in an old HP unshrouded turbine blade is shown.

The first visual Figure assessment of the 200 blades leads to the damage classification summarized in scheme 3.2. Both PS and SS of the GOMs are characterized

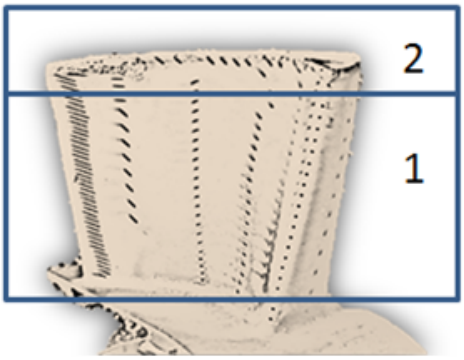

Figure 3.1: Classification of GOMs zones of interest in a typical HP unshrouded turbine rotor

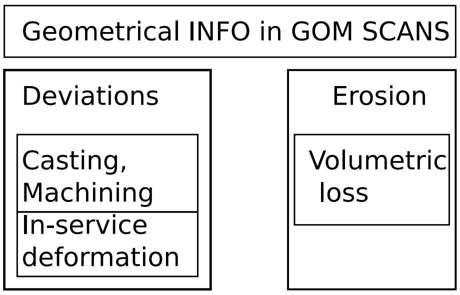

Figure 3.2: Classification of the geometrical information contained in each GOM scan

by small geometrical deviations (GD) derived from manufacturing tolerances and in-service deformations. The available data does not include these GD associated with each blade right after the manufacturing process. This means that in the present work we are not able to distinguish and isolate the effect of the manufacturing process and in-service plastic deformations. These two contributions are classified together under the term **geometrical deviations (GD)**.

Another important information contained in the GOM scans is the erosion: a large volumetric loss in the tip region is visible along the trailing edge on both pressure and suction sides.

More details about the parametrization of the GD and erosion are reported in a dedicated section of this work.

3.1.3 Real Blades After In-service Period vs Design Intent

Every manufactured engine has an original *Design Intent*. This section explains the concept of *Intent* and its link with the available data discussed in the previous section.

The long design process ends with a final shape for each component inside the engine. The aerothermal study carried out by the engineers starts from the assumption of a target performance (namely, the efficiency at each stage, multi-stage efficiency, capacity, reaction, thermal load, etc...). The **design intent** of a high-pressure stage blade must account for the blade's *cold to hot transition*. *Cold* configuration refers to a dismounted (removed from the engine) or mounted blade whose engine is not in operation (shutdown). The *hot* configuration refers to a blade inside an in-service operating engine. Normally, the aerothermal designers have experimental data from test rigs and are aware of the displacement characteristics of a *cold* to *hot* transition.

The **cold design intent**, is herein considered as the unique reference geometry for all 200 *GOM scans*. It has a shroudless tip to minimize losses, and a squared trailing edge due to limitations in the manufacturing procedure [126].

Each *GOM scan* is conceptually a *cold geometry* since it has been dismounted from its *RReng* high pressure stage. The difference between this *cold* configuration and the *Intent* is that the first has been manufactured, mounted inside an HPT Stage, and operated inside a real engine for a certain amount of hours. It experienced the *cold-to-hot transition* and deteriorated due to erosion and corrosion and deformed because of in-service extreme operational conditions. Each scanned blade provides engineers with valuable information regarding major and minor issues of the original DI once it is operated and subjected to real operational severe conditions.

The machines used to scan the components usually scan four blades at the time. One of the pairs is upside down with respect to the other two; the STL file resulting from the scan process will report for each point, belonging to the outer surface of the blade, a set of coordinates in the Cartesian system expressed with respect to a target point. The length unit of the GOM is in millimeters. On the other hand, the design intent, even if expressed in the Cartesian Coordinate system, is not supposed to have the same spatial position and scale of the GOM scans. A scaling process together with an **alignment** is necessary to compare the shapes and start a performance analysis: to this aim, an automated routine in Polyworks [2] was used. Section 3.1.4 details this process.

3.1.4 Alignment

To align each GOM scan with respect to the unique cold DI, it is assumed that the firtree was not exposed directly to the high temperatures during in-service operating conditions. Therefore the shape deviation in these zones is expected to be negligible.

The Polyworks algorithm compares the cloud of points belonging to each GOM scan with the DI blade's surface. Four reference points are set over the firtree for each cloud of points describing a single blade (Figure 3.3a). The software then rotates and translates each GOM so that the distance between each reference point and the analog set on the DI is minimized.

The final output of the process is a new rotated and translated GOM scan in the Cartesian space. The overlap of each GOM towards a unique reference location

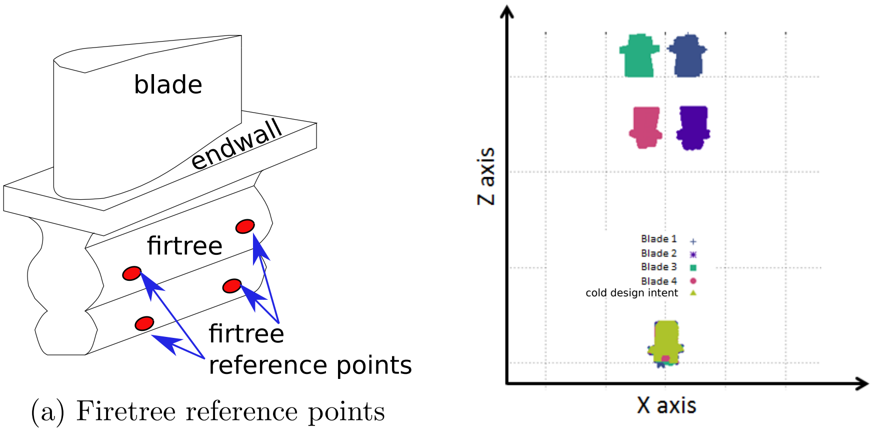

(a) Firetree reference points

(b) GOM scans position

Figure 3.3: Firtree alignment via Polyworks routine: reference points

enables to run a statistical analysis. In the present work, the following step is represented by the quantification of GD and erosion on the tip.

A representative GOM is shown in Figure 3.4: a small deviation between the CAD and the aligned GOM is visible. The colourmap depicts the distance between the GOM and the cold DI, measured along the orthogonal direction with respect to the GOM surface; the distance field is plotted over the GOM. The tip of the blade is not visible; the SS, due to the presence of numerous cooling holes, is reported using a low-resolution image. The proportions in the geometries illustrates, as in the rest of the work, were scaled in order to do not export confidential data.

Some representative GOMs among the 200 aligned have been sliced along two planes: the first cuts the surface at 10% of the span while the second cuts it at 50%. The comparison with the cold DI, sliced at the same positions, is reported in Figure 3.5. The aligned blades have a small deviation with respect to the DI's shape: a general lean is visible but the positions of the leading edge along with the trailing edge were not significantly affected by the mixed manufacturing and in-service deviations. Further investigation and quantification are still needed to better understand the impact of these deviations on the overall performance of the blade.

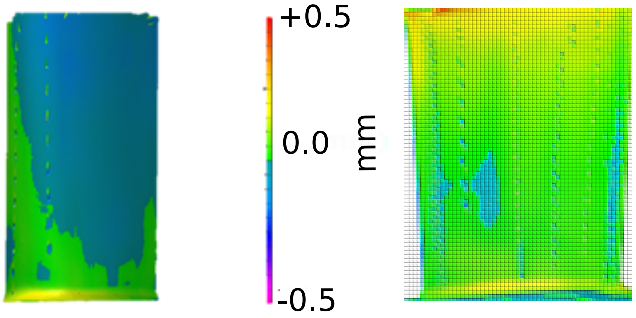

(a) Suction Side

(b) Pressure Side

Figure 3.4: GOM after the alignment performed via PolyWorks routine: the normal distance between the reference DI and the GOM surface is plotted over the surface of the latter. The winglet of the blade is not visible

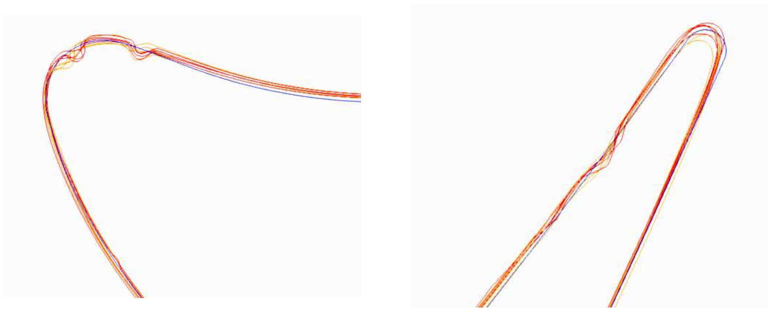

(a) 0.1 LE

(b) 0.1 TE

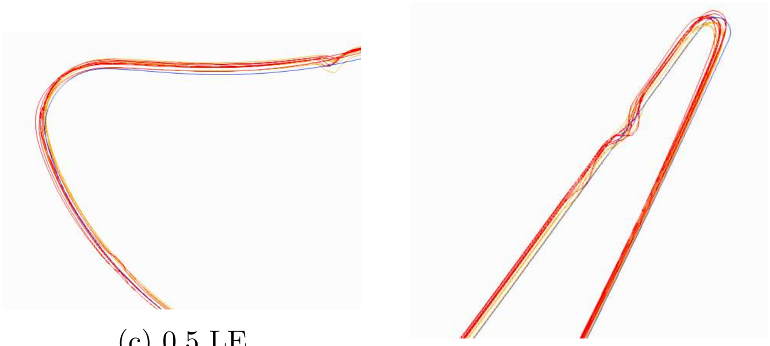

(c) 0.5 LE

(d) 0.5 TE

Figure 3.5: Sections of aligned GOMs vs section of reference cold CAD

3.2 Engineering Parameters

So far, the geometrical deviations observed in the GOM scans were presented in a qualitative way. To carry out a performance assessment, it is necessary to identify the relative movement of each GOM scan with respect to the DI (*identification*) and parametrize these key movements.

3.2.1 Identification and Parametrization

The present work uses the PADRAM [71] design space to parametrize the shape of each blade and create a mesh to assess performance via Computational Fluid Dynamics (CFD) simulations. PADRAM is an in-house software specifically designed for rapid and parametrized deformation, design and multi-block structured meshing of jet engine components. The latest available version is 20.1 at the time of writing. Among all the available parameters, a subset of ten is selected. The list below presents a short description and it refers to Figures 3.6a, 3.6b and 3.6c. Each parameter is applied along five radial sections from 0% to 70% of the blade's span (0, 10, 30, 50, 70).

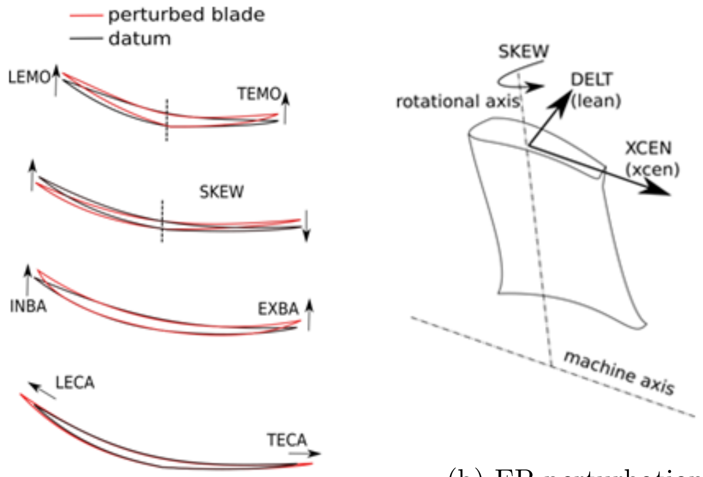

(a) EP section perturbation

(b) EP perturbation

(c) Hicks-Henne Bumps

Figure 3.6: Graphical representation of the selected PADRAM design parameters and their action in a blade profile

- XCEN: axial translation of the blade section. The reference direction is parallel to the machine rotational axis. A positive value of XCEN represents a translation of the blade section towards the inlet section of the stage; a negative value shifts the section towards the exit section of the stage. This translation is measured in mm.

- DELT: tangential shift of the blade section (in degrees). The tangential direction is orthogonal with respect to the engine's radius and its rotational axis. A positive value of DELT shifts the blade section towards the pressure side while a negative one in the opposite direction. Each radial section is rotated around the engine's axis.

- SKEW: solid rotation (in degrees) of all blade's sections around a vertical axis passing through the blade at a specified point. The vertical axis is parallel to the engine's radial direction.
- LEMO: Abbreviation of Leading Edge MOvement (degrees). It is a localized quadratic perturbation. The thickness of the blade changes consequently. LEMO units are expressed in degrees; it is possible to specify the position of blending points along the blade section, from where the perturbation will be null.
- TEMO: Abbreviation of Trailing Edge MOvement. Analogous to LEMO.
- INBA: Abbreviation of INlet Blade Angle (in degrees). The thickness of the blade is preserved.
- EXBA: Abbreviation of EXit Blade Angle (in degrees).
- LECA: Abbreviation of Leading Edge Camber Angle (in degrees). The blade chord varies according to the applied perturbation.
- TECA: Abbreviation of Trailing Edge Camber Angle (in degrees). It is analogous to LECA.

To better reproduce the particular blade shape of the GOM scans, localized Hicks-Henne bumps along the surface have been added to the parametrization. The Engineering Parameters (EP) listed above exhaustively describe the blade shape by perturbing it along five radial sections; the localized perturbation performed by Hicks-Henne bumps needs more sections to better capture the small irregularities of each GOM's surface.

Therefore, nine equally distributed radial sections, ranging from 0% to the 70% of the blade span were selected. Each of these sections contains four Hicks-Henne bumps (two for PS and two for SS). For each bump, the variables listed below are controlled.

- Width
- Amplitude
- Position of the centre with respect to the blade's chord length.

The selected parametrization is robust enough to partially deform the blade however, it is not enough to describe the severe volume loss characterizing the tip region. This matter is further discussed in Section 3.3.

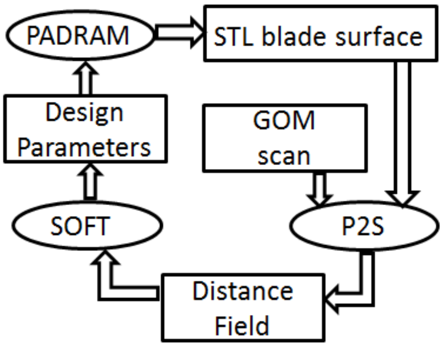

Figure 3.7: Inverse Mapping Optimization loop: softwares and outputs involved

3.2.2 Inverse Mapping

Each GOM scan was aligned in the Cartesian space so that the firtee was fixed; the next step is the construction of PADRAM geometry twins and their meshes (used in Section 4.3.2 for the performance assessment).

To pass from an aligned GOM to a parametrized twin, an inverse mapping procedure [104] was used (Figure 3.7). This is an optimization cycle where the values of the selected PADRAM design parameters are optimized. The objective is to minimize the average distance field between each GOM and the DI's surface, deformed using the given values of the PADRAM parameter.

Three softwares are involved in this optimization cycle:

- PADRAM: receives a vector of parameters (EPs) and returns the surface of the blade obtained by deforming the DI with them;
- P2S: is an in-house Rolls-Royce code; among other capabilities, it calculates the distance field between two similar clouds of points. The algorithm is based on the comparison between a reference cloud of points (GOM scan in the present study) and a target surface (PADRAM blade surface);
- SOFT: in-house optimization software.

The optimization strategy is performed using MAM (Multipoint Approximation Method) and SQP (Sequential Quadratic Programming) for the optimization of the EPs while SQP is used for Hicks-Henne bumps.

The inverse mapping is run for all 200 GOMs. In Figure 3.8, results of one representative blade are reported: the initial distance field between the GOM scan and the PADRAM surface shows the difference between the expected shape and the real blade. The pressure side has a positive lean. A noticeable lean is present along the blade hub as well. After the optimization cycle, the distance field is near zero along the blade surface.

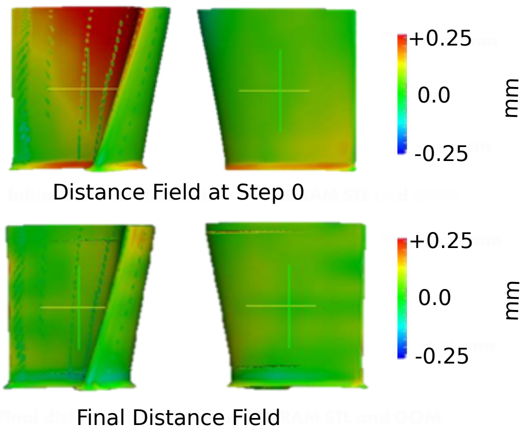

Figure 3.8: Inverse mapping results on one representative blade

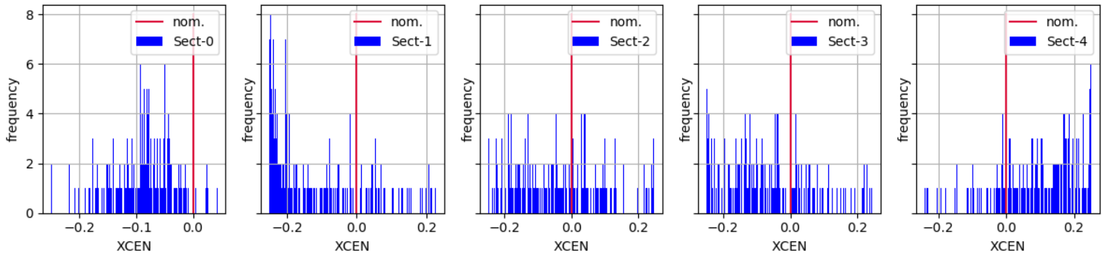

Figure 3.9: XCEN statistical trend for all 200 analyzed blades

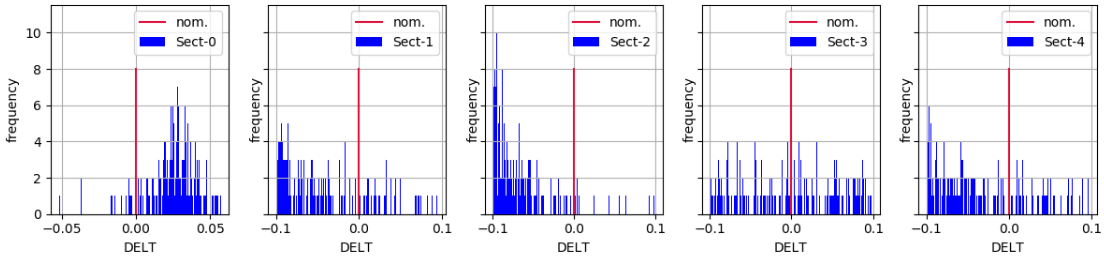

Figure 3.10: DELT statistical trend for the 200 analysed blades

The next step consists in comparing the perturbation vectors for each PADRAM twin with the values associated with the nominal cold geometry. The 200 blades provide a global statistical behavior of the geometrical deviations. Figures 3.9 to 3.17 report a red line passing through the null value - representing the nominal value associated with each parameter, together with the histograms for all parameters

Only five parameters were found to have a noticeable variation concerning nominal values: XCEN, DELT, LEMO, TEMO, and SKEW. These are the parameters to be used for the rest of this work.

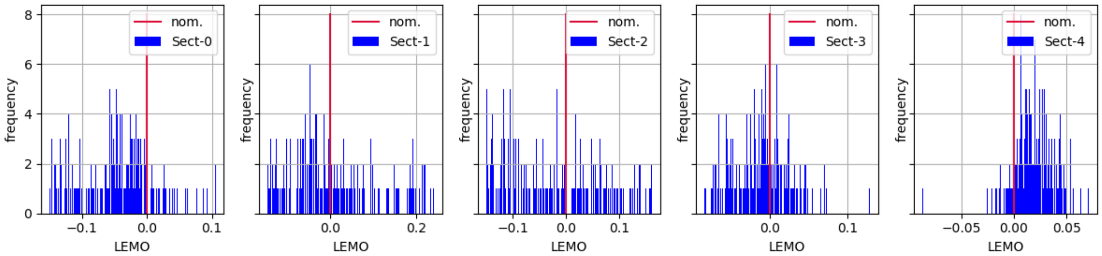

Figure 3.11: LEMO's statistical trend

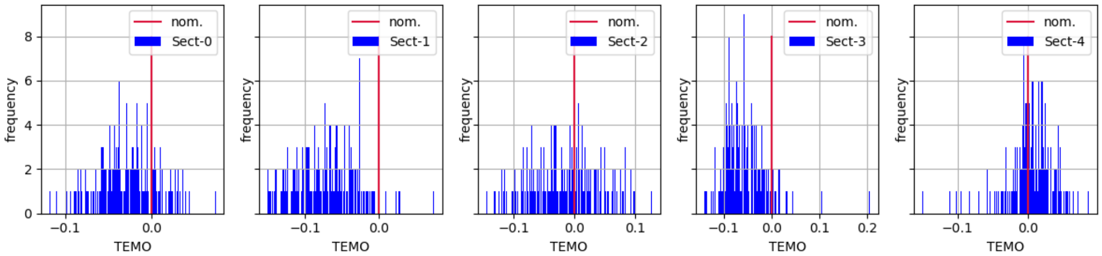

Figure 3.12: TEMO's statistical trend

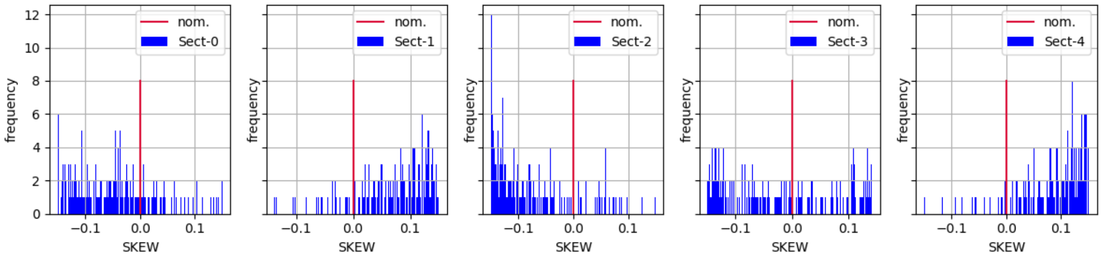

Figure 3.13: SKEW's statistical trend

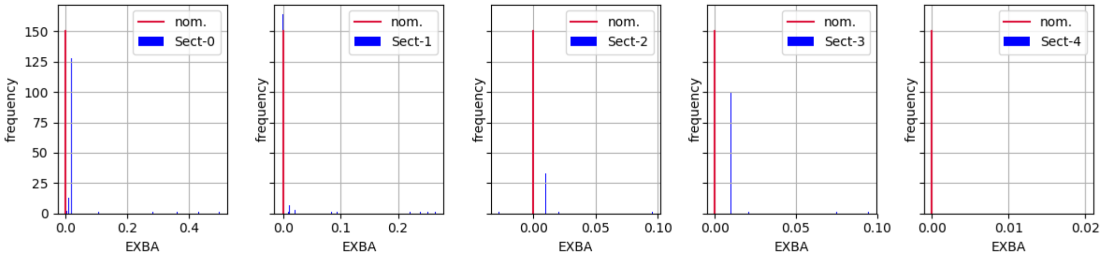

Figure 3.14: EXBA's statistical trend

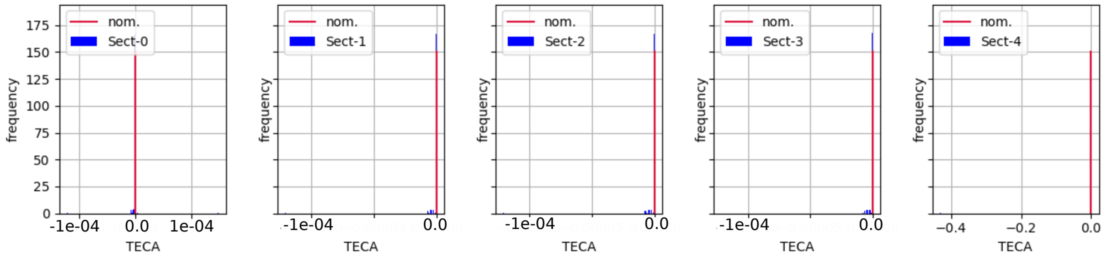

Figure 3.15: TECA's statistical trend

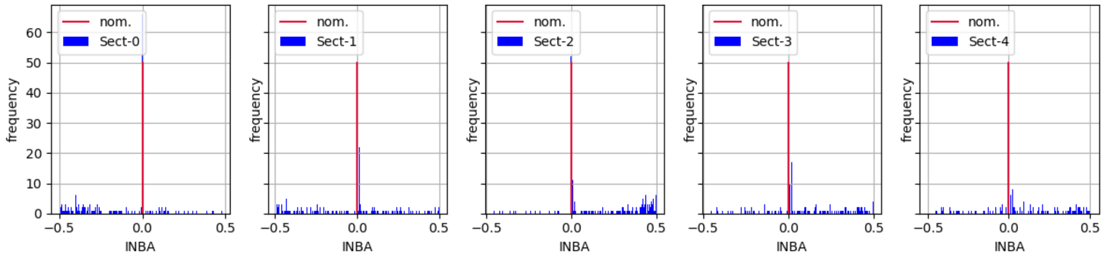

Figure 3.16: INBA's statistical trend

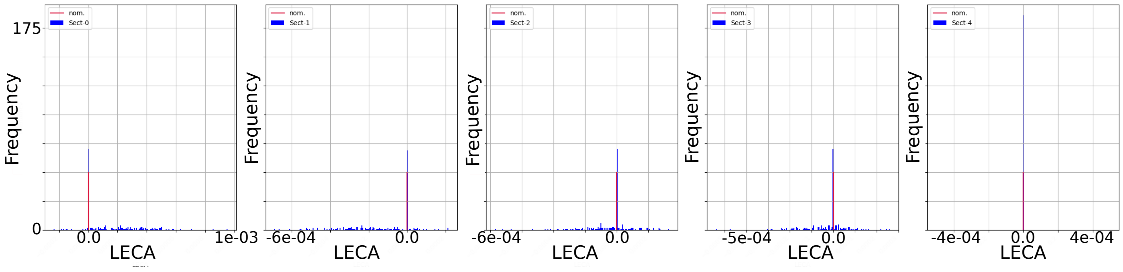

Figure 3.17: LECA statistical trend

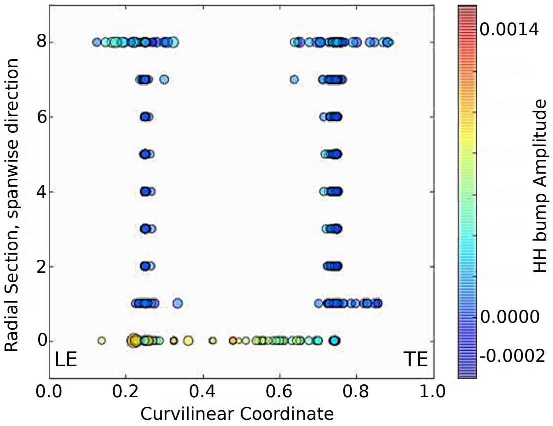

(a) PS

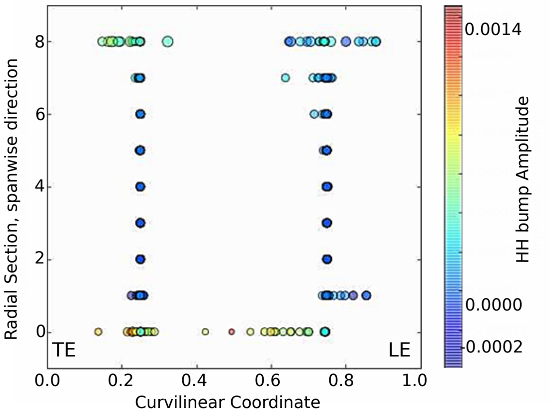

(b) SS

Figure 3.18: Hicks-Henne bumps statistics: width, amplitude and position with respect to the curvilinear coordinate

The values for the Hicks-Henne bumps variables are shown in Figure 3.18. Both magnitude and width variation of the bumps are small. The position is more uncertain along the sections close to the hub and the 70% mark. From the previous visual inspection of the blade's surface, no volume removal was noticed between 0% and 70% mark; the GOM's cooling holes positions are instead compatible with the Hicks-Henne positions. For the rest of this work, the Hicks-Henne bumps will be not included in the PADRAM uncertain design space, because they are not representative of a blade's shape variation. These bumps are a better fit to represent the presence of a cooling row which is not the focus of this work.

3.2.3 Variables' Independence Analysis

A further assessment is needed to understand the relationship between the EP uncertainties. The selected strategy for the Uncertainty Propagation is the PCE, and, as already mentioned in Section 2.2.1, it requires the assumption of independence between input variables to be true, otherwise a preliminary preprocessing is necessary (mapping via Nataf transform or orthogonalization via Gram Schmidt are available in Effective Quadratures suite). The quantification of the correlation between the EP uncertainties is carried out by calculating the Pearson coefficient, which formulation is expressed in Equation 3.1.

$$r_{EP_1EP_2} = \frac{cov(EP_1, EP_2)}{\sigma_{EP_1} \cdot \sigma_{EP_2}} \tag{3.1}$$

The coefficient $r_{EP_1EP_2}$ represents a linear relationship between two sets of design parameters EP_1 and EP_2: for the case under study the correlation matrix R_{EP} has dimensions 25×25; its graphical representation reported in Figure 3.19 shows a mild correlation between the uncertainties of the EPs. A classical PCE construction can therefore be carried out for the uncertainty propagation.

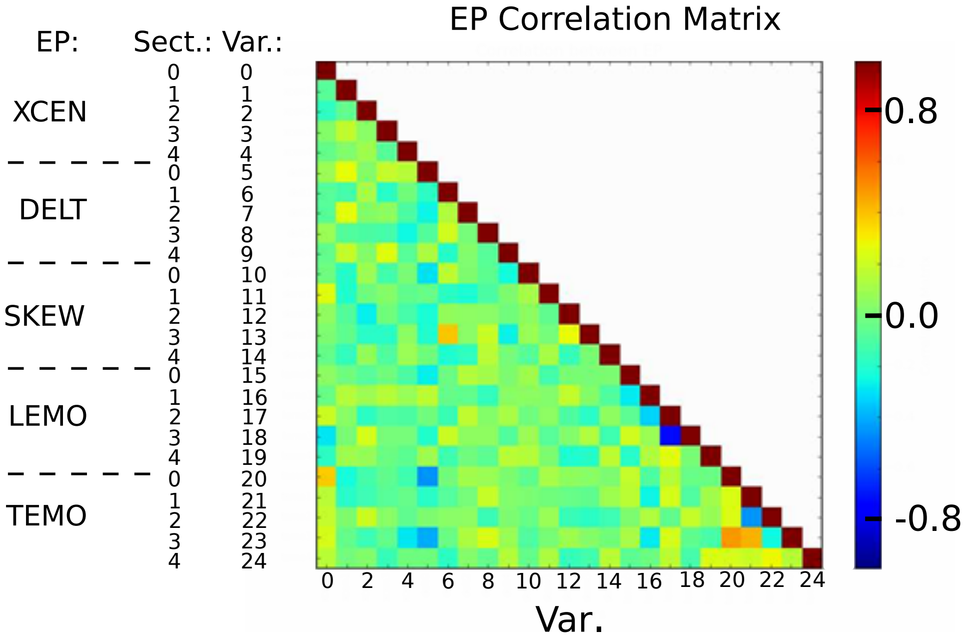

Figure 3.19: Correlation matrix of PADRAM's EP

3.3 Erosion

3.3.1 Visual Inspection of the GOMs Tip Region

The DI of the unshrouded blades under exam is characterized by a tip design that is meant to minimize the over tip leakage [124]. Figure 3.20 reports a section of the tip design in different axial planes, together with typical geometry for a scanned blade. The presence of a gutter on the trailing edge and rim on both PS and SS is meant to trap the flow passing between the tip region and the casing, avoiding the passage of the gas from pressure to suction side and re-directing it with the same exit angle of the main flow. The eroded blades are all characterized by the loss of this important aerodynamic feature; GOM scans and the cold reference blade have been sliced along three radial planes (Figure 3.21) cutting the rim along planes passing through 10% (TE1), 50% (TE2) and 90% (TE3) of the rim height.

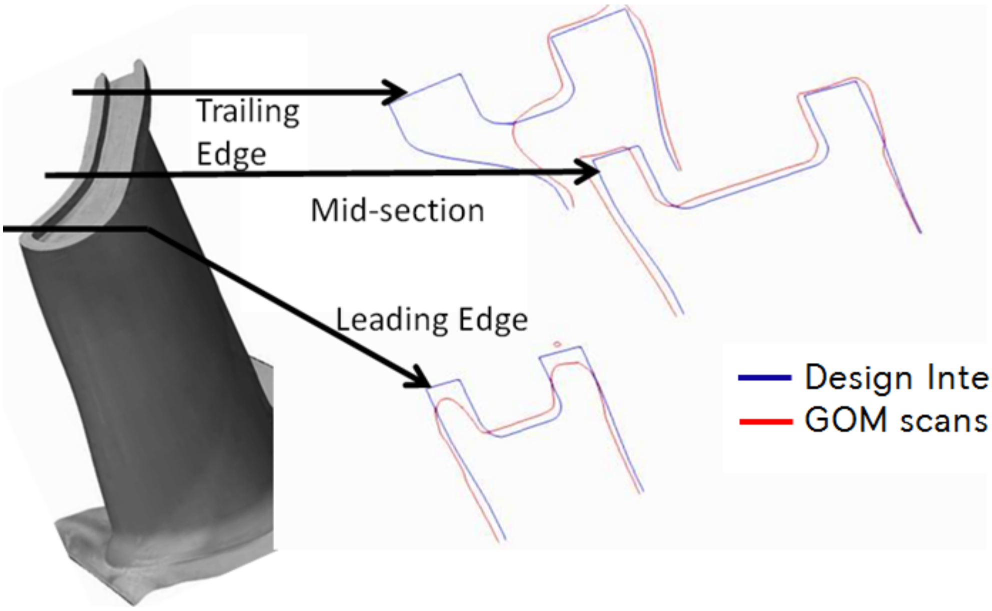

Figure 3.20: Overtip mechanism

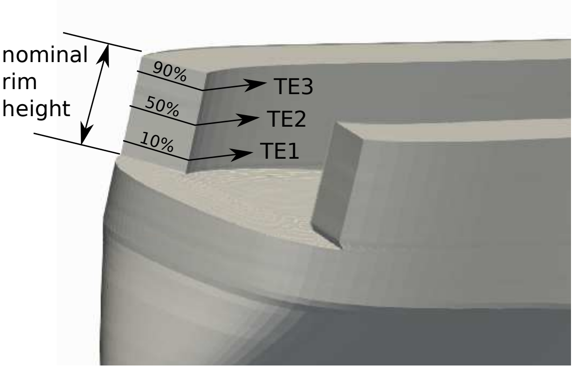

Figure 3.21: Rim cut positions: TE1, TE2, TE3

A graphical comparison of the rim's volume loss is reported in Figures 3.23,3.22 for the blade subset 1.5 SMH and 3 SMH. A large volumetric loss along the trailing edge pressure side (Figure 3.22) is already present in the blades which worked for 1.5 SMH: it means that the beneficial over tip mechanism is already lost and a drop in performance is expected. The trailing edge rim in blades which worked for more hours is totally removed. A graphical comparison made along the same radial sections of the rim is proposed for the leading edge (Figure 3.23). In the leading edge area, the rim is totally eroded along the 90% of the height both for 1.5 SMH and 3 SMH. The set of blades associated to 1.5 SMH have a more uncertain erosion level at the 50% mark of the rim's height: a subset of blades shows a localized leading edge loss while another subset was able to preserve the metal from local melting.

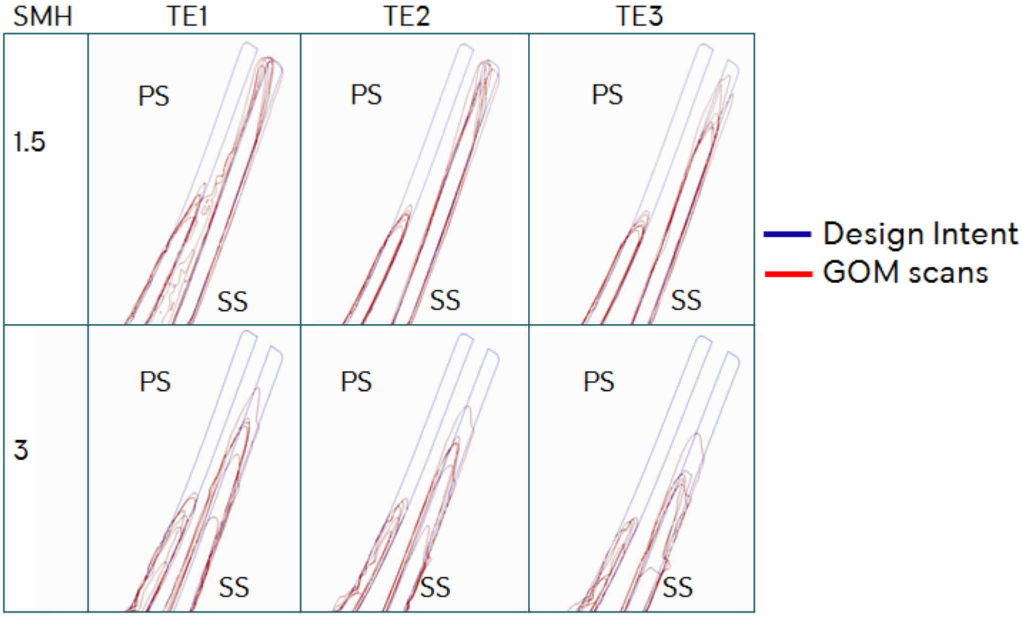

Figure 3.22: Trailing Edge erosion along three radial planes cutting the rim at different heights

The next step is the quantification of the erosion level along the GOM's rim. To this aim, a set of Python in-house scripts have been written. The blade rim was divided into several regions with a length of 0.01c, and the mean distance from the nominal rim position of the GOM points falling within the given region was calculated. The results obtained showed that most of the blades had lost 100% of rim height near the TE, and presented a common length for the LE rim removal, but not for its depth. After repeating the calculation for all the GOM scans, the statistical behaviour in the three zones was calculated, and it is reported in Figure 3.24 in the form of histograms. The average rim removal in the TE region is 21% on the PS and 17% on the SS, both measured as a percentage of the axial chord. The LE region is characterized by an average loss of 80% of rim height.

3.3.2 Identification and Parametrization

The information regarding the aforementioned localized volume loss was summarized using 3 variables, as shown in Figure 3.25. The PADRAM Variable Squealer Cut

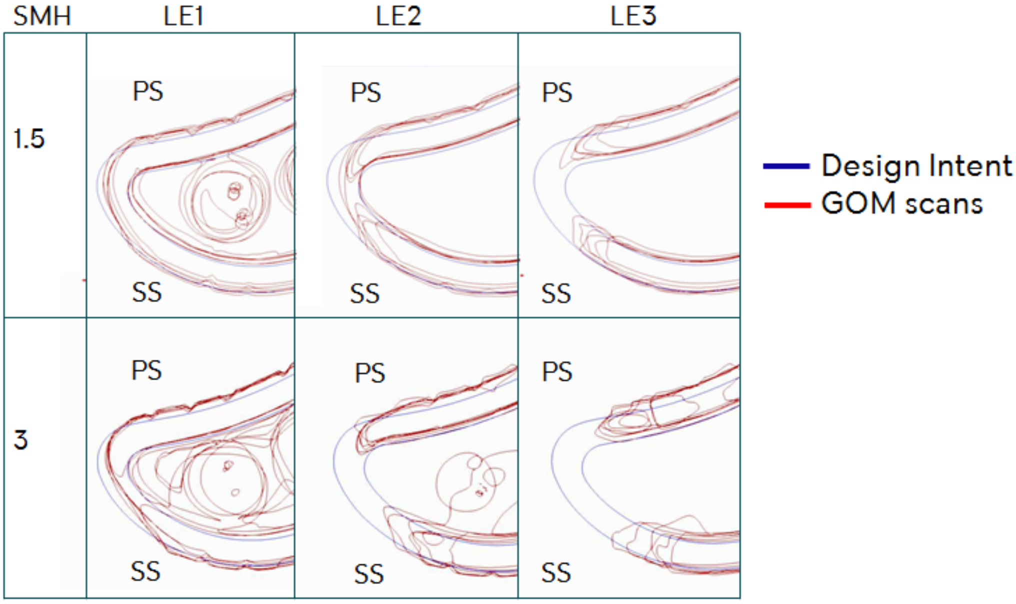

Figure 3.23: Leading Edge erosion along three radial planes cutting the rim at different heights

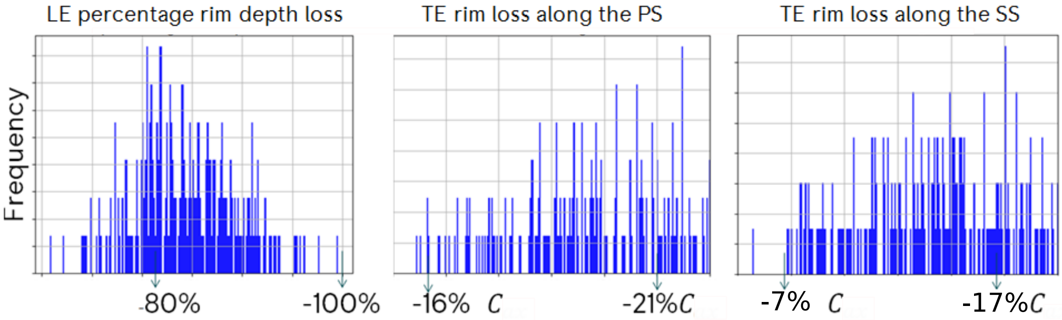

Figure 3.24: Statistical trend of erosion along three regions of interest

option was used to model the rim cuts according to the erosion parametrization in Figure 3.25). This option allows to specify the starting and the ending points of the rim's cut, expressed as a percentage of the blade's chord; furthermore it is possible to define the rim's height reduction.

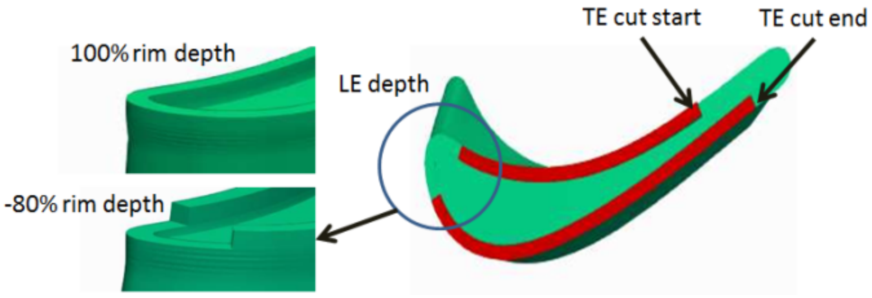

Figure 3.25: PADRAM Squealer Tip Cut option: for the case under study the TE start and end points are selected along with LE's depth

Chapter 4

Uncertainty Propagation

4.1 Cold and Hot Configurations

During the in-service conditions, the HPT blades are exposed to high centrifugal and thermal loads. These loads are responsible for the deformation of the blade's shape, both elastic and plastic. The former is present only during operation, and is reversed once these loads are removed; the latter remains even after the loads cease to be applied and can be captured together with the initial deviations due to manufacturing, metal erosion and pitting, in the cold shape of the component. A direct measurement of these deformations during operation represents a challenge because it is hard to replicate the complexity of the working conditions or perform measurements in such a harsh environment. Experimental setups in laboratories and numerical models are used to quantify the aforementioned expansion; with the term "*cold*" we refer to the blade's shape when it is not mounted on the rotor's disk or inside the engine when it is switched off. The term "*hot*" refers to the blade's shape inside an operating engine. Given these definitions, the classification and quantification of all uncertain variables seen in the previous chapter can be considered as an investigation on a set of cold blades. The performance assessment of an HPT rotor is usually conducted by simulating in-service conditions thus including the expansion of the blade. In the present work, the translation from cold-to-hot condition is represented by a localized translation applied to the blade's shape. The array containing the cold-to-hot translation for the case under study has been provided by the RR engineers and can be applied to the cold baseline configuration. The investigation carried out in Section 3.2 produced a statistical description of the geometrical deviations characterizing the 200 cold HPT blades. The following step is to understand how the performance metrics are affected by the uncertainties during the in-service period; high fidelity CFD runs were used for this purpose. The assumption made in each simulation is that the perturbation field characterizing the shape deviation of the GOM scans (EP and erosion) can be linearly added to the transformation field describing the cold-to-hot translation (conceptual sketch in

Figure 4.1).

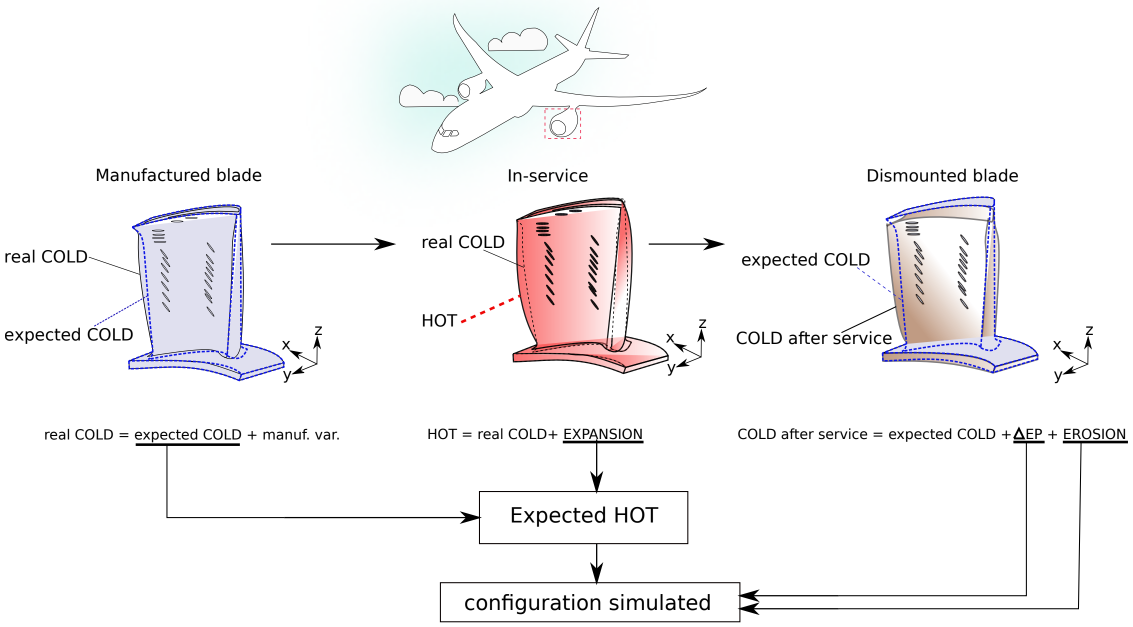

Figure 4.1: Cold-to-hot translation

4.2 CFD and Mesh Setup

4.2.1 PADRAM Mesh

A spatial discretization was performed using PADRAM [71] (PARametric Design and Rapid Meshing). As already seen in Section 3.2.2, this software contains an embedded library of a blade's geometrical parameters: by varying these values and applying them onto a baseline geometry, it is possible to easily deform an existing geometry. PADRAM also allows the rapid and parametrized generation of block-structured meshes over the aforementioned geometry.

The modelling of a single passage is based on *H-O-H* mesh; referring to the sketch in Figure 4.2, the blocks upstream of LE ($A1, A2, A3$), downstream of the TE ($B1, B2, B3$) and next to the periodic boundaries (C, D) were external H meshes; the topology of the layer surrounding the blade is *O-mesh*. The tip gap, as well as the internal part of the gutter, were discretized via H topology. The number of nodes along the edges orthogonal to the blade's surface, along the circumferential and the spanwise directions were varied in order to control the total number of cells. The mesh construction for the winglet was performed using the dedicated PADRAM option *Squealer Tip* [19]; the trailing edge of the blade's design is characterized by a

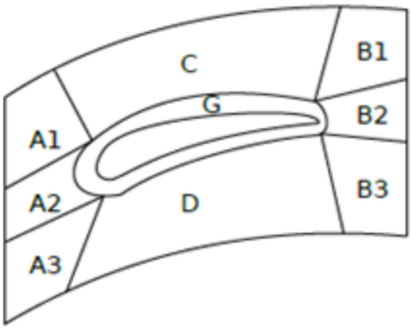

Figure 4.2: PADRAM mesh blocking on a blade-to-blade surface around the blade's tip

squared shape and a rim cut: the parametrization of this part is discussed in Section 3.3.2. Details of the mesh are illustrated in Figure 4.3.

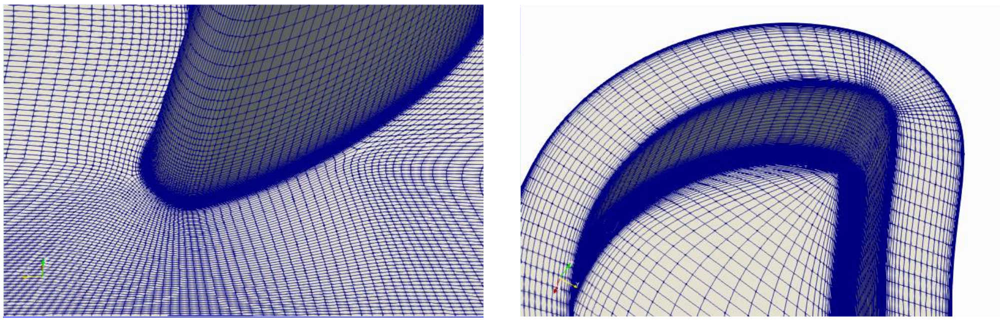

(a) LE hub

(b) LE tip

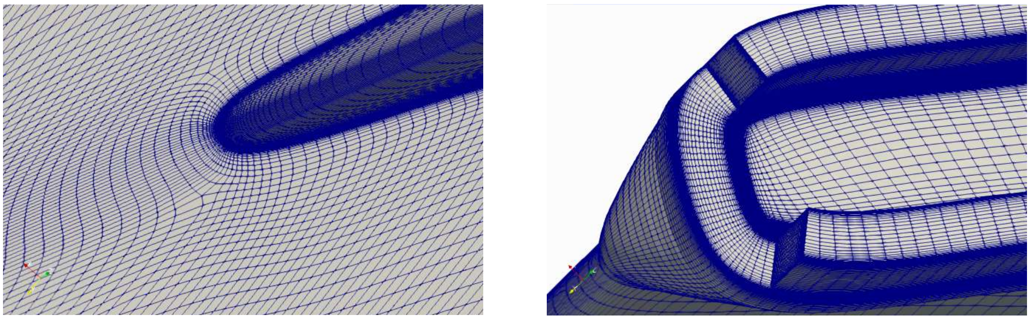

(c) TE hub

(d) TE tip

Figure 4.3: PADRAM mesh details: LE and TE visualization at hub and blade tip

4.2.2 CFD Setup

The solution of the 3D steady-state Reynolds-averaged Navier-Stokes (RANS) equations was performed using Hydra [63]: this CFD solver has been thought of as a

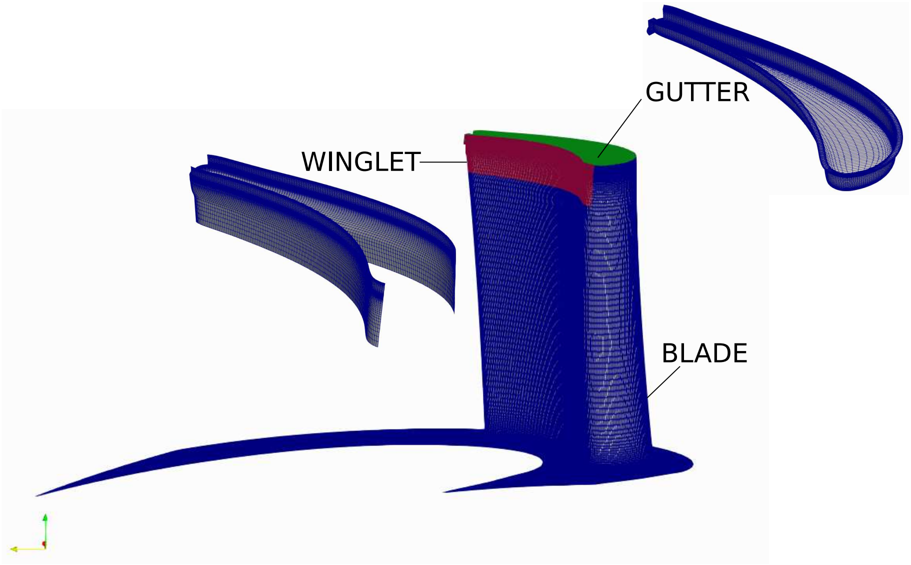

Figure 4.4: Details of blade, winglet and gutter meshing

sequence of multiple softwares (peculiarity which inspired the name, recalling the monster from the ancient Greek mythology). A first module (*jm52*) prepares the files containing the boundary conditions, a second module (*jm70*) initializes the flux and the last (*jm51*) runs the CFD simulation. We will refer to HYDRA as the set of these three modules together in the rest of the work. The fluid domain surrounding the blade has an elongated shape, following the direction of the wake (Figure 4.5); periodic boundary conditions were set along the periodic surfaces of the domain. The external blade surface along with the lower platform and the upper case were set as adiabatic walls.

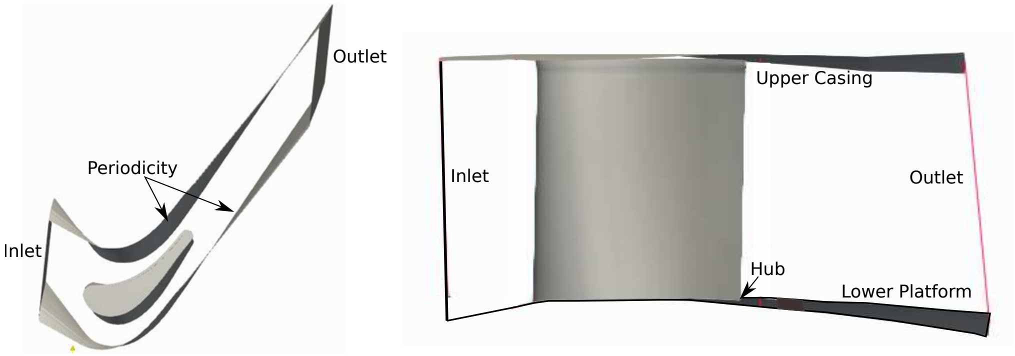

Figure 4.5: Fluid domain shape adopted in the present study

The boundary conditions for the fluid domain include: profiles of total temperature and pressure along the inlet section and profile of static pressure along the outlet section. Inlet profiles of total temperature and pressure are reported in Figure 4.6. The static pressure distribution along the outlet section of the rotor is reported in Figure 4.7. For the simulation of the HPT rotor, the turbulence model Spalart-Allmaras was selected [111], the scheme is implicit with a CFL (Courant-Friedrichs-Lewy) value equal to 40. The values of Y^+ were kept below 1. The operating fluid was set as compressible air with viscosity and thermal capacity defined as functions of the local temperature. The domain was simulated as a moving reference frame with fixed rotational speed, and the blade and hub were set as stationary in the rotating frame, while the casing was considered stationary in the absolute frame. The film cooling is not included in this study, nor secondary mass flows from the cavities usually present upstream the leading edge in real engines. The convergence criterion is set to a Root Mean Square (RMS) of the residuals (mass, energy and momentum) equal to $1e-16$; furthermore, a maximum number of iterations is specified: as reported in the following sections, for the case under study is unlikely to reach a convergence below $1e-16$ and when this limit was reached (Section 4.3.1) it was made possible only by a simplification of the geometry in the tip region.

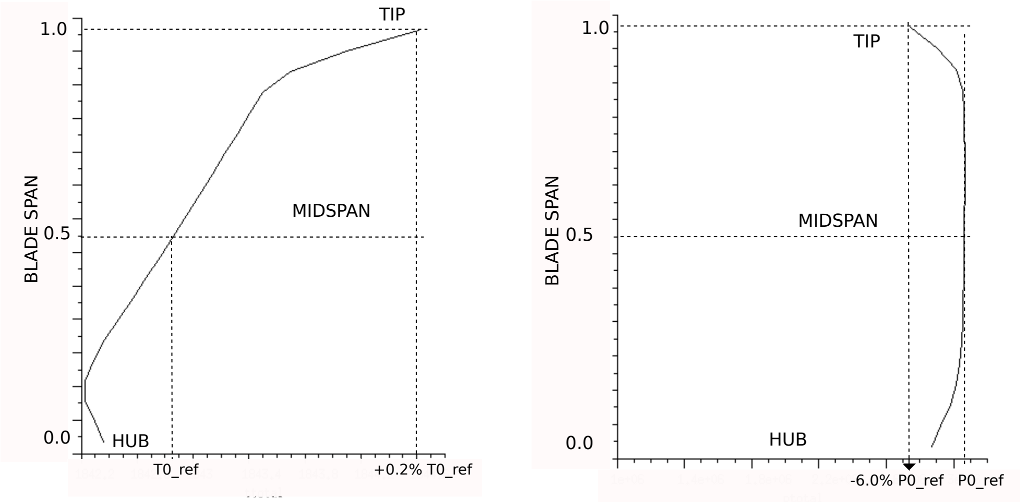

(a) Total temperature

(b) Total pressure

Figure 4.6: Simplified boundary conditions used in the present study: rotor inlet section

A very fine mesh was first constructed; from this setup, in order to create the coarser meshes, the number of nodes along circumferential, radial, and orthogonal with respect to the blade's surface, were scaled by a factor fc. A total number of four meshes were tested and compared in terms of the final value of rotor efficiency: in table 4.1 all values obtained are reported. The values are expressed as the difference between the coarser meshes and the reference (the finer mesh). The mesh with $9.9M$ cells was selected for the analysis carried out in the next sections. Figure 4.8 illustrates in detail the convergence of the tested meshes in terms of Root Mean Square (RMS) of the residuals (mass, energy and momentum) while Figure 4.9

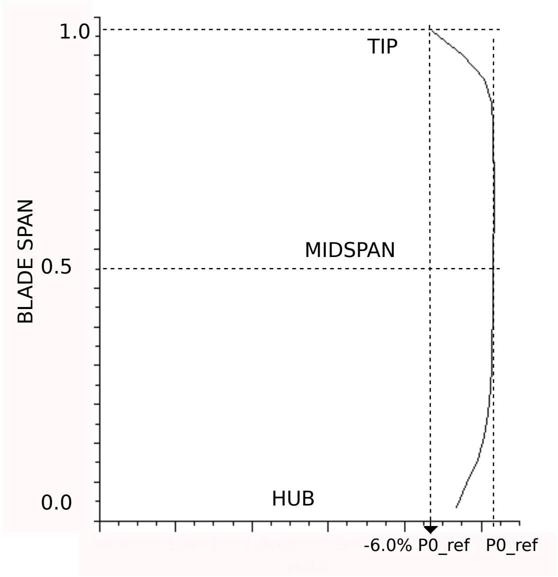

Figure 4.7: Simplified boundary conditions used in the present study: static pressure at rotor outlet

shows the rotor efficiency η_{rotor}. This latter is non-dimensionalized with respect to the reference value of η_{rotor} associated with the finer mesh.

Mesh number	Scaling factor	Number of cells (Millions)	$\eta_{finer} - \eta_{rotor}$
0 (finer)	1.0	14.40	-
1	1.1	11.56	-0.0009
2	1.15	9.93	-0.0014%
3 (coarser)	1.2	7.52	0.13%

Table 4.1: Mesh independence study: number of cells in each mesh and comparison of efficiency estimations

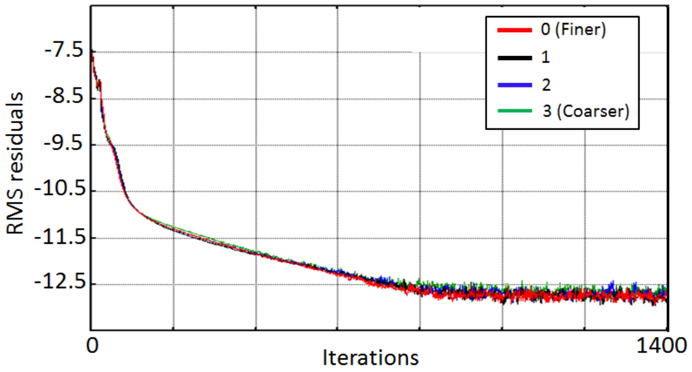

Figure 4.8: Convergence in terms of RMS of residuals for the mesh independence study

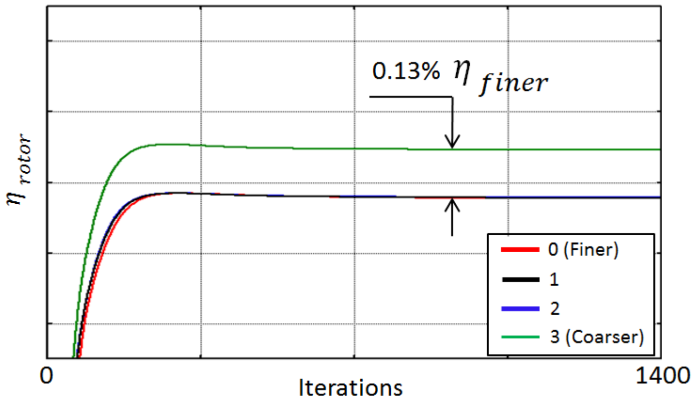

Figure 4.9: Convergence in terms of rotor efficiency for the mesh independence study

4.3 Engineering Parameters

4.3.1 Adjoint Simulations

The HYDRA software suite includes a discrete adjoint solver that allows the calculation of the first-order derivative for a number of figures of merit relative to a wide range of geometrical parameters. The intrinsic cost of an adjoint simulation is roughly equal to that of 3 primal CFD runs for each figure of merit. For the case under study, a linear relationship between EPs and the selected figure of merit (rotor efficiency) can be justified given the small statistical deviations measured in the UQ campaign in Section 4.3.2. The HYDRA adjoint solver requirements and limitations are observed below:

- Primal solution

  The term *primal* refers to a run of a standard CFD simulation. The discrete adjoint solver reads the primal flow file and uses the latter to solve the adjoint equations (described in Section 2.2.2) and calculates the gradients of the objective function. In order to minimize the numerical errors during the HYDRA adjoint run [63], it is strongly recommended to reach an RMS of residuals value of $1e - 14$ for the primal convergence.

- Turbulence model limitations The only fully supported turbulence model at the time of writing is the *Spalart-Allmaras*. The k-ω Shear Stress Transport (SST) is available but a frozen turbulence option must be selected. In the present work, the Spalart-Allmaras model is used.

- Geometry limitations

  Several tests for the application of the adjoint solver have been performed in the present study: an important consideration regarding the reliability of the adjoint gradients must be done to understand the heuristics behind the numerical strategies of this work. A first test was run with the entire (baseline) geometry, i.e. the datum configuration complete with both gutter and winglet. Even though the primal's convergence can be acceptable in terms of residuals (RMS), the validation of the adjoint gradients against a finite difference analysis did not show satisfactory results The finite difference analysis was performed: for each of the 5 EPs (DELT, LEMO, TEMO, XCEN, and SKEW) was applied one per time and one radial section per time (0%, 10%, 30%, 50$ and 70% of the span) with a step equal to ±0.1 degrees for all the parameters but XCEN whose step is set to $0.1mm$. The derivative of the objective function was calculated via central finite difference with a step equal to 0.1.

  A second test was run, this time without gutter and winglet (simplified geometry) and keeping the same tip gap as in the reference geometry. This time, along with a good primal convergence, the calculated adjoint gradients were matching, within a satisfactory tolerance for all the parameters but TEMO, the derivatives calculated via finite difference analysis on the same, simplified geometry (Figure 4.11). To drive an optimization process, it is important to have reliable values of adjoint gradients and the simplified geometry can provide satisfactory results. So for the rest of this work, more specifically in Chapter 5, the adjoint will be used with the simplified geometry. In Figure 4.10, a distorted image of the simplified geometry along with its reference geometry is reported.

The comparison of the adjoint gradients with finite differences for all selected variables indicates the ones with a larger influence towards the variation of the metric of interest (rotor efficiency in this study). Figure 4.11 illustrates the adjoint gradients validation; the sensitivity with respect to a variation of TEMO is overestimated by the adjoint gradients. The trailing edge movement influences the throat area which

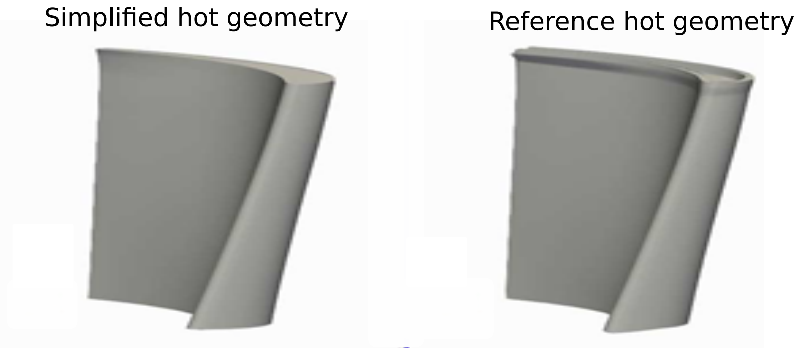

Figure 4.10: Simplified rotor, gutter and winglet are removed from the reference hot configuration

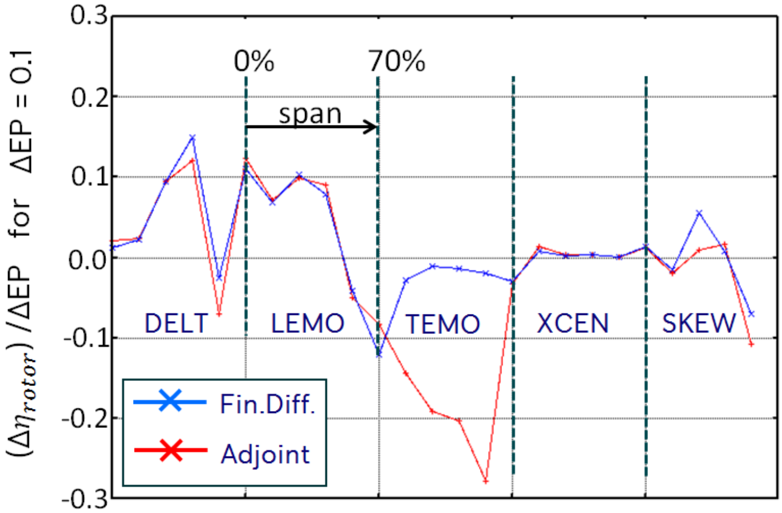

Figure 4.11: Adjoint gradients validation. Comparison between derivatives values and finite difference analysis carried out on a simplified geometry

in turn does not have a linear relationship with the performance variations: the linearization performed by the adjoint is not enough to capture this effect. Among the EP gradients showing a good agreement with the finite difference analysis, DELT and LEMO seem to have a higher influence towards a variation of rotor efficiency. For this reason, these two parameters are selected in the following sections to perform the UP via PCE and the optimization process.

4.3.2 Propagation via PCE

In the previous section, the results obtained with the adjoint operator have been discussed along with their validation. The analysis of the impact of each parameter towards the variation in performance led to the selection of DELT and LEMO as the most influencing geometrical parameters for blade sections ranging from 0% to

70% of the span.

The results obtained refer to a simplified geometry. For the sensitivity of the real hot configuration the PCE was selected; the open-source code Effective Quadratures [1, 100] was used to construct the surrogate model. The EPs variations measured during the UQ campaign (see inverse mapping procedure and statistical analysis in Section 3.2) were small with respect to the nominal, expected values. Thus, linearity between the variation of EPs and the change in rotor efficiency was assumed, leading to a first order polynomial expansion. The volumetric loss characterizing the tip region is not taken into account in this phase. For this reason, DELT and LEMO, previously identified as the most influential for the simplified geometry, are the only parameters selected during this sensitivity analysis. The perturbation performed by these two geometrical parameters (DELT and LEMO) were applied on the same radial sections along the span (0%, 10%, 30%, 50% and 70%) seen for the inverse mapping and the adjoint run. Thus the total number of uncertain variables involved in the present UP is equal to 10.

The PCE basis was set as a *total order* and the fitting was performed via a least squared approximation, with an oversampling equal to 1.5. As already reported in Section 3.2.2, the inverse mapping process applied to each GOM led to the identification of a perturbation vector for each geometry. A statistical analysis of the perturbation vectors allowed the construction of histograms for all the EPs, defining the variability of each EP with respect to their nominal values. These histograms (Figures 3.11 to 3.17) were used to define the PDFs as truncated Gaussian as reported in Figure 4.12.

The Uncertainty Quantification was carried out around the hot baseline geometry. A total number of 17 CFD simulations were run: the first configuration has EPs set to zero (baseline) whilst the remaining configurations are calculated by the PCE model, by selecting from the first order quadrature points the ones that maximize the rank of the coefficient matrix. Figure 4.13 illustrates a graphical comparison of the configurations tested and the details about the perturbation vectors applied to obtain each of them are reported in Figure 4.14. The results in terms of statistical moments predicted by the surrogate model are summarized in Table 4.2. The deviation of the mean rotor efficiency η_m from the nominal η_n is reported together with the standard deviation σ. The predicted η_m is slightly smaller than the nominal value and the standard deviation is not significant. These values can be indicative of a design already close to a robust one. This can also be indicative of the fact that a substantial change in performance can be difficult to achieve by using only DELT and LEMO. It is interesting to compare the sensitivity of the full-featured configuration with the one seen in the case of simplified geometry: the gradients were already available due to the adjoint run and the statistical moments were calculated and reported in Table 4.2. The standard deviation associated with the full-featured blade is lower than the one obtained for the simplified geometry.

For each configuration among the 17 simulated, the radial distribution of isentropic efficiency η_{is} was calculated to verify where the difference, even if small,

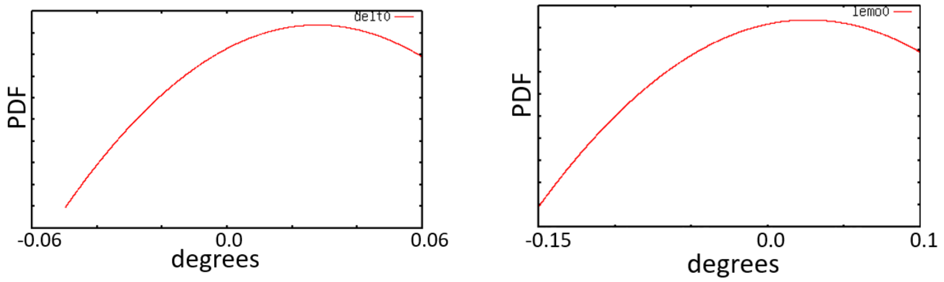

(a) Section 0, DELT

(b) Section 0, LEMO

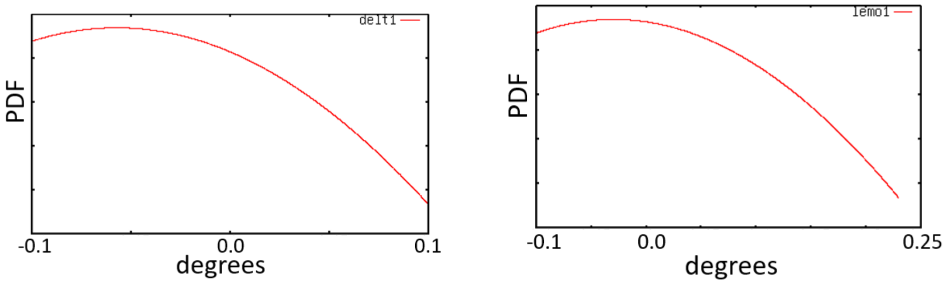

(c) Section 1, DELT

(d) Section 1, LEMO

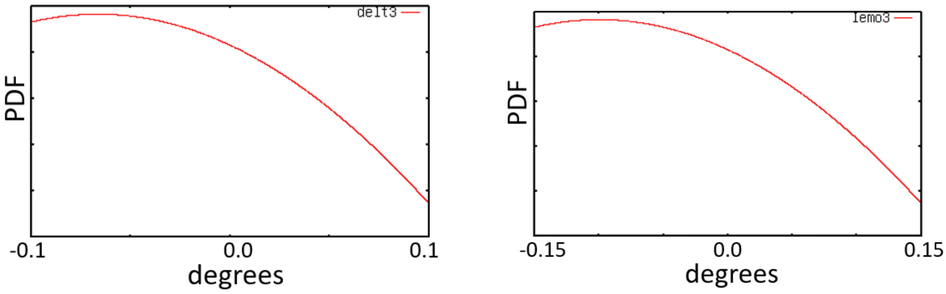

(e) Section 2 DELT

(f) Section 2, LEMO

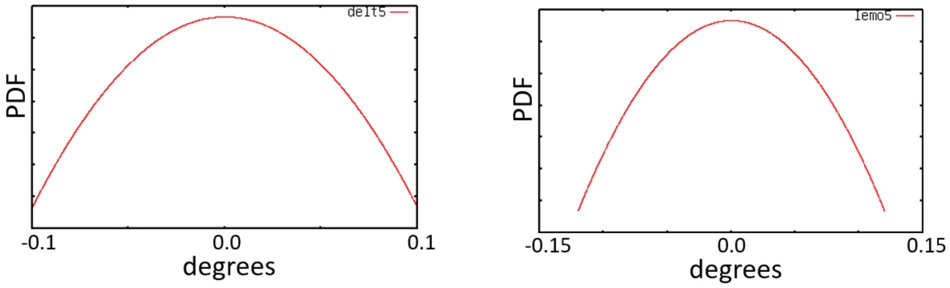

(g) Section 3, DELT

(h) Section 3, LEMO

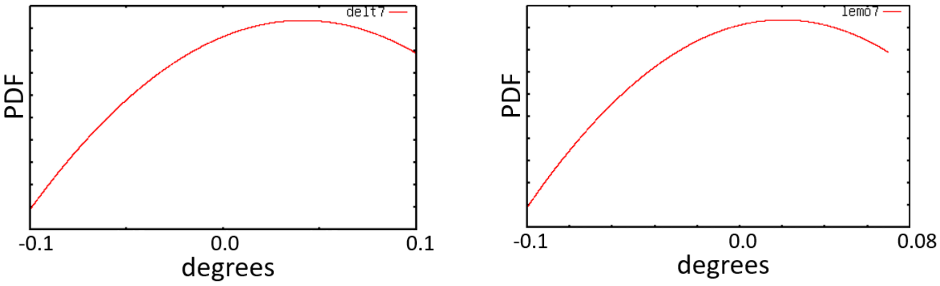

(i) Section 4, DELT

(j) Section 4, LEMO

Figure 4.12: Truncated Gaussian probability distributions associated to statistical variation of EPs in reverse engineered GOM scans

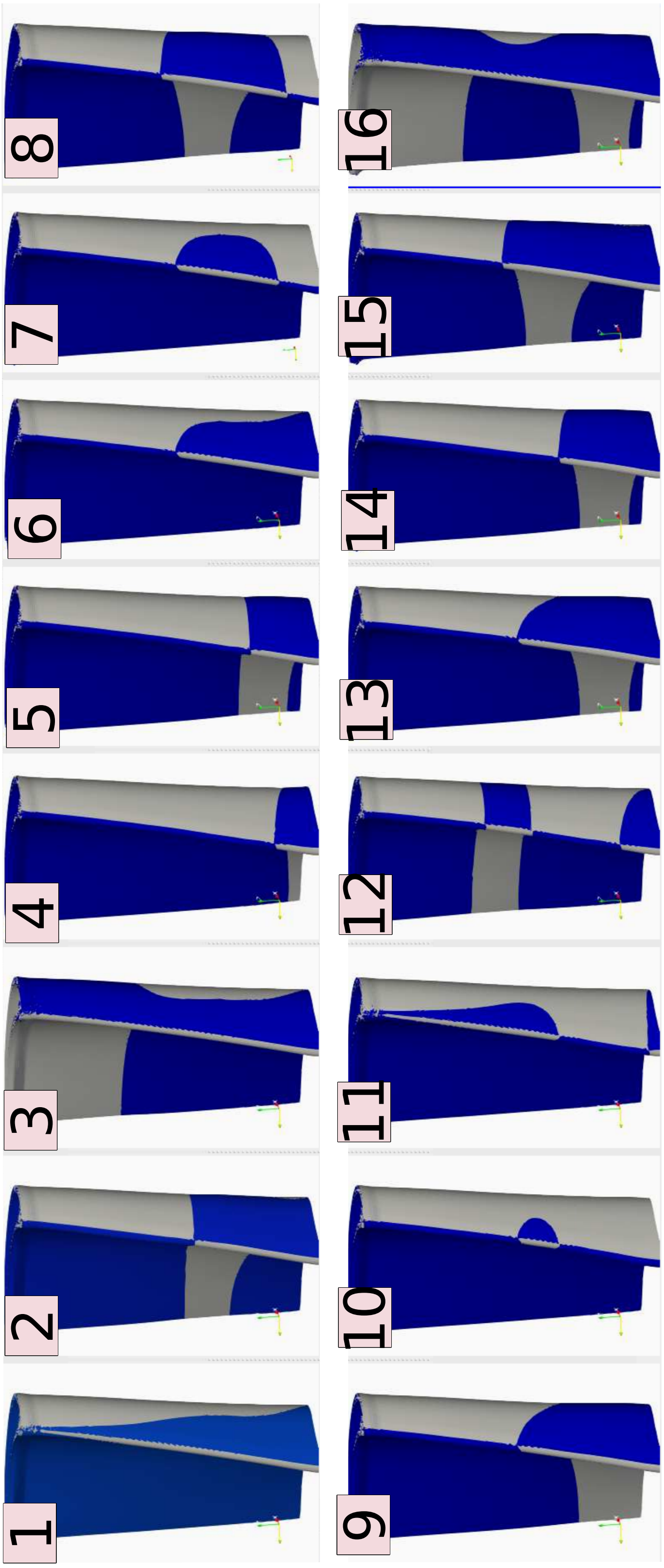

Figure 4.13: Configurations tested during the UP campaign

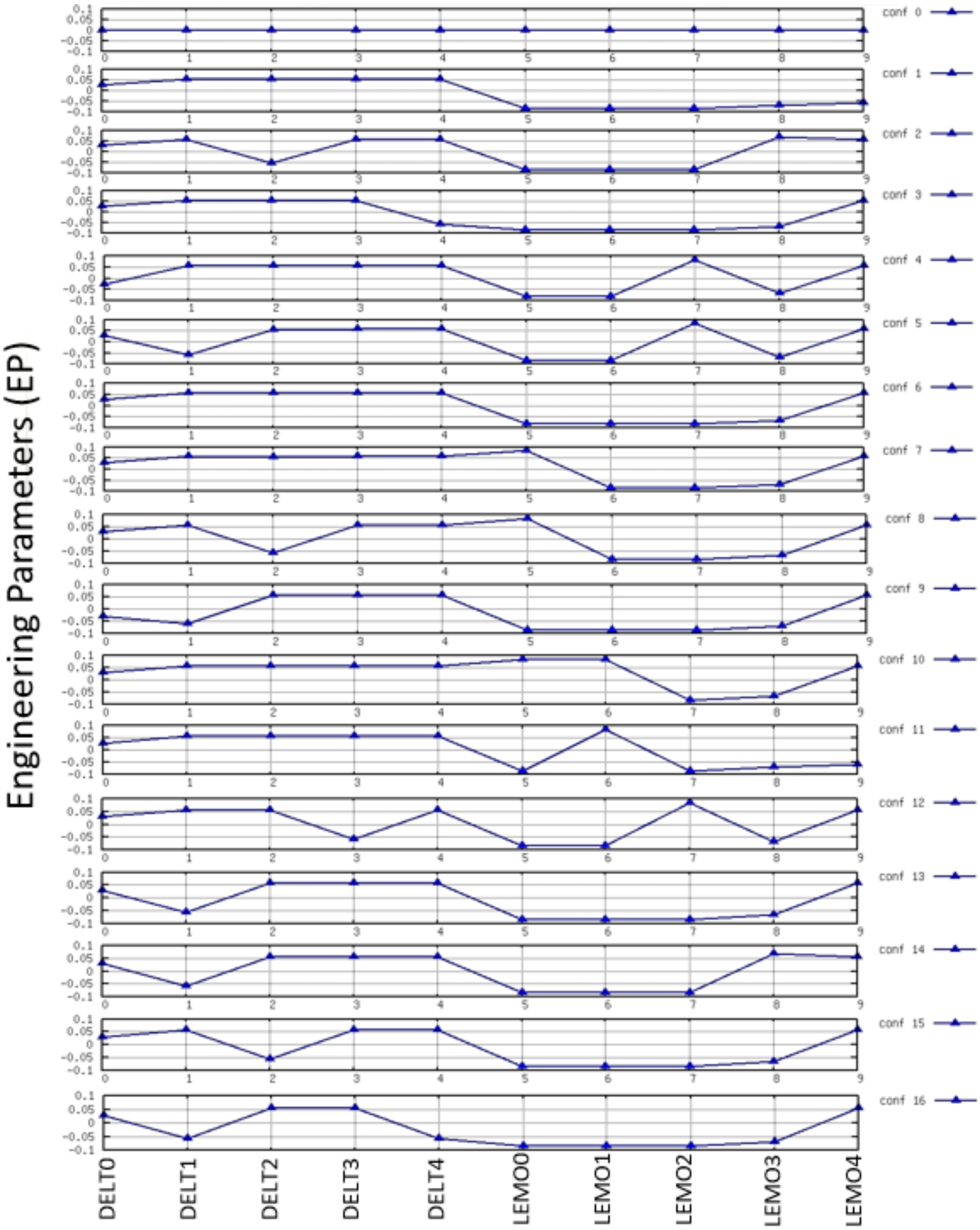

Figure 4.14: Configurations tested during the UP campaign: EP values for each configuration

PCE Prediction	Simplified geometry	Real Geometry
$\eta_m - \eta_n$	-0.0003%	-0.0008%
σ_η	0.0243%	0.0177%

Table 4.2: UP campaign around the hot baseline geometry, PCE predictions compared with the statistical moments calculated for the simplified geometry

between geometries is present. Figure 4.16 illustrates the comparison along with the negligible difference already predicted by the PCE. The calculation was performed by selecting the quantities of interest along the inlet and the outlet sections of the fluid domain; the location of these planes with respect to the blade is shown in Figure 4.15, while in Equation 4.1 the formulation used to calculate the radial distribution of isentropic efficiency is reported. The heat capacity ratio γ is equal to 1.2737. Total temperatures and pressures are the tangentially mass-averaged values at the given radial positions. Small variations in efficiency are experienced among the configurations (Figures 4.17a and 4.17b) near the hub and the tip regions.

$$\eta_{is} = \frac{T_{IN} - T_{OUT}}{T_{IN} - T_{OUT_{is}}} \text{ where } T_{OUT_{is}} = T_{IN} \cdot \left(\frac{P_{OUT}}{P_{IN}}\right)^{\frac{\gamma-1}{\gamma}} \tag{4.1}$$

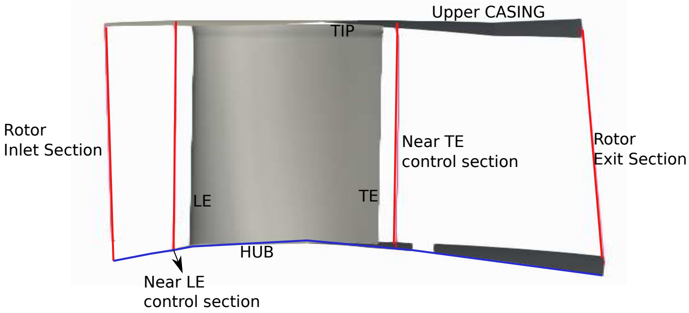

Figure 4.15: Control sections positions for the data reduction performed along the radial direction

4.4 Erosion Parameters

4.4.1 Propagation via PCE

In the previous section, the UP campaign for uncertain EPs showed a small sensitivity of the metric of interest. In this section, a new investigation is carried out to assess the performance variation due to the uncertain erosion parameters.

As already seen in Section 3.3, all the GOM scans analyzed in the present work are affected by volume loss in the tip region where the rim is eroded in a well-defined zone of both leading and trailing edges. The trailing edge is completely removed on

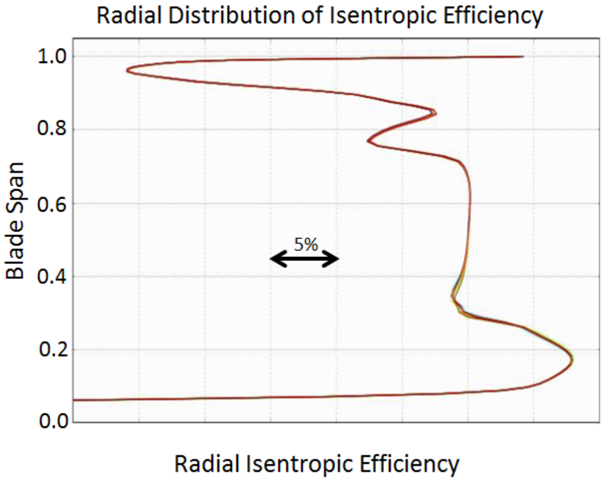

Figure 4.16: Radial distribution of isentropic efficiency for the 17 configurations tested in the UQ campaign, sensitivity with respect to EPs

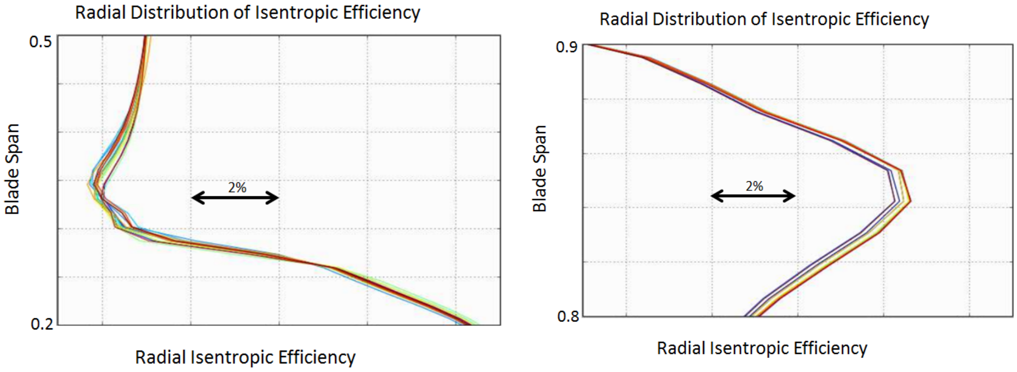

(a) Near Hub

(b) Near tip

Figure 4.17: Radial distribution of isentropic efficiency for the 17 configurations simulated in the UP campaign, hub and tip regions

the pressure side. The original design of the blade winglet was thought to trap the gas flow inside the gutter, such that the overtip leakages would be minimized, and to redirect these gas streams with the same exit angle as the main passage flow.

The sensitivity analysis carried out in this section quantifies the isolated contribution of the erosion along the blade rim; this means that no perturbation was applied to the blade below the tip and the values of all EPs were equal to zero, as in the baseline configuration.

The UP was run by constructing a PCE surrogate model: the numerical setup was the same as the one used for the EPs (first total order polynomial expansion, fit via least square approximation and oversampling equal to 1.5); the PDFs associated to each of the three erosion parameters are truncated Gaussian whose statistical

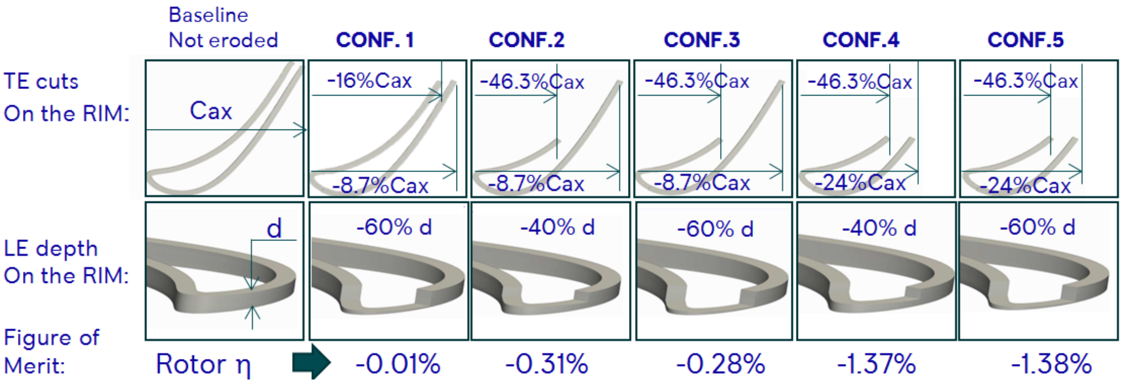

Figure 4.18: Configuration tested in the Uncertainty Quantification of erosion parameters

moments were calculated from the histograms in Figure 3.24 (Section 3.3).

In Figure 4.18, a comparison of all tested configurations is shown; the corresponding values of the uncertainty vectors were selected among the first order quadrature points, to maximize the rank of the associated coefficients' matrix. For each of the six cases, two views are presented: in the first row, the blade is cut along a plane passing through 30% of the rim's height (where 0% is represented by the gutter nominal surface) and orthogonal to the radial direction. The second row illustrates the detail of the rim in the leading edge zone. The removed volume for the three zones of interest is reported in the same way as specified to PADRAM. For the leading edge, the height of the rim volume to be removed needs to be specified (start and end points are fixed), while in the trailing edge region, start and end points need to be specified (the height is fixed to 100% of the nominal rim height).

These six simulated configurations are representative of the statistical behavior within the group of the 200 eroded blades. The predictions of the surrogate model constructed and the details in terms of performance variation, expressed as deviation from the reference rotor efficiency η_n, are reported in Table 4.3. The first difference with the results obtained during the uncertainty quantification for the EPs is the value of the standard deviation σ_η: the set of eroded blades and their PCE suggest a higher sensitivity with respect to the erosion parameters. The average drop in performance, this time, is larger than the one experienced propagating the EP's uncertainties; a maximum difference of -1.48% is associated with the fifth eroded configuration, where the volume loss is more pronounced.

PCE prediction	**Value**
$\eta_m - eta_n$	-0.78%
σ_m	0.68%

Table 4.3: PCE results obtained by performing a UP campaign around the baseline geometry

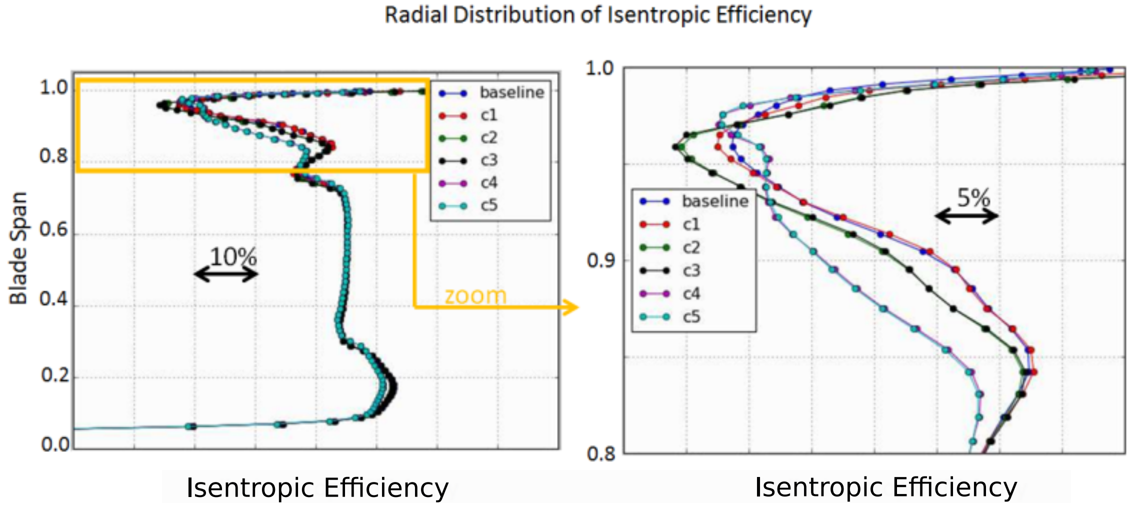

Figure 4.19: Radial distribution of isentropic efficiency for the configuration tested in the erosion parameters UP

Configuration number	**Rotor Efficiency**
0 (baseline)	η
1	-0.01%
2	-0.33%
3	-0.3%
4	-1.47%
5	-1.48%

Table 4.4: Results in terms of rotor efficiency obtained by performing a UP campaign around the eroded baseline geometry

The radial distribution of isentropic efficiency is reported for all the configurations in Figure 4.19. The fourth and the fifth configurations, associated with a more important volume loss along the trailing edge, have lower values of isentropic efficiency around 80% of the blade span. Next to the winglet sections, around 95% of the blade span, a performance recovery is experienced, leading to radially averaged values larger than for the baseline.

The erosion on the tip region leads to a localized tip gap variation with respect to the nominal value. A wider gap between the blade rim and the upper casing allows the gas to pass more easily from the pressure to the suction side; to better understand the OTL (Over Tip Leakage) fluid dynamics, the distributions of non-dimensional relative tangential velocity and non-dimensional entropy are reported respectively in Figures 4.20 and 4.21.

The comparison is shown for the baseline with undamaged rim, the third configuration *CONF3* associated with a drop in performance in-between the nominal and for the worst-case scenario (*CONF5*). The planes where the quantities of in-

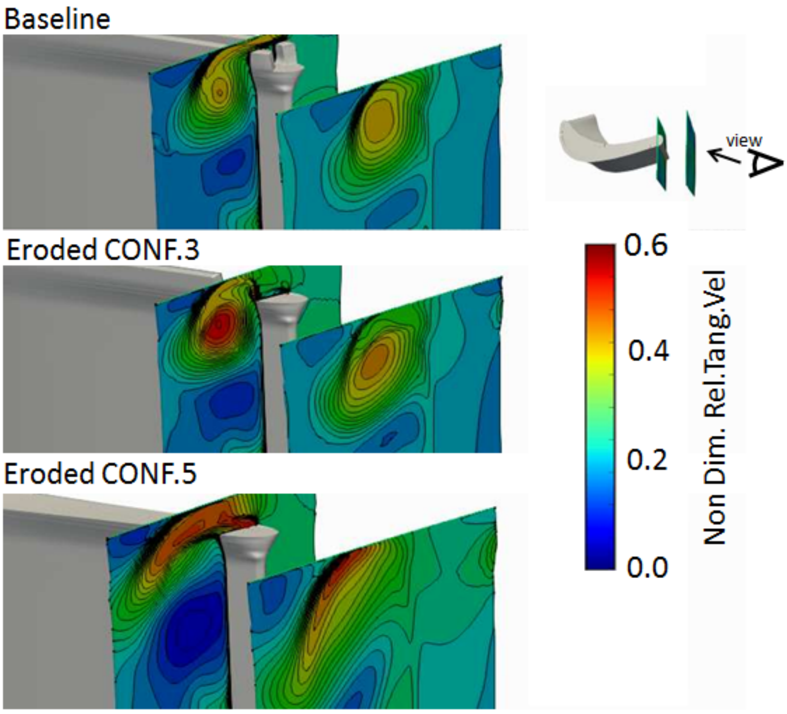

Figure 4.20: Isovalue map of non-dimensional relative tangential velocity on two planes cutting before and after the trailing edge

terest are plotted are located $0.1c$ upstream of the TE, being c the axial chord of the blade; the second plane is $0.5c$ downstream of the TE; the third plane is located $1.5c$ downstream of the TE; the latter control section is visible only in the non-dimensional entropy comparison (4.21), seen with a zoom-out perspective with respect to the plots of non-dimensional relative tangential velocity. Both quantities of interest (qoi) are non dimensionalized according to the formula in Equation 4.2, where *baseline* is the nominal not eroded configuration.

$$qoi = \frac{qoi_{conf_i} - min(qoi_{baseline})}{max(qoi_{baseline}) - (min(qoi_{baseline})} \tag{4.2}$$

The rim along the upper surface of the blade is designed to limit the passage of the gases over the tip but, as soon as the volume loss becomes more important (especially along the trailing edge), the size of the high-velocity jet leaking over the blade increases (Figure 4.20). The entropy generation in Figure 4.21 shows the enlarged tip-leakage vortex and its migration towards lower radial sections. This condition can explain the drop in performance predicted by the CFD simulations.

Figure 4.22 illustrates a 3D view of the over tip flows; three main structures can be identified: the TE vortex, formed by the gases trapped inside the gutter and flowing through the rim at the trailing edge (a); the leading edge horseshoe vortex (b) and the OTL vortex by the gases leaking from the blade's PS to SS (letter c).

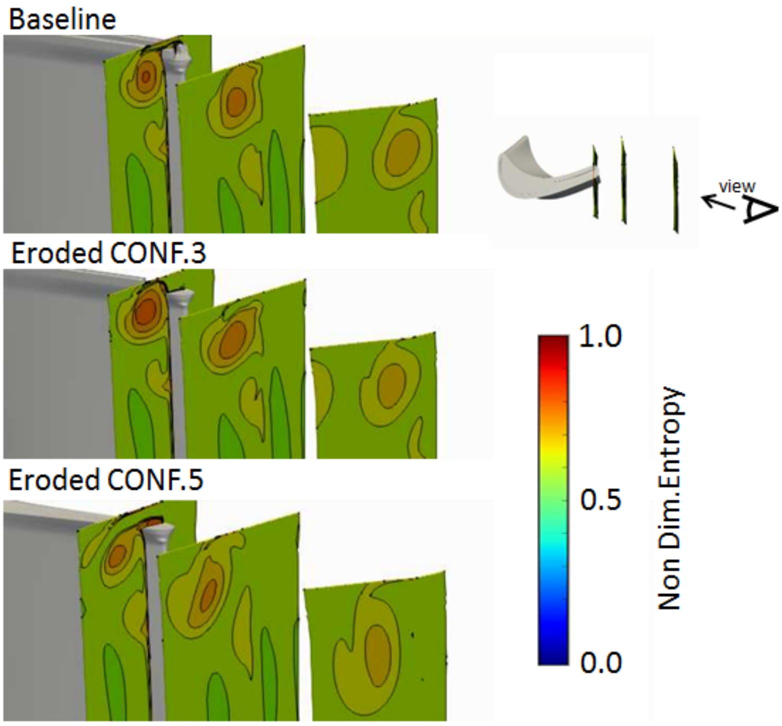

Figure 4.21: Isovalue map of non-dimensional entropy generation

The leading edge horseshoe vortex increases in size in sections closer to the leading edge as soon as the erosion effect becomes more severe. Just after the blade's mid-chord, the leading edge horseshoe vortex mixes with the OTL generating a larger vortex in the worst damaged blade.

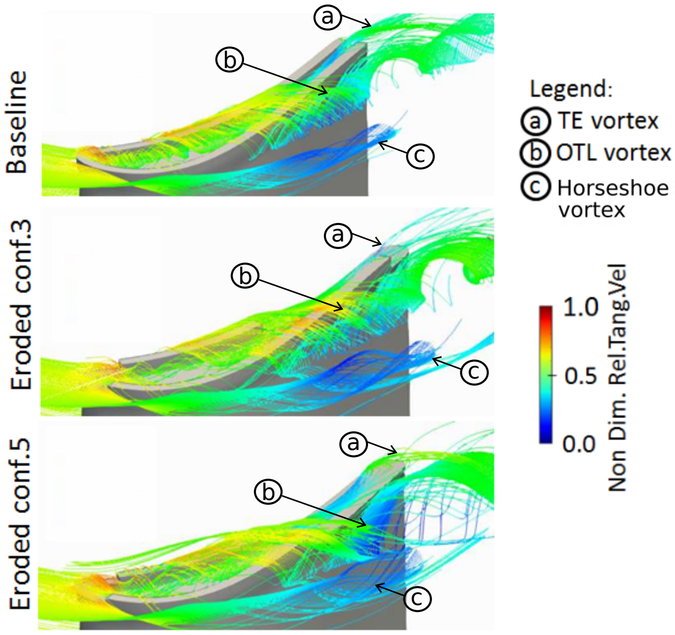

Figure 4.22: Flow visualization in the tip region, colored by non-dimensional relative tangential velocity

Chapter 5

Optimization

The analyses carried out in the previous sections highlighted a small drop in performance due to shape deviations occurring beneath the tip region and a prominent sensitivity of the rotor efficiency concerning the uncertain erosion in the tip region. To improve the figure of merit associated with the nominal blade and desensitize it concerning the typical volume loss as observed in Section 3.3, a series of gradient-based optimizations were run.

The selected optimizer was the version of Sequential Least Squares Quadratic Programming (SLSQP) implemented in the Python library Scipy [4]. The module has been coupled with the suite Effective Quadratures [100, 1] for the PCE construction; an additional class for the calculation of the objective function derivatives was implemented. This class, given the PCE expansion, calculates the derivatives of nominal performance, mean and standard deviation with respect to the design variables, and passes them to SLSQP for the optimization (Section 5.1).

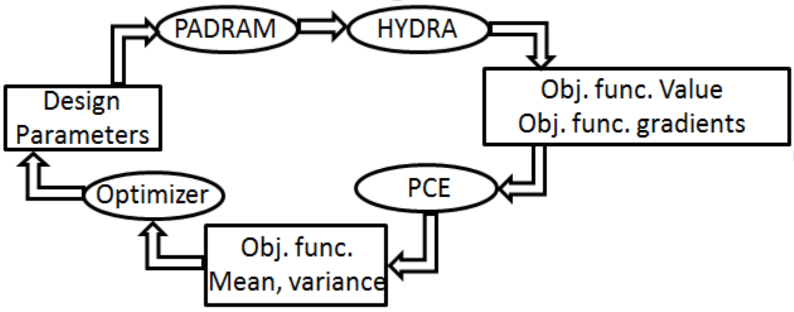

Figure 5.1: Modules involved in the gradient-based optimization process

The small variability of the EPs allows to consider a linear relationship between DELT, LEMO and the objective η_n. The hypothesis of linearity leads to the choice of a first order PCE for the case under study. The number of variables herein considered is the same as described in Section 4.3.2. All the CFD evaluations are carried out by applying the perturbation vectors to the hot, baseline configuration.

More details about the optimization setups and the optimized configurations are reported in the dedicated sections below.

5.1 Adjoint-driven Optimization for the Simplified Geometry

The first optimization aims to improve the nominal performance of a simplified version of the hot configuration. The simplified blade has been obtained by removing both gutter and winglet; the gap between the tip and the upper case is kept the one as for the full-featured, hot geometry.

In each optimization cycle (Figure 5.1):

- PADRAM creates the blade and corresponding domain and mesh by reading the file containing the values of the EPs (DELT and LEMO from 0% to 70% of the blade's span) and applying the required transformations to the baseline geometry.
- HYDRA is run in two separated phases: in the first one the run of the normal CFD (primal) is performed; after convergence is reached, the HYDRA adjoint solver reads the primal flow solution and solves the corresponding equations.
- The gradient of the rotor efficiency is calculated for every design parameter (DELT and LEMO along the aforementioned radial sections) by calling additional HYDRA adjoint tools. The step size of the variables parameters is specified in the input files and is equal to 0.1 for both DELT and LEMO.
- The gradients and the value of the objective function are passed to the PCE. The outcomes of the built surrogate model are the nominal value of the rotor efficiency (objective) and its mean and standard deviation.
- The SLSQP optimization library reads the gradients of the objective function; the optimization aims to minimize the quantity $100 - \eta_n$ by perturbing the geometry thus varying the values of PADRAM EPs, which are passed to PADRAM and a new optimization loop begins.

Given the small sensitivity observed by the baseline configuration concerning the EP variations measured during the inverse mapping procedure, in Section 4.3.2, a larger range is set for the design variables to be optimized: DELT and LEMO, along all the radial sections, can vary ±0.75 (movement towards both the blade's PS and SS). As stated in Section 3.2.3, each design variable has an associated uncertainty and independence is assumed.

In Figure 5.4, the history of the objective function $100 - \eta_n$ is reported: a small performance improvement is achieved during the first step of the optimization cycle;

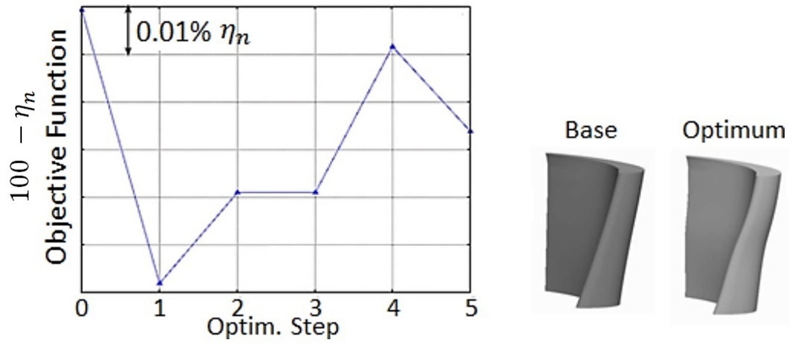

Figure 5.2: First steps and objective function history during the adjoint driven optimization process

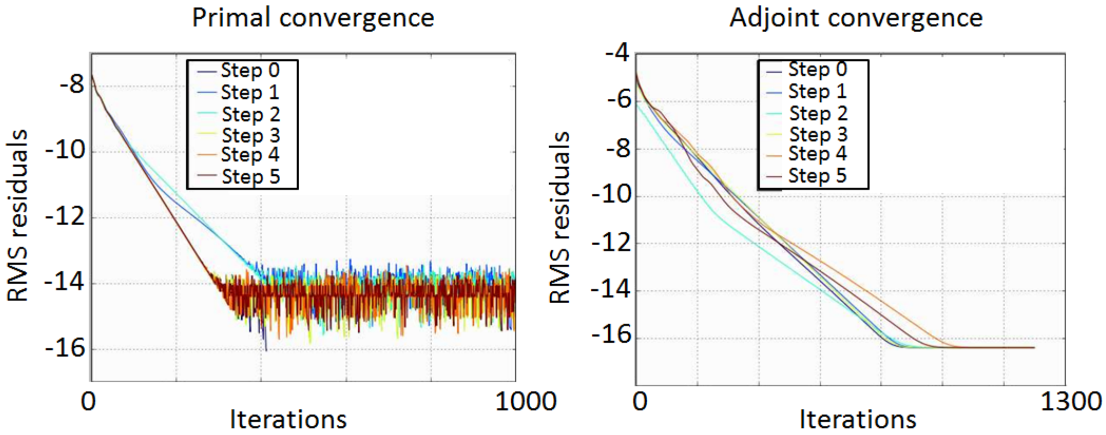

Figure 5.3: Convergence history of primal and adjoint solver during the adjoint driven optimization for the simplified geometry

after that, no further improvements are observed. The values of the perturbation vector are small when compared with the range of variation allowed to the optimizer (Table 5.1). A CFD assessment on the full-featured blade was performed: the full-featured baseline perturbed with the adjoint-driven optimum vector improved the nominal performance by 0.05%. The radial distribution of isentropic efficiency associated with the baseline and this latter perturbed with the adjoint optimum is reported in Figure 5.6; a small difference in the distributions is visible around 70% of the blade's span. The radial distribution of rotor efficiency for the full featured blade perturbed with the adjoint-driven optimum vector is illustrated in Figure 5.6, with a zoom around the zone where a more visible difference between baseline and perturbed geometry is noticeable.

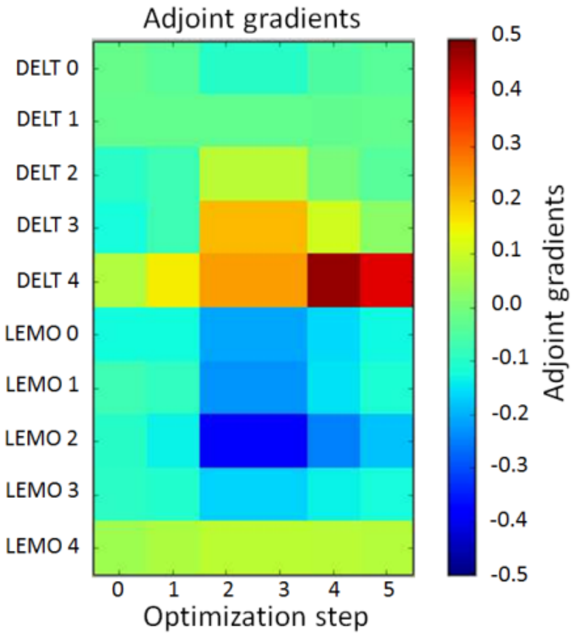

Figure 5.4: Gradients variation during the adjoint driven optimization process

Parameter	**Optimum value**
DELT 0	0.021
DELT 1	0.024
DELT 2	0.095
DELT 3	0.121
DELT 4	-0.070
LEMO 0	0.124
LEMO 1	0.070
LEMO 2	0.099
LEMO 3	0.089
LEMO 4	-0.049

Table 5.1: Perturbation vector for the adjoint-driven optimum

5.1.1 PCE-driven Optimization for the Simplified Geometry

A further optimization was run, calculating the gradients using a first order PCE. The geometry is the same as in the adjoint-driven approach. The PCE receives the PDFs for the design variables, truncated Gaussians, associated with the statistical variation of DELT and LEMO (Section 4.3.2); the PCE basis is a total order, the fitting is performed via least square approximation with oversampling of 1.5. The total number of uncertain variables is equal to 10 (DELT and LEMO along 5 radial sections of the blade) and the number of configurations simulated in each optimiza-

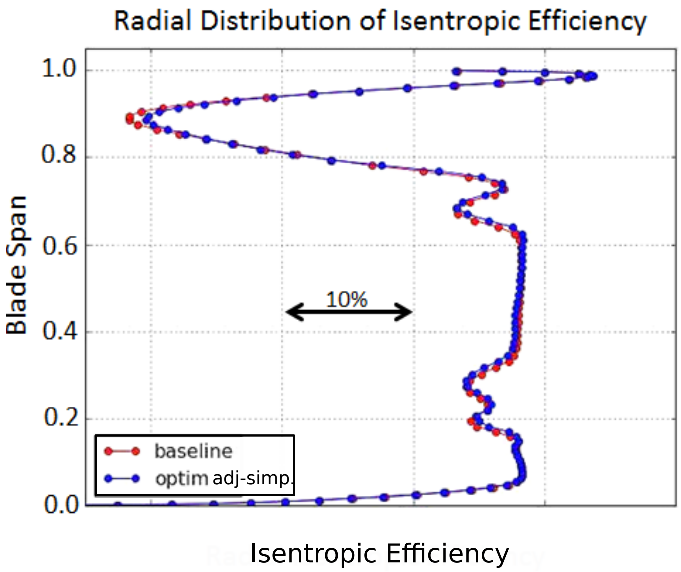

Figure 5.5: Radial distribution of isentropic efficiency, comparison between the simplified baseline and the adjoint optimum

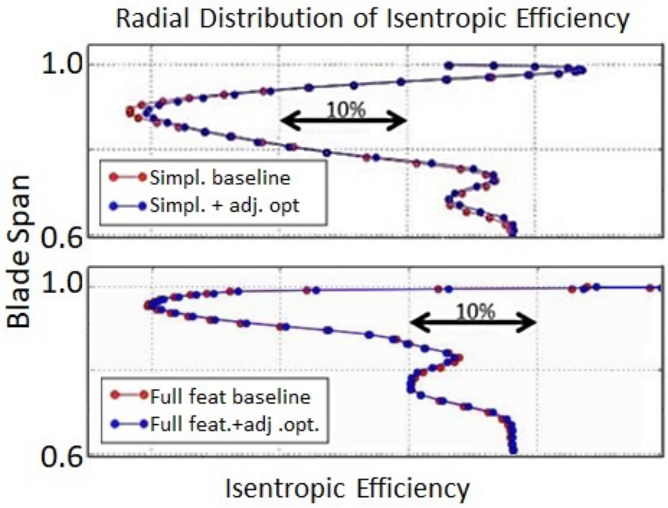

Figure 5.6: Radial distribution of Isentropic Efficiency for the full-featured baseline perturbed with the adjoint-driven optimum vector, full-featured baseline, simplified baseline and the adjoint optimum for simplified geometry

tion step is equal to 17. At each optimization cycle, the PCE calculates the mean value of rotor efficiency η_m representative of the statistical behaviour of the 17 configurations; the standard deviation σ_η of the objective function is also calculated and it is representative of the robustness for the given variability in DELT and LEMO. The history of the minimized objective function $(100 - \eta_n)$ is illustrated in Figure

5.7.

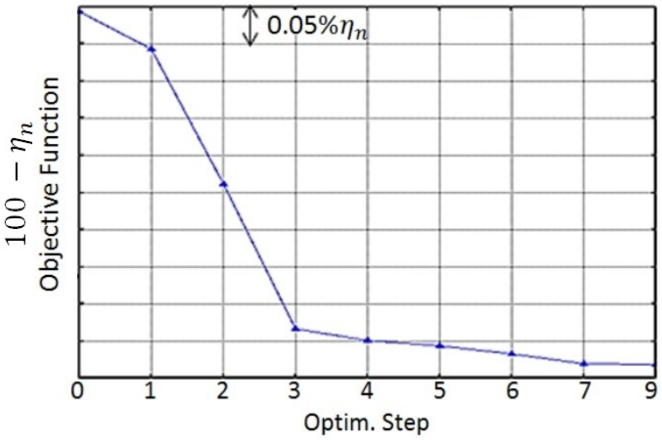

Figure 5.7: Objective function history in the PCE-driven optimization for the simplified geometry

The performance improvement is larger than the one obtained with the adjoint-driven optimization: this time the simplified geometry optimization improved the rotor efficiency by 0.47%.

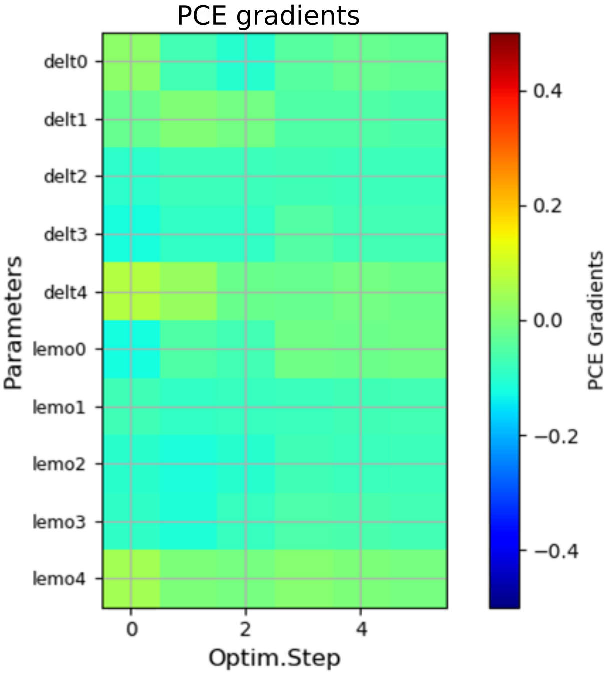

Figure 5.8: PCE derivatives, optimization of the simplified geometry

A comparison in terms of optimal perturbation vectors found for the simplified geometry, with adjoint-driven and PCE-driven approaches, is reported in Figure 5.9: the PCE-driven optimization pushed the values of the optimal configuration towards the edges of the allowed design space. A qualitative comparison of the optimal shapes is illustrated in Figure 5.10.

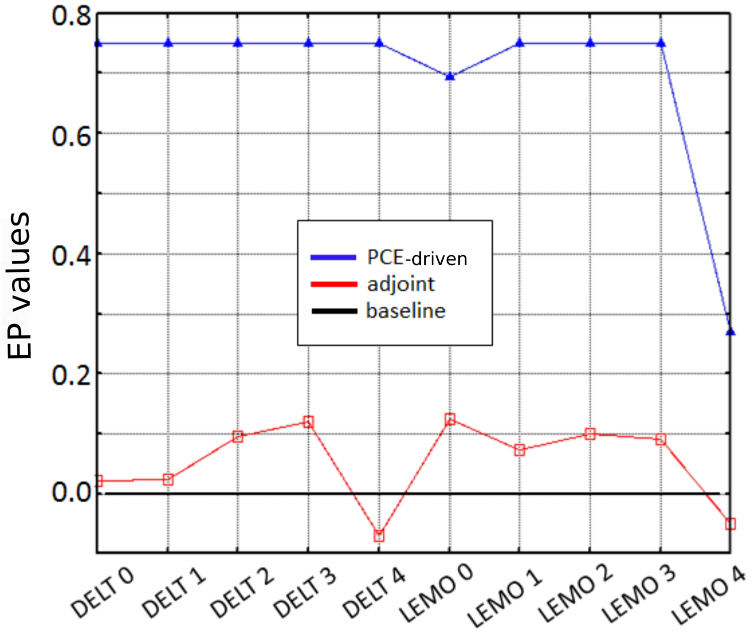

Figure 5.9: Comparison in terms of optimal perturbation vectors found for the simplified geometry: adjoint driven and PCE-driven

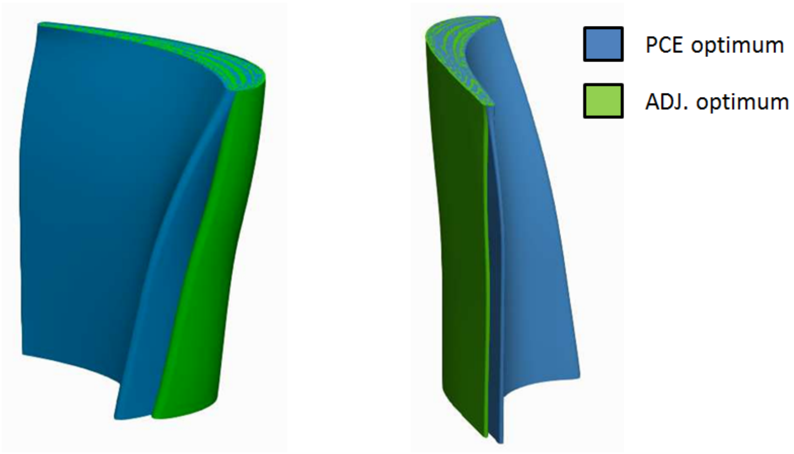

Figure 5.10: Comparison between adjoint-driven optimum, PCE-driven optimum, and the Adjoint-driven simplified geometry

5.2 PCE-driven Optimization for the Full-featured Geometry

The full-featured geometry with nominal rim was optimized via a PCE-driven approach: SLSQP optimizer was provided with the first order derivatives calculated via PCE in each cycle. The setup for the construction of the surrogate model is the same as the one discussed in the previous section, for the simplified geometry. The optimum was reached after three steps, with an improvement of about 0.3% of the nominal rotor efficiency. The magnitude of the PCE derivatives decreased slightly during the optimization. In the rest of the work, this optimum shape will be identified with the name *OPTIMUM A*.

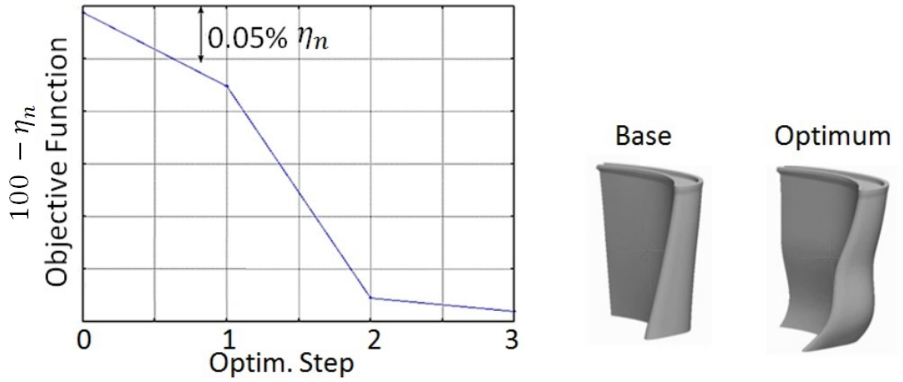

Figure 5.11: Objective function history during the PCE-driven optimization for the full-featured geometry

As already seen for the simplified geometry, the optimizer pushes the values of the optimized variables towards the boundaries of the design space. This time a smaller value of lean is experienced in the sections around 10% and 30% of the blade span (right-hand side of Figure 5.11).

The radial distribution of isentropic efficiency for the full-featured baseline and its PCE-driven optimum is shown in Figure 5.14. The region close to the winglet (around 90% of the blade's span) along with the regions above the hub (between 20% and 30% of the blade's span) have a larger tangentially mass-averaged value of efficiency; smaller differences are noticeable at other radial positions.

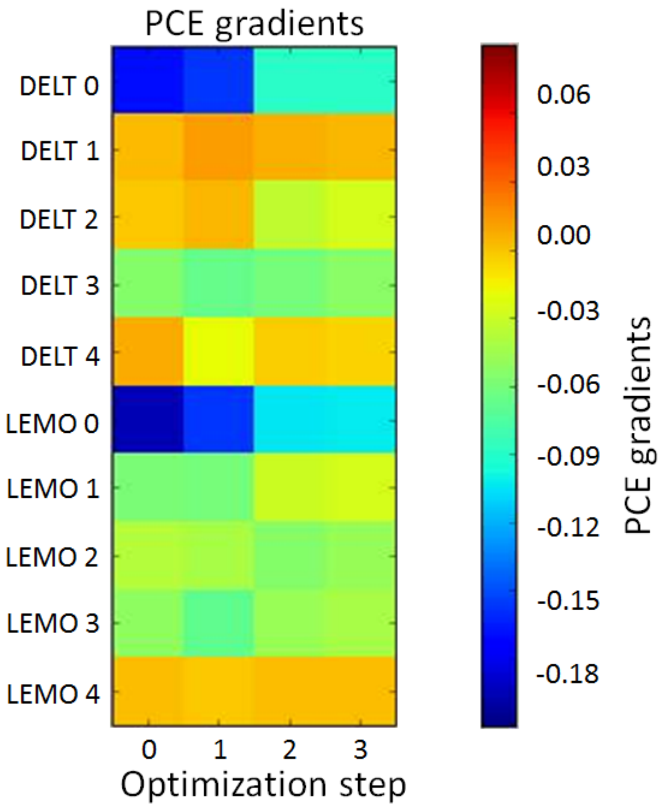

Figure 5.12: PCE derivatives during the PCE-driven for the full-featured geometry

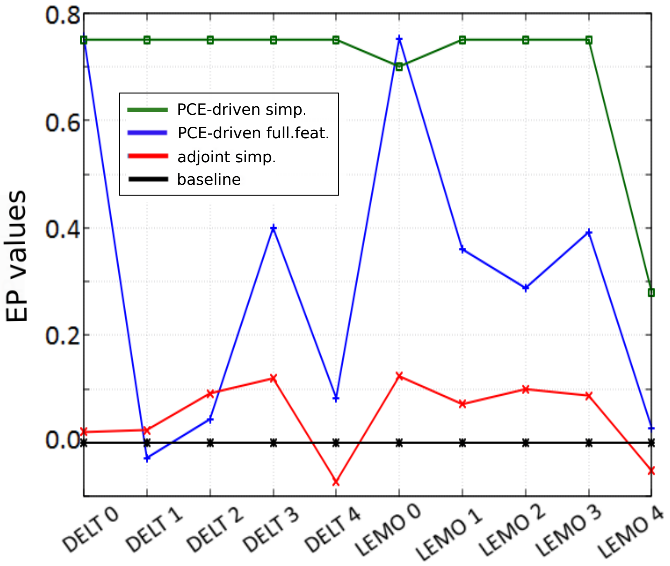

Figure 5.13: Optimum perturbation vectors: comparison between the PCE-driven for full-featured, simplified geometry and adjoint-driven for the simplified geometry

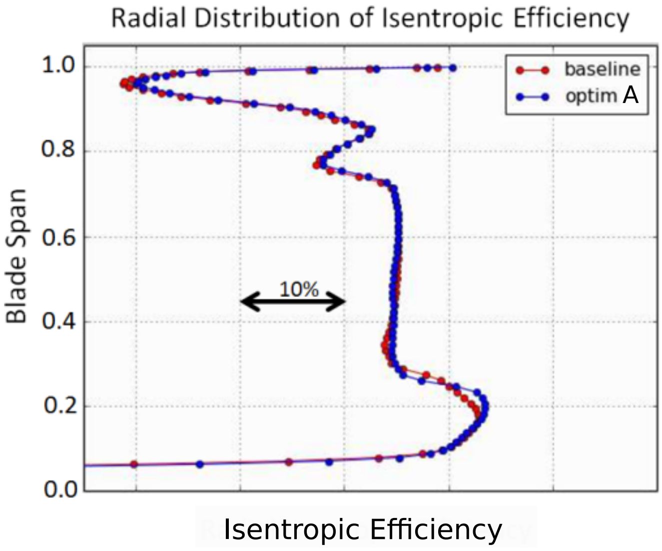

Figure 5.14: Radial distribution of isentropic efficiency for the full-featured baseline and OPTIMUM A

5.3 PCE-driven Optimization for the Worst-case Eroded Geometry

A fifth optimization process was run starting from the perturbation vector of the optimum *A* found in Section 5.2, with the aiming to output a design less sensitive to the typical tip erosion found in the UP analysis in Section 4.4. To limit the computational cost, a worst-case optimization approach is considered: the aim is to maximize the efficiency of the rotor, in the presence of the rim erosion leading to the largest drop in performance (-1.48% for *(CONF5)*, as observed in Section 4.4. The history of the minimized objective function $100 - \eta_e$ is reported in Figure 5.15 and the corresponding standard deviation σ_η, calculated by the PCE surrogate model, in Figure 5.16. The improvement in worst-case performance, associated with the optimum in step 6, is $+0.13\%$ of the nominal value. Incidentally, the optimized geometry is found to be slightly more robust to the imposed variability in the EPs than the configuration in step 0 and a small decrease in standard deviation is experienced, starting from an already low value. The qualitative comparison between the initial configuration (OPTIMUM A with eroded rim) and the optimum (configuration found in step 6) is reported on the right-hand side of Figure 5.15.

The perturbation vector found by optimizing the eroded worst-case scenario was tested by replacing the clean, not eroded rim. In Table 5.2, a comparison in terms of isentropic efficiency is reported for OPTIMUM A and OPTIMUM B, for both nominal geometries and in the presence of the worst-case of rim erosion. The optimum geometry *OPTIMUM B* achieves an improvement in both nominal (η_n) and worst-case rim erosion (η_e) performances, both concerning *OPTIMUM A* and,

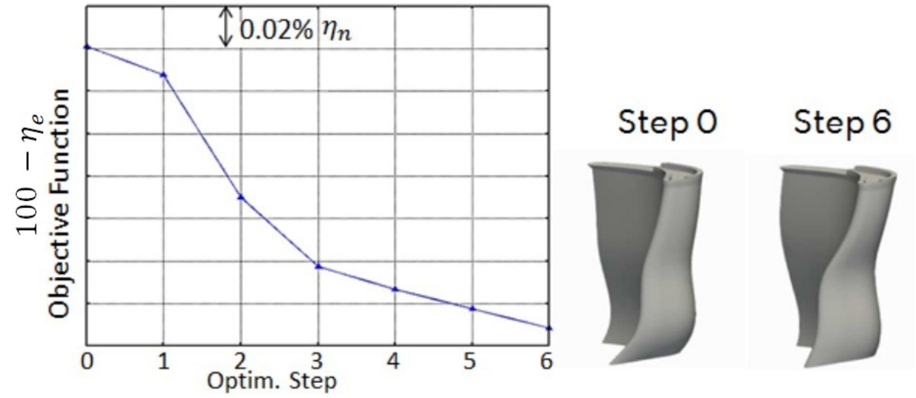

Figure 5.15: Objective function history during the PCE-driven optimization for eroded geometry and comparison of starting and final shapes

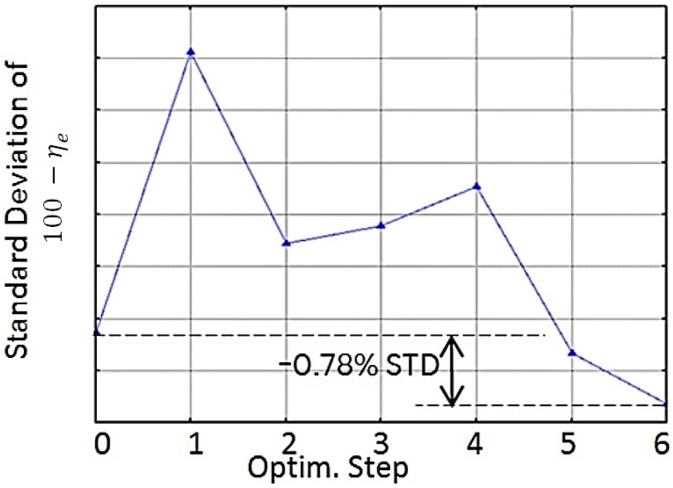

Figure 5.16: Standard deviation of the objective function during the PCE-driven optimization for eroded geometry

even more so, with respect to the baseline geometry.

Geometry	$\eta_n - \eta_{n,d}$	$\eta_e - \eta_{n,d}$
BASELINE	-	-1.48
OPTIMUM A	0.28	-1.06
OPTIMUM B	0.3	-0.92

Table 5.2: Comparison in terms of rotor efficiency for baseline and optimal configurations with eroded and nominal rim

In Table 5.2, $\eta_{n,d}$ represents the nominal performance of the baseline geometry. In the rest of the work, the optimum perturbation vector found in this section is

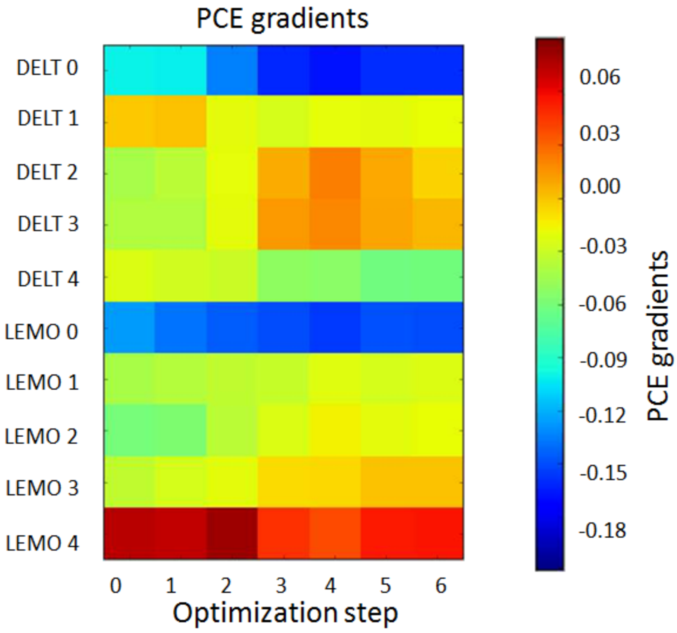

Figure 5.17: PCE derivatives, optimization of eroded geometry

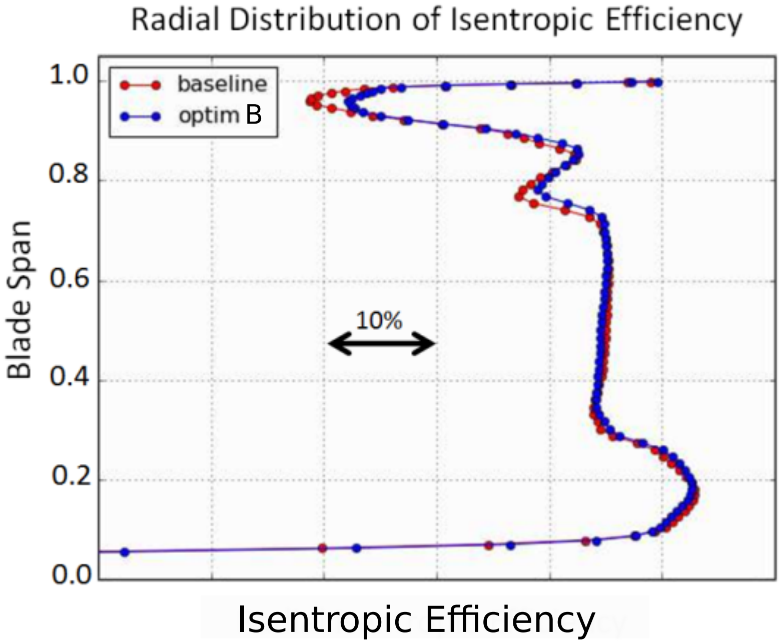

Figure 5.18: Radial distribution of isentropic efficiency for eroded geometries in step 0 and step 6

renamed *OPTIMUM B*.

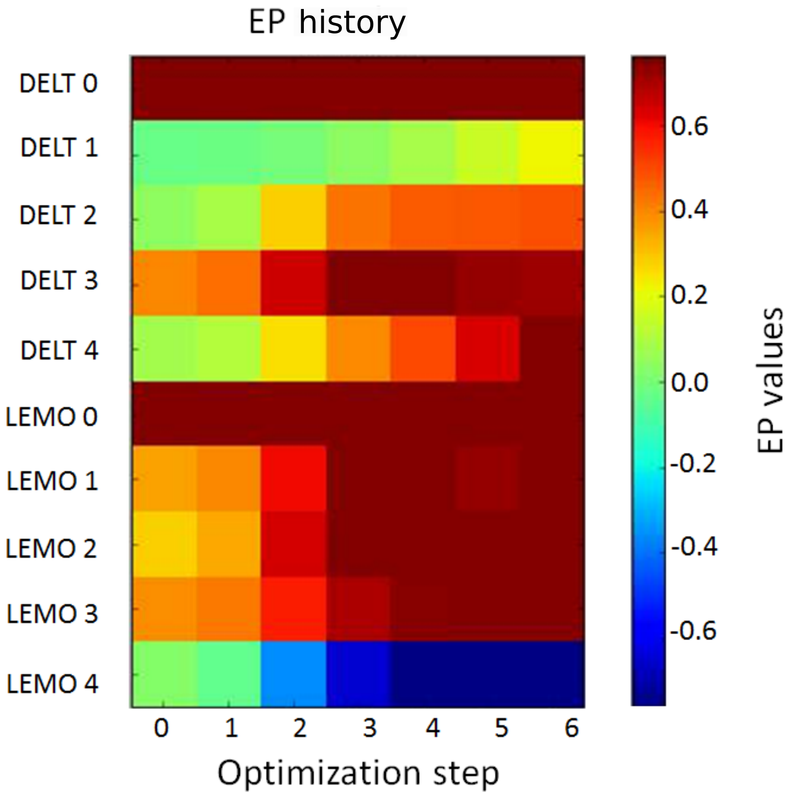

Figure 5.19: DELT and LEMO history during the PCE-driven optimization for the eroded geometry

5.4 Local Optimization (Larger Design Space)

A further gradient-based optimization was carried out starting from the optimum found in Section 5.3 (*OPTIMUM B*); in the presence of a larger design space (more EPs). The EPs herein considered are DELT, LEMO, TEMO, INBA, EXBA, SKEW. The radial positions were set at 0% (hub), 30%, 50%, 70%, and 90% (just below the winglet) of the blade's span. The gradient concerning the design variables was calculated via centered finite differences, using a step size of 0.1 degrees for all EPs and 0.1 mm for SKEW. The values of the derivatives with respect to the 35 design variables are plotted in Figure 5.20

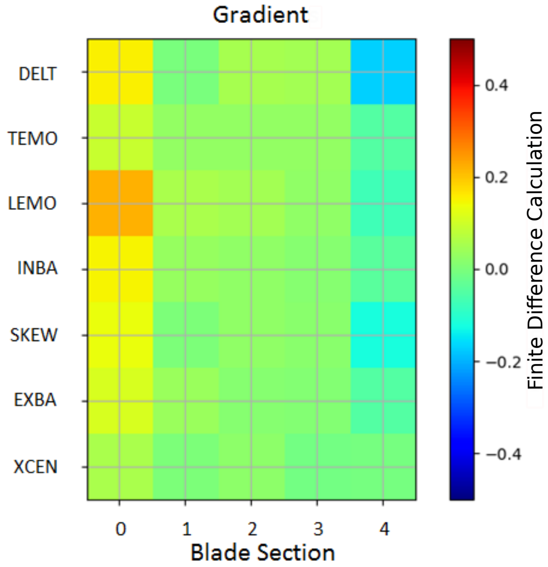

Figure 5.20: Gradient of *OPTIMUM B*'s worst-case efficiency with respect to the design parameters in the larger design space

Given the values of the gradient, 6 new configurations were obtained as follows:

- Perturbing the EPs values along all the directions improved the rotor efficiency, with a perturbation magnitude equal to 0.1, 0.2 and 0.3;
- Perturbing all the EPs values along the gradients directions, with a perturbation magnitude scaled such that the maximum value applied was 0.1, 0.2, and 0.3, respectively.

The new configurations are plotted in Figure 5.21. For each of these, both nominal efficiency (with clean rim) and worst-case efficiency were calculated; by running CFD. The values of nominal and worst-case efficiency are reported in Table 5.3 relative to the nominal efficiency of the baseline rotor geometry.

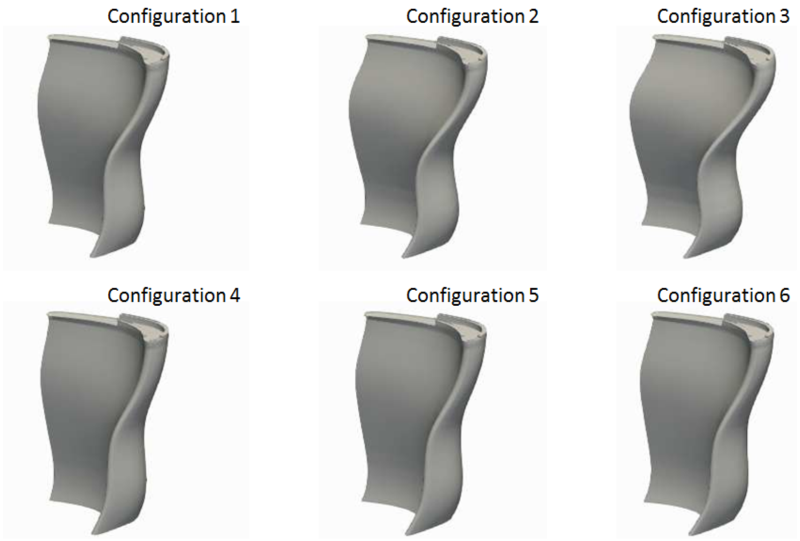

Figure 5.21: Six configurations tested in the local optimization with larged design space

Configuration	$\eta_n - \eta_{n,b}$	$\eta_e - \eta_{n,b}$
1	0.44%	−0.71%
2	0.51%	−0.49%
3 (OPTIMUM C)	0.58%	−0.29%
4	0.42%	−0.79%
5	0.46%	−0.66%
6	0.47%	−0.55%

Table 5.3: Performance improvements achieved in the local optimization with enlarged design space

A gradual performance improvement is experienced for all the configurations with the entire rim, particularly for Configuration 3; the latter is renamed in the rest of the work as *OPTIMUM C*. Recalling Section 4.4, where the worst drop in efficiency for eroded rim was equal to −1.48%, analyzing the third column in Table 5.3, it is possible to observe a global recovery of efficiency when the volumetric loss along the tip takes place. The best configuration in terms of performance recovery is the *OPTIMUM C*, where only 0.29% of isentropic efficiency is lost, i.e. 1.1% is not lost with the worst-case scenario of the eroded rim.

5.5 Discussion of the Results

In this section, the optimal geometries found in the previous sections are analyzed in detail. The analyzed geometries are:

- Baseline;
- *Optimum ADJ*, found by driving the optimizer with the adjoint gradients;
- *OPTIMUM A*, found by optimizing the baseline, with nominal rim, driving the optimizer with PCE derivatives;
- *OPTIMUM B*, found by optimizing the performance in the presence of the worst-case tip configuration, i.e., the one causing the largest drop in performance to the baseline;
- *OPTIMUM C*, found by optimization in a larger design space, aiming to improve the performance in the presence of the worst-case tip configuration.

The radial distribution of isentropic efficiency for the optimized configurations, calculated including the nominal rim in the geometries, is reported in Figure 5.22. For all the optimal shapes, a performance improvement is experienced close to the tip region. This effect is more evident for the *OPTIMUM C*.

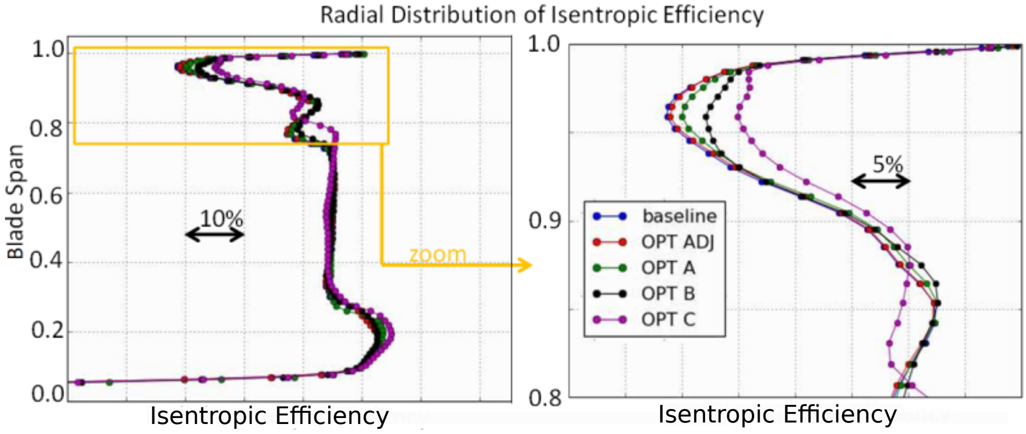

Figure 5.22: Radial distribution of isentropic efficiency for optimized configurations

In Figure 5.23, the distribution of non-dimensionalized relative tangential velocity is illustrated. The planes are located $0.1c$ upstream of the TE and $0.5c$ downstream of the TE. The optimized configuration *OPTIMUM C* shows a reduction in the size of the tip leakage vortex. The 3D visualization of the vortex structures characterizing the flux in the tip region is reported in Figure 5.24. The horseshoe vortex generated by the flow separating at the LE towards the SS of the blade's tip (vortex structure denoted with letter c) experiences a reduction in size as well as

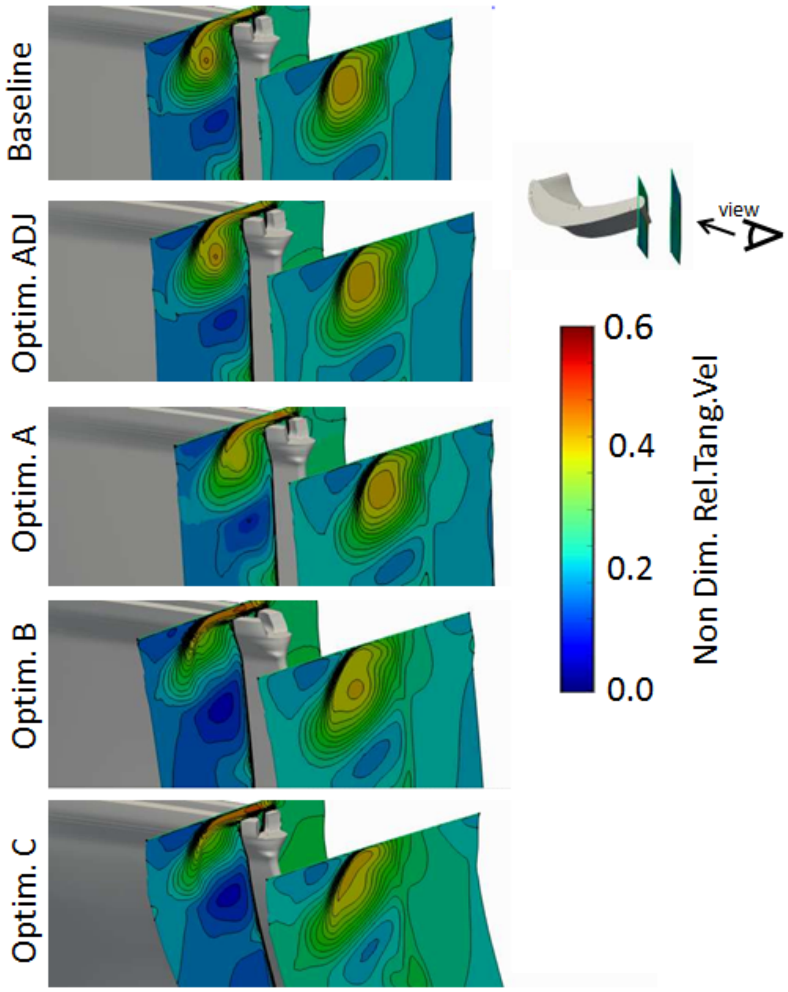

Figure 5.23: Distribution of non-dimensional relative tangential velocity along planes upstream and downstream the trailing edge

the OTL (letter *b*). These two vortex structures are shifted towards radial sections closer to the blade winglet and, for the configuration *OPTIMUM C*, they do not mix by the time they reach the trailing edge sections.

The comparison in terms of entropy generation is reported in Figure 5.25: the latter is plotted along a first plane located $0.1c$ upstream of the TE, a second $0.5c$ downstream of the TE, and a third one $1.5c$ downstream of the TE, near the outlet section of the fluid domain. The reduction in size of the secondary flows is visible, especially for *OPTIMUM C*, along with a general decrease of entropy values in the section close to the exit.

To better understand the load distribution characterizing each optimum configuration, the plot of static pressure is reported in Figure 5.26 along a plane cutting the blades at midspan. A second comparison is reported for a plane cutting the

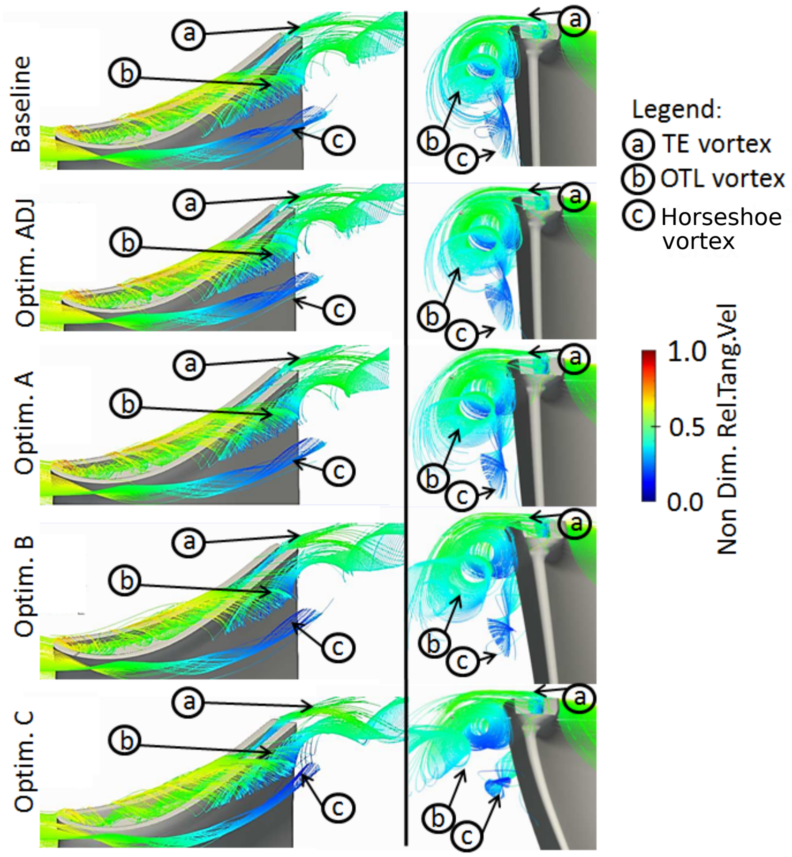

Figure 5.24: OTL colored by non-dimensional relative tangential velocity

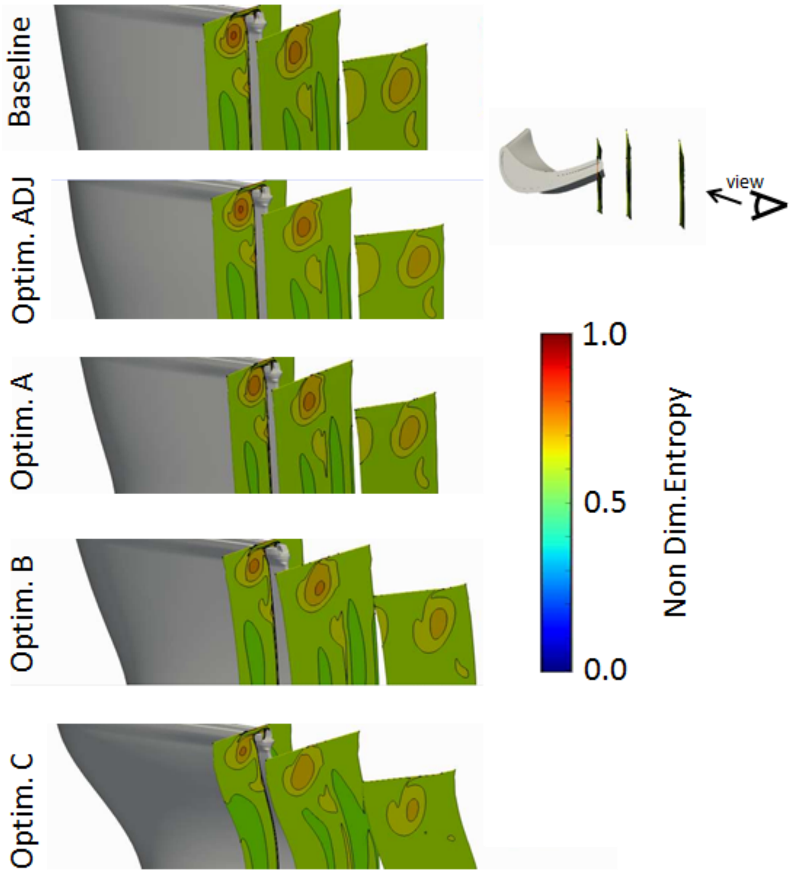

Figure 5.25: Distribution of non-dimensional entropy along planes upstram and downstream the trailing edge

blade along the winglet at 95% of the blade span. The values are reported as a percentage of the reference value of static pressure P_{0-ref} at the outlet of the fluid domain (see boundary conditions setup in Section 4.2.2). The general trend shows a gradual offloading of the tip region, causing a local improvement in performance.

A further assessment was carried out to understand the causes of the performance recovery when the rim erosion occurs: the optimum perturbation vectors, this time, were applied in the presence of the worst eroded rim. The plot with the comparison in terms of non-dimensionalized relative tangential velocity is presented in Figure 5.28, while the non-dimensionalized entropy generation is shown in Figure 5.29. The region associated with higher values of relative velocity decreases in size; lower values of entropy are visible together with a reduction of the vortex's size.

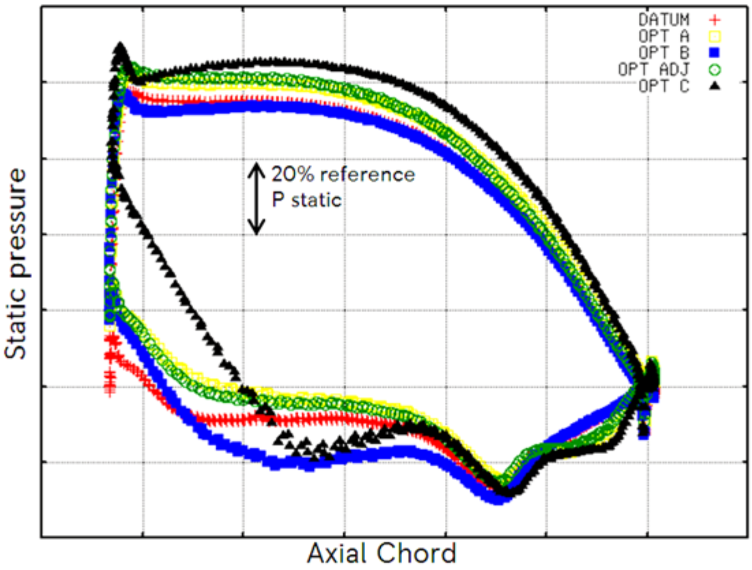

Figure 5.26: Static pressure distribution along the midspan of the optimal configurations compared with the baseline

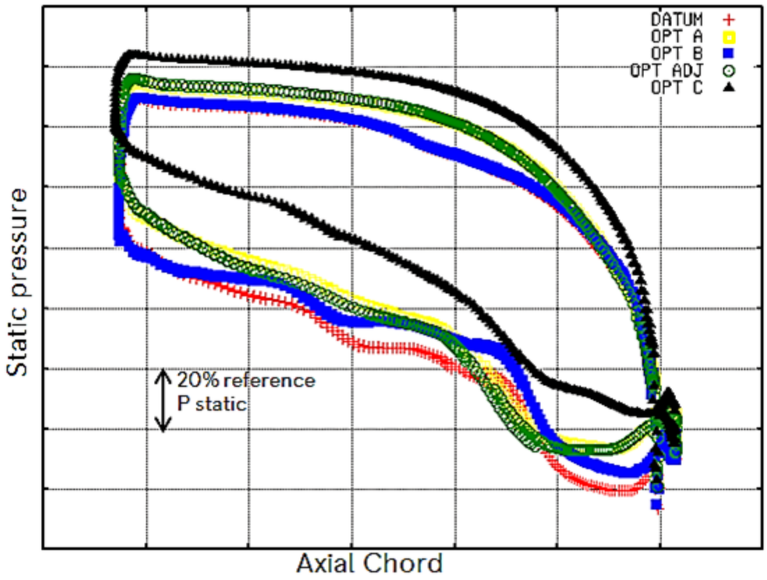

Figure 5.27: Static pressure distribution along a plane passing through 95% of the blade's span, comparison for optimal configurations and baseline

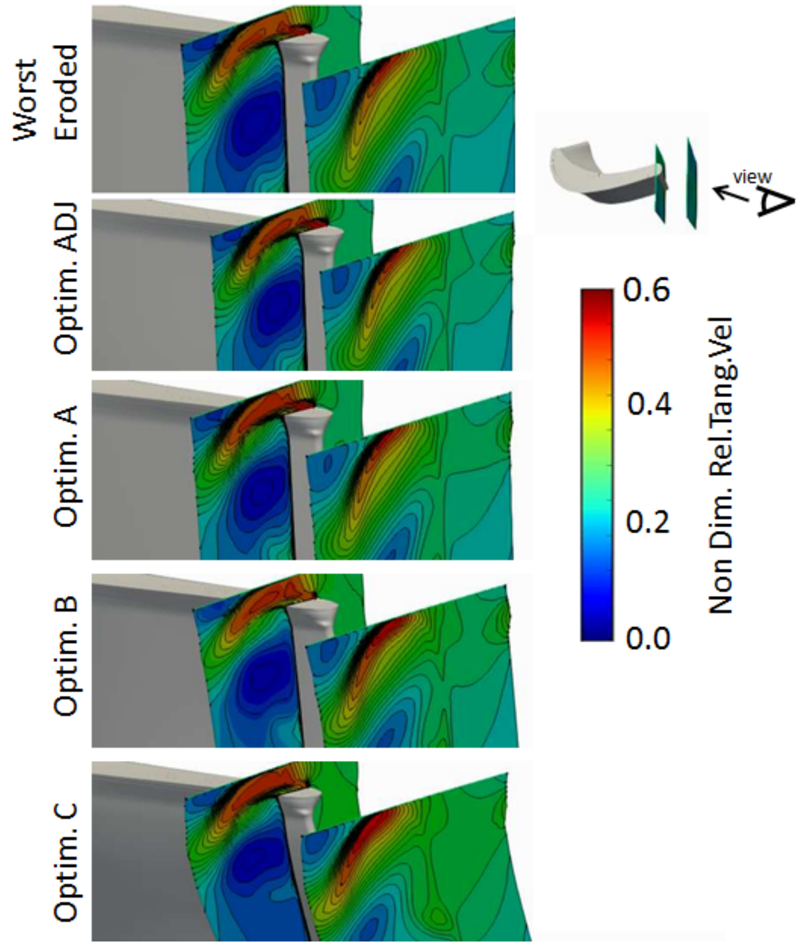

Figure 5.28: Distribution of non-dimensional relative tangential velocity for optimal configurations with eroded rim

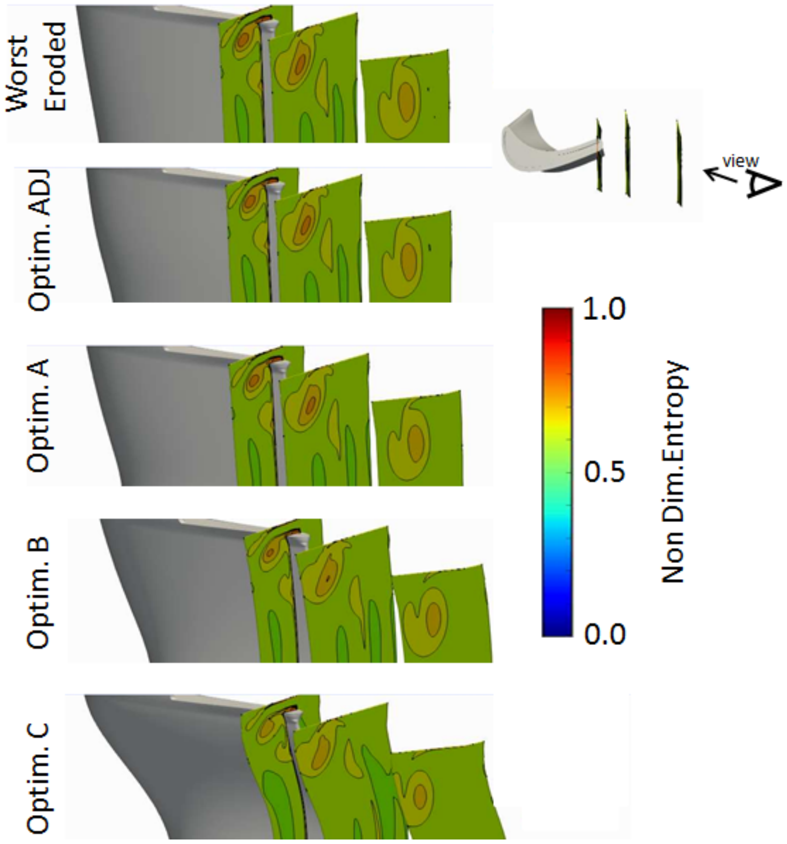

Figure 5.29: Distribution of non-dimensional entropy for optimal configurations with eroded rim

Chapter 6

Conclusions and future work

Conclusions

The design of a modern jet engine for aeronautical propulsion and its components is subject to numerous uncertainties, starting from the manufacturing tolerances which can cause a deviation of the real blades from the expected performance. The working conditions of high-pressure turbine stages are particularly harsh, with maximum values of temperatures close to the melting point of the blade's alloyed metal. In-service deformations and volume loss in the blading system add up to manufacturing uncertainties, causing an even larger deviation from the expected performance.

In addition to all this, operating conditions (velocity, temperature and pressure distribution, but also turbulence levels) are also uncertain, and can vary with time. The present work aims to desensitize a real HPT rotor with respect to the geometrical deviations and the erosion level characterizing the component after several engine flying hours. The numerical strategies adopted to achieve the final goal, a more robust design, use a series of statistical approaches: uncertainty quantification, propagation, and robust optimization.

The test case is represented by a set of 200 real HPT blades; these components were dismounted from four engines, belonging to the same family, and digitized via GOM scan technology. A first classification of the damage enabled to separate two main groups of shape deviations with respect to the expected blade design: the first one is represented by geometry variations occurring from 0% to 70% of the blade span; the second set is constituted by a large volume loss occurring along the tip region of the blade. The rim of the components was systematically eroded in three main zones (trailing edge on both pressure and suction side and the leading edge) thus removing an important aerodynamic feature of the blade, namely the over tip leakage mechanism.

The visual inspection of the digitized blades was followed by identification and parametrization of the uncertain variables leading to the deformed shapes. Geometrical deviations from hub to 70% of the blade span were described by a subset of geometric parameters inside PADRAM design space (EPs). Each GOM scan can be seen as the result of the perturbation of a baseline geometry - the design intent -using all the aforementioned PADRAM variables. The quantification of the EPs deviations from the nominal shape was performed via inverse mapping procedure, for all the 200 blades. The volume loss along the blade tip was parametrized using PADRAM squealer tip option and the quantification of the metal removal rate was carried out by a set of in-house Python scripts.

The uncertainty propagation focused on the aerodynamic performance of the rotor, described by its isentropic efficiency. Two distinct UP campaigns were carried out to identify the most influential parameters causing a drop in performance. The UP was performed using polynomial chaos expansions. The results showed a negligible sensitivity of the efficiency with respect to the EPs variations, and a significant degradation in performance due to the variability of the tip erosion.

For the robust optimization the most influential EPs (DELT and LEMO) were selected as the design variables to improve the nominal rotor efficiency. A series of gradient-based approaches were used: in the first approach a simplified geometry, without winglet and gutter, was optimized driving the optimizer with adjoint gradients. This strategy was followed by a PCE-driven optimization, for both nominal blade and the worst-case scenario of eroded rim: the results showed a small improvement in performance as well as a recovery in efficiency when erosion occurs. The final optimization with a larger design space allowed to achieve a larger improvement in performance and desensitize the rotor with respect to the worst case of eroded rim: the final optimum is, in fact, able to recover a satisfactory percentage of efficiency when the rim is damaged, losing only 0.3% of rotor efficiency.

An offload of the tip region is present in the final, optimized configuration and this causes a local improvement of efficiency; the entropy generation is mitigated along section downstream of the trailing edge of the blade; the overtip leakage and the horseshoe vortex visible in the main flow of the eroded baseline decreased in size and strength in the optimized configuration.

Future works

The present work focused on the aerodynamic performance of the HPT blades. The next step will be a numerical assessment of thermal performance and mechanical stresses. The former is necessary not only to ensure the proper cooling effectiveness but also for the design of the intricate internal film cooling system. The final optimum shape presents a visible curvature; the casting methodology for the production of mono-crystal blades already allows to model complex, external aerodynamic shapes (mould where the wax is poured) but excessive curvatures along the trailing edge might add complexity to the production: the available narrow space inside the trailing edge corner must contain the internal passages for the cooling system and further analysis is needed to determine the best shape of the ceramic core (negative of the film cooling internal passages) to be used in the first stage of the blade production. Conjugate heat transfer and finite element analysis are necessary to assess thermal load distributions and stresses induced by centrifugal forces and vibrations, thus the estimation of the rotor life span. A multi-disciplinary optimization would therefore be necessary to simultaneously consider all these competing objectives.

Authored Conference and Journal Publications

[1] Licheri, F., Ghisu, T., Virdis, I., Puddu, P., Cambuli, F. Evaluation of entropy generation methods in wells turbines (2019) Proceedings of the International Conference on Offshore Mechanics and Arctic Engineering - OMAE, 10, art. no. omae2019-96513

[2] Ghisu, T., Cambuli, F., Puddu, P., Virdis, I., Carta, M., Licheri, F. A critical examination of the hysteresis in wells turbines using computational fluid dynamics and lumped parameter models (2020) Journal of Offshore Mechanics and Arctic Engineering, 142 (5), art. no. 052001, DOI: 10.1115/1.4046379

[3] Ghisu, T., Cambuli, F., Puddu, P., Virdis, I., Carta, M. Discussion: “Unsteady RANS simulations of wells turbine under transient flow conditions” (Hu and Li, ASME J. Offshore Mech. Arct. Eng., 140(1), p. 011901) (2019) Journal of Offshore Mechanics and Arctic Engineering, 141 (4), art. no. 045501, DOI: 10.1115/1.4042875

[4] Cambuli, F., Ghisu, T., Virdis, I., Puddu, P. Dynamic interaction between OWC system and Wells turbine: A comparison between CFD and lumped parameter model approaches (2019) Ocean Engineering, 191, art. no. 106459, DOI: 10.1016/j.oceaneng.2019.106459

[5] Ghisu, T., Cambuli, F., Puddu, P., Virdis, I., Carta, M., Licheri, F. A lumped parameter model to explain the cause of the hysteresis in OWC-Wells turbine systems for wave energy conversion (2020) Applied Ocean Research, 94, art. no. 101994, DOI: 10.1016/j.apor.2019.101994

[6] Scillitoe, A. D., Wong, C. Y., Gross, J. C., Virdis, I., Ubald, B. N., Hill, B., Seshadri, P. Programming with equadratures: an open-source package for uncertainty quantification, dimension reduction, and optimisation, AIAA 2022-2108. AIAA SCITECH 2022 Forum. January 2022., DOI: 10.2514/6.2022-2108

[7] Virdis, I., Ghisu, T., Shahpar, S., de la Puerta, I., Li, H., Digital Shadow and Robust Optimization of In Service Squealer Tip Turbine Blades, (under review) Proceedings of ASME Turbo Expo 2022, Turbomachinery Technical Conference and Exposition GT2022, June 13-17, 2022, Rotterdam, The Netherlands

Bibliography

[1] Effective quadratures. `https://equadratures.org`. Accessed 2021-12-12.

[2] Innovmetric polyworks-modeler, `https://www.innovmetric.com/en/products/polyworks-modeler`. Last accessed 2021-11-30.

[3] Madeleine project eu. `https://www.madeleine-project.eu/knowledge-results/presentations-14`. Accessed 2021-11-30.

[4] SciPy slsqp minimization library. `https://docs.scipy.org/doc/scipy/reference/optimize.minimize-slsqp.html`. Accessed 2021-26-12.

[5] Sir Frank Whittle the first patent. `https://frankwhittle.co.uk/the-first-patent/`. Accessed 2021-12-12.

[6] *Front Matter*. John Wiley e Sons, Ltd, 2017, pp. i–xx.

[7] Abernathy, R., Powell, B. D., Colbert, D. L., Sanders, D. G., and Thompson Jr, J. Handbook, uncertainty in gas turbine measurements. Tech. rep., Arnold Engineering Development Center Arnold AFS TN, 1973.

[8] Agati, G., Borello, D., Di Gruttola, F., Rispoli, F., Venturini, P., Gabriele, S., and Simone, D. Numerical study of droplet erosion in the first-stage rotor of an axial flow compressor. In *Turbo Expo: Power for Land, Sea, and Air* (06 2021), vol. Volume 2B: Turbomachinery — Axial Flow Turbine Aerodynamics; Deposition, Erosion, Fouling, and Icing. V02BT33A003.

[9] Albring, T. A., Sagebaum, M., and Gauger, N. R. Efficient aerodynamic design using the discrete adjoint method in su2. In *17th AIAA/ISSMO Multidisciplinary Analysis and Optimization Conference* (06 2016), vol. AIAA 2016-3518.

[10] Anon. Aeronautics and air transport: Beyond vision 2020 (towards 2050). Tech. rep., Advisory Council for Aeronautical Research in Europe, 2010.

[11] Antinori, G., Arsenyev, I., and Fischersworring-Bunk, A. Robust design optimization of a low pressure turbine rotor discs secondary air system.

In *Turbo Expo: Power for Land, Sea, and Air* (06 2017), vol. Volume 7A: Structures and Dynamics. V07AT32A001.

[12] Avdeev, S., and Tkachenko, A. Approximation Method of the Gas Turbine Engine Compressor Characteristics. In *Turbo Expo: Power for Land, Sea, and Air* (06 2021), vol. Volume 2C: Turbomachinery — Design Methods and CFD Modeling for Turbomachinery; Ducts, Noise, and Component Interactions. V02CT34A038.

[13] Bansal, L., Rathi, V., and Mudafale, K. A review on gas turbine blade failure and preventive techniques. *International Journal Of Engineering Research and General Science 6* (05 2018), 54–62.

[14] Bao, Z., Kou, Z., Han, B., and Li, G. Unsteady Film Cooling Performance on the High Pressure Turbine Shroud Under Rotor-Stator Interaction for an Aero-Engine. In *Turbo Expo: Power for Land, Sea, and Air* (06 2021), vol. Volume 5A: Heat Transfer — Combustors; Film Cooling. V05AT12A003.

[15] Barigozzi, G., Bassi, F., Perdichizzi, A. G., and Savini, M. Experimental investigation of cooling jets mixing in a gas turbine cascade. In *RTO AVT Symposium on Advanced Flow Management: Part B – Heat Transfer and Cooling in Propulsion and Power Systems* (05 2001).

[16] Brezillon, J., and Dwight, R. Discrete adjoint of the navier-stokes equations for aerodynamic shape optimization. In *EUROGEN-Sixth Conference on Evolutionary and Deterministic Methods for Design, Optimization and Control with Applications to Industrial and Societal Problems* (09 2005).

[17] Bunker, R. S. The Effects of Manufacturing Tolerances on Gas Turbine Cooling. *Journal of Turbomachinery 131*, 4 (07 2009). 041018.

[18] Caloni, S. *Multi-disciplinary Multi-objective design optimization of the Shroudless rotor tip for high pressure turbines, PhD Thesis, School of Engineering and Material Science.* Queen Mary University of London, 2018.

[19] Caloni, S., Shahpar, S., and Coull, J. D. Numerical investigations of different tip designs for shroudless turbine blades. In *Proceedings of the Institution of Mechanical Engineers, Part A: Journal of Power and Energy* (2016), vol. 230, pp. 709–720.

[20] Cao, Y., Hussaini, M. Y., and Zang, T. A. Exploitation of sensitivity derivatives for improving sampling methods. *AIAA Journal 42*, 4 (2004), 815–822.

[21] Carter, T. J. Common failures in gas turbine blades. *Engineering Failure Analysis 12*, 2 (2005), 237–247.

[22] Cesari, G., Panella, F., and Pirinu, A. Stress/strain state for critical components of a jet engine aeronautical compressor. *Engineering Failure Analysis 116* (2020), 104745.

[23] Chen, L., and Chen, J. Aerodynamic optimization design for high pressure turbines based on the adjoint approach. *Chinese Journal of Aeronautics 28*, 3 (2015), 757–769.

[24] Crescenti, F., Kipouros, T., Munk, D., and Savill, M. Generating minimal pareto sets in multi-objective topology optimisation: an application to the wing box structural layout. *Structural and Multidisciplinary Optimization 63* (2021), 1119–1134.

[25] Das, I. Robustness optimization for constrained, nonlinear programming problems. *Engineering Optimization 32* (07 2000), 585–618.

[26] Das, I., and Dennis, J. E. Normal-boundary intersection: A new method for generating the pareto surface in nonlinear multicriteria optimization problems. *SIAM J. on Optimization 8*, 3 (03 1998), 631–657.

[27] Dussourd, J. L. A Simple One-Dimensional Model for Primary Turbine Blade Erosion Prediction. In *Turbo Expo: Power for Land, Sea, and Air* (03 1983), vol. Volume 3: Coal, Biomass and Alternative Fuels; Combustion and Fuels; Oil and Gas Applications; Cycle Innovations. V003T05A007.

[28] Duta, M. C., Shahpar, S., and Giles, M. B. Turbomachinery design optimization using automatic differentiated adjoint code. In *Turbo Expo: Power for Land, Sea, and Air* (05 2007), vol. Volume 6: Turbo Expo 2007, Parts A and B, pp. 1435–1444.

[29] Easterby, C. C., Moore, J. D., and Bogard, D. G. Cfd evaluation of internal flow effects on turbine blade leading-edge film cooling with shaped hole geometries. In *Turbo Expo: Power for Land, Sea, and Air* (06 2021), vol. Volume 5A: Heat Transfer — Combustors; Film Cooling. V05AT12A023.

[30] Eliaz, N., Shemesh, G., and Latanision, R. Hot corrosion in gas turbine components. *Engineering Failure Analysis 9*, 1 (2002), 31–43.

[31] Freeman, C. Tip clearance in axial turbomachines. Tech. rep., 1985.

[32] Garner, S., and Ibrahim, Z. Gas Turbine Common Issues, Failure Investigations, Root Cause Analyses, and Preventative Actions. In *ASME Power Conference* (06 2016), vol. ASME 2016 Power Conference. V001T02A007.

[33] Geuens, C., and Verstraete, T. Adjoint-Based Inverse Design of Axial Compressor Airfoils. In *Turbo Expo: Power for Land, Sea, and Air* (06 2021),

vol. Volume 2C: Turbomachinery — Design Methods and CFD Modeling for Turbomachinery; Ducts, Noise, and Component Interactions. V02CT34A002.

[34] Ghisu, T. *Robust Aerodynamic Design of Compression Systems, Ph.D. Thesis.* Univ. of Cambridge, Cambridge, England, U.K., 2009.

[35] Ghisu, T., Lopez, D. I., Seshadri, P., and Shahpar, S. Gradient-enhanced least-square polynomial chaos expansions for uncertainty quantification and robust optimization. In *AIAA AVIATION 2021 FORUM*.

[36] Ghisu, T., Parks, G., Jarrett, J., and Clarkson, P. Adaptive polynomial chaos for gas turbine compression systems performance analysis. *Aiaa Journal - AIAA J 48* (06 2010), 1156–1170.

[37] Ghisu, T., Parks, G. T., Jarrett, J. P., and Clarkson, P. J. Robust design optimization of gas turbine compression systems. *Journal of Propulsion and Power 27*, 2 (2011), 282–295.

[38] Ghisu, T., and Shahpar, S. Toward Affordable Uncertainty Quantification for Industrial Problems: Part I — Theory and Validation. In *Turbo Expo: Power for Land, Sea, and Air* (06 2017), vol. Volume 2C: Turbomachinery. V02CT47A019.

[39] Ghisu, T., and Shahpar, S. Affordable Uncertainty Quantification for Industrial Problems: Application to Aero-Engine Fans. *Journal of Turbomachinery 140*, 6 (04 2018). 061005.

[40] Giles, M. B., Duta, M. C., Muller, J.-D., and Pierce, N. A. Algorithm developments for discrete adjoint methods. *AIAA Journal 41*, 2 (2003), 198–205.

[41] Glezer, B. Turbine blade tip design clearance treatment: Thermal-mechanical design factors affecting turbine blade clearance. Tech. rep., Von Karman Institute for Fluid-Dynamics - Lectures Series 2004-01, 2004, January 19-23.

[42] Haftka, R. T., and Malkus, D. S. Calculation of sensitivity derivatives in thermal problems by finite differences. *International Journal for Numerical Methods in Engineering 17*, 12 (1981), 1811–1821.

[43] Hajiloo, A., Nariman-Zadeh, N., and Moeini, A. *Pareto Optimum Design of Robust Controllers for Systems with Parametric Uncertainties.* 10 2008.

[44] Hatzichronoglou, T. Revision of the high-technology sector and product classification. *OECD Science, Technology and Industry Working Papers* (02 1997).

[45] Hirsch, C., Wunsch, D., Szumbarski, J., Łaniewski-Wołłk, Ł., and Pons-Prats, J. *Uncertainty Management for Robust Industrial Design in Aeronautics: Findings and Best Practice Collected During UMRIDA, a Collaborative Research Project (2013–2016) Funded by the European Union.* Notes on Numerical Fluid Mechanics and Multidisciplinary Design. Springer International Publishing, 2018.

[46] Jakeman, J. D., Franzelin, F., Narayan, A., Eldred, M., and Plfüger, D. Polynomial chaos expansions for dependent random variables. *Computer Methods in Applied Mechanics and Engineering 351* (2019), 643–666.

[47] Jiang, S., Li, Z., and Li, J. Effects of the squealer winglet structures on the heat transfer characteristics and aerodynamic performance of turbine blade tip. *International Journal of Heat and Mass Transfer 139* (2019), 860–872.

[48] John, A., Vivarelli, G., Qin, N., and Shahpar, S. Using feature-based mesh adaptation to improve the adjoint optimization of transonic compressor blades. In *ASME Turbo Expo 2020: Turbomachinery Technical Conference and Exposition* (11 2020).

[49] Kamenik, J., Toal, D. J., Keane, A., Högner, L., Meyer, M., and Shahpar, S. Modeling and impact of high-pressure turbine blade trailing edge film cooling hole variations. In *AIAA Scitech 2020 Forum.*

[50] Kamenik, J., Voutchkov, I., Toal, D., Keane, A., Hogner, L., Meyer, M., and Bates, R. Robust turbine balde optimization in the face of real geometric variations. *Journal of Propulsion and Power 6* (2018), 1479–1493.

[51] Karimi, M. S., Raisee, M., Salehi, S., Hendrick, P., and Nourbakhsh, A. Robust optimization of the nasa c3x gas turbine vane under uncertain operational conditions. *International Journal of Heat and Mass Transfer 164* (2021), 120537.

[52] Kato, H., Mashiko, H., Tokuyama, Y., ichi Funazaki, K., and Takida, J. Robust aerodynamic shape optimization of supersonic turbine using non-intrusive polynomial chaos expansion. In *9th World Congress on Structural and Multidisciplinary Optimization* (2011).

[53] Khajavi, M., and Shariat, M. Failure of first stage gas turbine blades. *Engineering Failure Analysis 11*, 4 (2004), 589–597.

[54] Koekoek, R., and Swarttouw, R. F. The askey-scheme of hypergeometric orthogonal polynomials and its q-analogue.

[55] Kolmakova, D., Baturin, O., and Popov, G. Effect of Manufacturing Tolerances on the Turbine Blades. In *Gas Turbine India Conference* (12 2014), vol. ASME 2014 Gas Turbine India Conference. V001T02A004.

[56] Korolev, Y., Toropov, V., and Shahpar, S. Design optimization under uncertainty using the multipoint approximation method. In *58th AIAA/ASCE/AHS/ASC Structures, Structural Dynamics, and Materials Conference*.

[57] Kulkarni, D. Y., and di Mare, L. Virtual gas turbines part ii: an automated whole-engine secondary air system model generation. In *Turbo Expo: Power for Land, Sea, and Air* (06 2021), vol. Volume 2C: Turbomachinery — Design Methods and CFD Modeling for Turbomachinery; Ducts, Noise, and Component Interactions. V02CT34A034.

[58] Kulkarni, D. Y., Lu, G., Wang, F., and di Mare, L. Virtual Gas Turbines Part I: A Top-Down Geometry Modelling Environment for Turbomachinery Application. In *Turbo Expo: Power for Land, Sea, and Air* (06 2021), vol. Volume 2C: Turbomachinery — Design Methods and CFD Modeling for Turbomachinery; Ducts, Noise, and Component Interactions. V02CT34A033.

[59] Kumar, A., Keane, A., Nair, P., and Shahpar, S. Efficient robust design for manufacturing process capability. In *OSMO UK Conference on Engineering Design Optimization* (01 2006), p. 242.

[60] Kurz, R., Meher-Homji, C., Brun, K., Moore, J. J., and Gonzalez, F. Gas turbine performance and maintenance. In *Asia Turbomachinery & Pump Symposium* (2013).

[61] Lane, R. J., and Behenna, J. EJ200—The Engine for the New European Fighter Aircraft. *Journal of Engineering for Gas Turbines and Power 113*, 1 (01 1991), 25–32.

[62] Langmaak, S., Scanlan, J., and Sóbester, A. Robust gas turbine and airframe system design in light of uncertain fuel and co2 prices. *Journal of Aircraft 53*, 5 (2016), 1372–1390.

[63] Lapworth, L. Hydra-cfd: A framework for collaborative cfd development. In *Conference: International Conference on Scientific and Engineering Computation (IC-SEC)At: Singapor* (07 2004).

[64] Li, F., Liu, Z., and Feng, Z. Film Cooling and Aerodynamic Performance on Multi-Cavity Squealer Tip of a Turbine Blade. In *Turbo Expo: Power for Land, Sea, and Air* (06 2021), vol. Volume 5A: Heat Transfer — Combustors; Film Cooling. V05AT12A025.

[65] Li, Y., Anitescu, M., Roderick, O., and Hickernell, F. Orthogonal bases for polynomial regression with derivative information in uncertainty quantification. *International Journal for Uncertainty Quantification 1*, 4 (2011), 297–320.

[66] Marta, A. C., Shankaran, S., Wang, Q., and Venugopal, P. Interpretation of adjoint solutions for turbomachinery flows. *AIAA Journal 51*, 7 (2013), 1733–1744.

[67] Martin, I., Hartwig, L., and Bestle, D. A multi-objective optimization framework for robust axial compressor airfoil design. *Structural and Multidisciplinary Optimization 59* (06 2019).

[68] Martins, J., and Ning, A. *Engineering Design Optimization.* 10 2021.

[69] Mattioli, E. *Aerodinamica.* Levrotto & Bella, 1992.

[70] Meher-Homji, C. B., and Gabriles, G. Gas turbine blade failure - causes, avoidance, and troubleshooting. *Turbomachinery And Pump Symposia* (1998).

[71] Milli, A., and Shahpar, S. Padram: Parametric design and rapid meshing system for complex turbomachinery configurations. In *Proceedings of the ASME Turbo Expo* (06 2012), vol. 8.

[72] Moore, J. D., Easterby, C. C., and Bogard, D. G. Effects on film cooling performance in the showerhead from geometric parameterization of shaped hole designs. In *Turbo Expo: Power for Land, Sea, and Air* (06 2021), vol. Volume 5A: Heat Transfer — Combustors; Film Cooling. V05AT12A026.

[73] Moore, J. D., Easterby, C. C., and Bogard, D. G. Experimental and Computational Investigation of Film Cooling Performance and External Flowfield Effects due to Impingement Coolant Feed in the Leading Edge of a Turbine Blade. In *Turbo Expo: Power for Land, Sea, and Air* (06 2021), vol. Volume 5A: Heat Transfer — Combustors; Film Cooling. V05AT12A027.

[74] Mukherjee, D. K. Stresses in Turbine Blades due to Temperature and Load Variation. In *Turbo Expo: Power for Land, Sea, and Air* (04 1978), vol. Volume 1B: General. V01BT02A057.

[75] Mura, R., Ghisu, T., and Shahpar, S. Least squares approximation-based polynomial chaos expansion for uncertainty quantification and robust optimization in aeronautics. In *AIAA AVIATION 2020 FORUM.*

[76] Nadarajah, S., and Jameson, A. A comparison of the continuous and discrete adjoint approach to automatic aerodynamic optimization. *Canadian Journal of Earth Sciences.*

[77] Nahum, A. *Frank Whittle (Icon Science): The Invention of the Jet.* Icon Science. Icon Books, 2017.

[78] Nobile, F., Tempone, R., and Webster, C. G. A sparse grid stochastic collocation method for partial differential equations with random input data. *SIAM Journal on Numerical Analysis 46*, 5 (2008), 2309–2345.

[79] Oberkampf, W. L., and Trucano, T. G. Verification and validation in computational fluid dynamics. *Progress in Aerospace Sciences 38*, 3 (2002), 209–272.

[80] Oladyshkin, S., and Nowak, W. Data-driven uncertainty quantification using the arbitrary polynomial chaos expansion. *Reliability Engineering & System Safety 106* (2012), 179–190.

[81] Otero, J. J., sharma, A. S., and Sandberg, R. D. Adjoint-based optimal flow control for compressible dns, 2016.

[82] Padulo, M., Campobasso, M. S., and Guenov, M. D. Novel uncertainty propagation method for robust aerodynamic design. *AIAA Journal 49*, 3 (2011), 530–543.

[83] Pande, P., Neuman, R., and Cavanagh, R. The six sigma way: how ge, motorola, and other top companies are honing their performance. *Das Summa Summarum des Management* (01 2007), 299–308.

[84] Phadke, M., Laboratories, A. . T. B., Telephone, A., and Company, T. *Quality Engineering Using Robust Design.* Prentice-Hall International editions. Prentice Hall, 1989.

[85] Pongetti, J., Kipouros, T., Emmanuelli, M., Ahlfeld, R., and Shahpar, S. Using Autoencoders and Output Consolidation to Improve Machine Learning Models for Turbomachinery Applications. In *Turbo Expo: Power for Land, Sea, and Air* (06 2021), vol. Volume 2D: Turbomachinery — Multidisciplinary Design Approaches, Optimization, and Uncertainty Quantification; Radial Turbomachinery Aerodynamics; Unsteady Flows in Turbomachinery. V02DT36A018.

[86] Poursaeidi, E., Tafrishi, H., and Amani, H. Experimental-numerical investigation for predicting erosion in the first stage of an axial compressor. *Powder Technology 306* (2017), 80–87.

[87] Pérez Arroyo, C., Dombard, J., Duchaine, F., Gicquel, L., and Odier, N. Numerical Investigation of the Interaction Between Gas-Turbine Engine Components With Dynamic Mode Tracking. In *Turbo Expo: Power for Land, Sea, and Air* (06 2021), vol. Volume 2C: Turbomachinery — Design

Methods and CFD Modeling for Turbomachinery; Ducts, Noise, and Component Interactions. V02CT34A041.

[88] Rao, S. S., and Berke, L. Analysis of uncertain structural systems using interval analysis. *AIAA Journal 35*, 4 (1997), 727–735.

[89] Rezazadeh Reyhani, M., Alizadeh, M., Fathi, A., and Khaledi, H. Turbine blade temperature calculation and life estimation - a sensitivity analysis. *Propulsion and Power Research 2*, 2 (2013), 148–161.

[90] Royce, R. *The Jet Engine.* Wiley, 2015.

[91] Rusted, A., and Lynch, S. Determining Total Pressure Fields From Velocimetry Measurements in a Transonic Turbine Flowfield. In *Turbo Expo: Power for Land, Sea, and Air* (06 2021), vol. Volume 2B: Turbomachinery — Axial Flow Turbine Aerodynamics; Deposition, Erosion, Fouling, and Icing. V02BT32A009.

[92] Sabater, C., and Görtz, S. *Gradient-Based Aerodynamic Robust Optimization Using the Adjoint Method and Gaussian Processes.* 11 2020, pp. 211–226.

[93] Saha, A. K., Acharya, S., Prakash, C., and Bunker, R. Blade Tip Leakage Flow and Heat Transfer With Pressure-Side Winglet. In *Turbo Expo: Power for Land, Sea, and Air* (06 2003), vol. Volume 5: Turbo Expo 2003, Parts A and B, pp. 497–507.

[94] Salehnasab, B., Poursaeidi, E., Mortazavi, S., and Farokhian, G. Hot corrosion failure in the first stage nozzle of a gas turbine engine. *Engineering Failure Analysis 60* (2016), 316–325.

[95] Schaefer, J. A., Romero, V. J., Schafer, S. R., Leyde, B., and Denham, C. L. Approaches for quantifying uncertainties in computational modeling for aerospace applications. In *AIAA Scitech 2020 Forum.*

[96] Schmidt, R., Voigt, M., Vogeler, K., and Meyer, M. Comparison of Two Methods for Sensitivity Analysis of Compressor Blades. *Journal of Turbomachinery 139*, 11 (08 2017). 111006.

[97] Scillitoe, A., Ubald, B., Seshadri, P., and Shahpar, S. Design space exploration of stagnation temperature probes via dimension reduction. In *ASME Turbo Expo 2020: Turbomachinery Technical Conference and Exposition* (09 2020).

[98] Scillitoe, A. D., Wong, C. Y., Gross, J. C., Virdis, I., Ubald, B. N., Hill, B., and Seshadri, P. Programming with equadratures: an

open-source package for uncertainty quantification, dimension reduction, and optimisation. In *AIAA SCITECH 2022 Forum.*

[99] Seshadri, P., Duncan, A., Simpson, D., Thorne, G., and Parks, G. Spatial flow-field approximation using few thermodynamic measurements part ii: Uncertainty assessments. *Journal of Turbomachinery 142* (12 2019), 1–18.

[100] Seshadri, P., and Parks, G. Effective-quadratures (eq): Polynomials for computational engineering studies. *The Journal of Open Source Software 2* (03 2017).

[101] Seshadri, P., Shahpar, S., and Parks, G. T. Robust Compressor Blades for Desensitizing Operational Tip Clearance Variations. In *Turbo Expo: Power for Land, Sea, and Air* (06 2014), vol. Volume 2A: Turbomachinery. V02AT37A043.

[102] Seshadri, P., Simpson, D., Thorne, G., Duncan, A., and Parks, G. Spatial Flow-Field Approximation Using Few Thermodynamic Measurements—Part I: Formulation and Area Averaging. *Journal of Turbomachinery 142*, 2 (01 2020). 021006.

[103] Shahpar, S. Towards robust cfd based design optimisation of virtual engine. Tech. rep., NATO, Athens, Greece, Document No. RTO–AVT-147, 2007.

[104] Shahpar, S. Building Digital Twins to Simulate Manufacturing Variation. In *Turbo Expo: Power for Land, Sea, and Air* (09 2020), vol. Volume 2A: Turbomachinery. V02AT32A049.

[105] Shahpar, S., and Caloni, S. Adjoint optimisation of a high pressure turbine stage for a lean-burn combustion system. In *Conference: ETC 10 (Eurpean Turbomachinery Conference)* (04 2013).

[106] Shahpar, S., Kumar, A., and Keane, A. Robust design of compressor blades against manufacturing variations. In *ASME International Design Engineering Technical Conferences; Computers and Information In Engineering Conference. American Society Of Mechanical Engineers (ASME).* (05 2006), vol. 2006.

[107] Sherman, L. L., Taylor III, A. C., Green, L. L., Newman, P. A., Hou, G. W., and Korivi, V. M. First- and second-order aerodynamic sensitivity derivatives via automatic differentiation with incremental iterative methods. *Journal of Computational Physics 129*, 2 (1996), 307–331.

[108] Shi, W., Chen, P., Li, X., Ren, J., and Jiang, H. Effects of squealer tip geometry deviation on flow field and aerodynamic performance using uncertainty quantification method and sensitivity analysis method. In *GPPS Beijing19* (09 2019).

[109] Smolyak, S. A. Quadrature and interpolation formulas for tensor products of certain classes of functions. *Doklady Akademii Nauk SSSR 148* (1963), 1042–1045.

[110] Sobol, I. Global sensitivity indices for nonlinear mathematical models and their monte carlo estimates. *Mathematics and Computers in Simulation 55*, 1 (2001), 271–280. The Second IMACS Seminar on Monte Carlo Methods.

[111] Spalart, P., and Allmaras, S. A one-equation turbulence model for aerodynamic flows. In *30th Aerospace Sciences Meeting and Exhibit*.

[112] Sperling, S., Christensen, L., Celestina, R., Mathison, R., Aksoy, H., Liu, J., and Nickol, J. Coupling of mainstream velocity fluctuations with plenum fed film cooling jets. In *Turbo Expo: Power for Land, Sea, and Air* (06 2021), vol. Volume 5A: Heat Transfer — Combustors; Film Cooling. V05AT12A024.

[113] Tao, Z., Guo, Z., Song, L., and Li, J. Uncertainty Quantification of Aero-Thermal Performance of a Blade Endwall Considering Slot Geometry Deviation and Mainstream Fluctuation. In *Turbo Expo: Power for Land, Sea, and Air* (09 2020), vol. Volume 2D: Turbomachinery. V02DT38A029.

[114] Thompson, D. W., King, P. I., and Rabe, D. C. Experimental Investigation of Stepped Tip Gap Effects on the Performance of a Transonic Axial-Flow Compressor Rotor. *Journal of Turbomachinery 120*, 3 (07 1998), 477–486.

[115] Ullah, I., Alsaleem, S. M., Wright, L. M., Shiau, C.-C., and Han, J.-C. Influence of Coolant Density on Turbine Blade Film Cooling at Transonic Cascade Flow Conditions Using the Pressure Sensitive Paint Technique. In *Turbo Expo: Power for Land, Sea, and Air* (06 2021), vol. Volume 5A: Heat Transfer — Combustors; Film Cooling. V05AT12A015.

[116] Vazquez, R., and Sanchez, J. M. Temperature Measurement System for Low Pressure Ratio Turbine Testing. In *Turbo Expo: Power for Land, Sea, and Air* (06 2003), vol. Volume 1: Turbo Expo 2003, pp. 527–539.

[117] Vishwanathan, A., Vio, G. A., Kipouros, T., and Parks, G. T. On the effect of boundary condition uncertainty on robust topology optimization of aerospace structures. *Finite Elements in Analysis and Design 193* (2021), 103533.

[118] Vivarelli, G., Qin, N., Shahpar, S., and Radford, D. Anisotropic adjoint sensitivity-based mesh movement for industrial applications. *Computers & Fluids 221* (03 2021), 104929.

[119] Wang, H., Wang, C.-h., Zhu, X.-d., Pu, J., Lu, H.-y., Liu, M.-h., and Wang, J.-h. Uncertainty analysis of film cooling of fan-shaped holes on a stator vane under realistic inlet conditions. In *Turbo Expo: Power for Land, Sea, and Air* (06 2021), vol. Volume 5A: Heat Transfer — Combustors; Film Cooling. V05AT12A012.

[120] Wang, K., Shao, H., Zhang, X., Peng, D., Liu, Y., and Zhou, W. An experimental study of turbine vane film cooling using endoscope-based psp technique in a single-passage wind tunnel. In *Turbo Expo: Power for Land, Sea, and Air* (06 2021), vol. Volume 5A: Heat Transfer — Combustors; Film Cooling. V05AT12A028.

[121] White, A., Mahadevan, S., Grey, Z., Schmucker, J., and Karl, A. Efficient calibration of a turbine disc heat transfer model under uncertainty. *Journal of Thermophysics and Heat Transfer 35*, 2 (2021), 234–244.

[122] Wiener, N. The homogeneous chaos. *American Journal of Mathematics 60*, 4 (1938), 897–936.

[123] Wong, C. Y., Seshadri, P., and Parks, G. T. Automatic borescope damage assessments for gas turbine blades via deep learning. In *AIAA Scitech 2021 Forum*.

[124] Wu, H., Xu, S., Huang, X., and Wang, D. The Development and Verification of a Fully Turbulent Discrete Adjoint Solver Using Algorithmic Differentiation. In *Turbo Expo: Power for Land, Sea, and Air* (06 2021), vol. Volume 2C: Turbomachinery — Design Methods and CFD Modeling for Turbomachinery; Ducts, Noise, and Component Interactions. V02CT34A031.

[125] WU, X., ZHANG, W., SONG, S., and YE, Z. Sparse grid-based polynomial chaos expansion for aerodynamics of an airfoil with uncertainties. *Chinese Journal of Aeronautics 31*, 5 (2018), 997–1011.

[126] Xu, L., Bo, S., Hongde, Y., and Lei, W. Evolution of rolls-royce air-cooled turbine blades and feature analysis. In *Asia-Pacific International Symposium on Aerospace Technology, APISAT2014 September 24-26, 2014 Shanghai, China* (2015), vol. 99, pp. 1482–1491.

[127] Yan, X., Huang, Y., He, K., Li, J., and Feng, Z. Numerical investigations into the effect of squealer–winglet blade tip modifications on aerodynamic and heat transfer performance. *International Journal of Heat and Mass Transfer 103* (12 2016), 242–253.

[128] Yan, X., Ye, M., and He, K. Investigations Into Heat Transfer and Aerodynamic Performance of a Worn Squealer Tipped Turbine Stage. *Journal of Turbomachinery 142*, 9 (08 2020). 091012.

[129] Yonezawa, K., Takayasu, M., Nakai, G., Sugiyama, K., Sugita, K., Umezawa, S., and Ohmori, S. An Impact Assessment of Erosion of Nozzle Guide Vanes and Rotor Blades on Aerodynamic Performance of a Gas Turbine by CFD. In *Turbo Expo: Power for Land, Sea, and Air* (06 2019), vol. Volume 2B: Turbomachinery. V02BT40A013.

[130] Zhiying, C., and Ping, Z. Robust optimization design for turbine blade-tip radial running clearance using hierarchically response surface method. In *IOP Conference Series: Materials Science and Engineering* (11 2017), vol. 269, p. 012066.

[131] Zhou, C., and Zhong, F. A Novel Suction-Side Winglet Design Philosophy for High-Pressure Turbine Rotor Tips. *Journal of Turbomachinery 139*, 11 (07 2017). 111002.

[132] Zou, Z., Shao, F., Li, Y., Zhang, W., and Berglund, A. Dominant flow structure in the squealer tip gap and its impact on turbine aerodynamic performance. *Energy 138* (2017), 167–184.